Multimodal imaging of the tumour microenvironment in head and neck cancer

Clinical graduation internship Technical Medicine

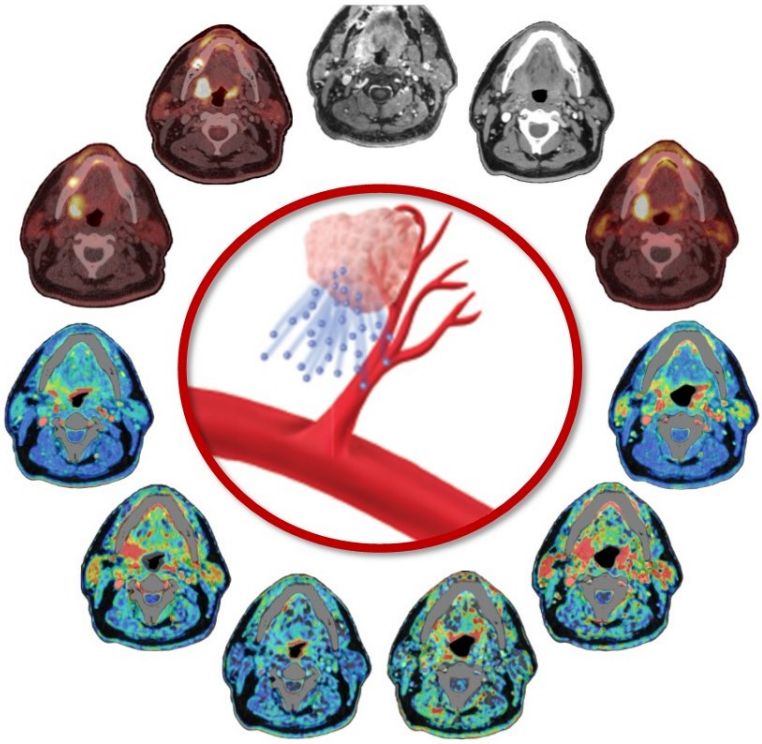

E.A.J. van Genugten

Supervisors from the University of Twente:

Technical supervisor & Chair of graduation committee: Prof. Dr. Ir. C.H. Slump
Process supervisor: Drs. R.J. Haarman
Extern member: Dr. Ir. F.F.J. Simonis

Supervisors from the Radboud UMC, Department of Nuclear Medicine, Radiology & Anatomy:

Medical supervisor: Dr. E.H.J.G. Aarntzen
Technical supervisor: Dr. M. Rijpkema
Daily supervisor: D. Lobeek, MSc

Radboudumc

UNIVERSITY OF TWENTE.

Preface

De afgelopen 13 maanden heb ik met veel plezier stage gelopen op de afdeling nucleaire geneeskunde in het Radboudumc. In dit laatste jaar heb ik geprobeerd om alles wat ik heb geleerd tot nu toe en overal waar ik nog over wil leren en geïnteresseerd in ben samen te brengen. Dit afstuderen bestond uit het opzetten en uitvoeren van een klinische studie, met alle logistieke en theoretische uitdagingen die hierbij horen. De PIVOT studie, een naam beïnvloed door mijn kunstschaats verleden. Vertaald vanuit het engels ook wel 'spil', maar in mijn hoofd meer gerelateerd aan een dansbeweging (tevens ook basketbal en dus ook kunstschaatsen) waarbij één been als middelpunt wordt gebruikt (pivot-punt) waardoor de andere hier in een circulaire beweging omheen kan draaien. Buiten dat het een handig acroniem is kan ik filosoferen over de betekenis; de HPV positieve tumoren zouden het pivot-punt zijn, deze kunnen hopelijk in de toekomst worden voorkomen (stop gezet worden, stilstaan) door het HPV-vaccin. Echter, HPV negatieve tumoren hebben een veel slechtere overleving die wellicht verbeterd kan worden door te kijken naar waardoor het komt dat de HPV^+ tumoren beter reageren. Zo kan het pivot-punt been het andere been helpen om een circulaire beweging te maken, of eigenlijk vooruit te komen.

Dit had ik echt niet gekund zonder alle hulp vanuit het Radboudumc en vanuit de Universiteit Twente. Ten eerste **Daphne**, zonder wie dit onderzoek niet had kunnen starten. Je bent ontzettend gestructureerd, waardoor het altijd een uitdaging bleef om jou een stap voor te zijn i.p.v. andersom. Iedere week, twee keer per week, een keer per twee weken overleg; zolang ik maar dacht dat het me hielp liet je tijd voor me vrij. Met een bemoedigende 'goed gedaan' de meeting afsluiten als je al mijn vragen terug had geketst. Altijd ideeën om ook mijzelf te verbeteren in aspecten niet per se gerelateerd aan alleen die klinische studie. Op een gegeven moment had je zelfs door dat je mij even een half uurtje moest laten ademen nadat ik bijna springend je kantoor binnenkwam met een doorbraak of geschikte patiënt. Wat me vooral van jou bij blijft **Erik**, is dat je altijd weer nieuwe ideeën hebt, door het inzicht in alle verschillende mechanismen en aspecten waar ik mee te maken had. Donderdag was een feest met goede koffie en jouw slechte muziek aan het eind van de dag. En af een toe een uur lang over een PET scan, of mijn onderzoek, kunnen praten omdat je me er zo veel over uit kunt leggen. Maar het aller hardste heb ik gelachen toen je op Austin Powers achtige wijze voorbij mijn kantoor kwam 'lopen' (lees: roltrap). Om het rijtje Radboud compleet te maken, **Mark**, je liet het klinische inzicht over voor anderen maar bleef altijd tussendoor op de gang of tijdens de koffie een oogje in het zeil houden. Vooral met de moeilijke persoonlijke start van mijn stage of als hieromheen wat spannends aan het gebeuren was, had ik het idee dat ik bij je terecht kon en was je altijd een van de eersten die vroeg hoe het was gegaan. Of als je me achter de kont aan zat of ik wel genoeg vrije dagen nam en ging feesten met de vierdaagse.

Zo af en toe mocht ik naar het verre Enschede reizen, maar meestal vond je het het leukst om je studenten in het ziekenhuis op te zoeken. **Professor Slump, Kees,** altijd klaar om nieuwe inzichten te geven en het onderzoek van een andere kant te bekijken wat voor mij erg nuttig was om me uit de tunnelvisie te halen. De hele stage periode van twee jaar met ups en downs heb jij meegemaakt, **Rian**. Tot jouw komst zat ik altijd met een berg op te kijken tegen een reflectie. Door de manier waarop jij ons als groepje vrij hebt gelaten in wat wij nodig hadden heb ik hier erg veel uit kunnen halen. Samen met het groepje van vooral het laatste jaar zagen jullie dingen die ik als vanzelfsprekend beschouwde als waardevolle aanvullingen op de groep. Ik kon altijd kwijt wat me dwars zat en door jullie/jou kwam ik tot de achterliggende oorzaken waar ik zelf nog niet over na heb gedacht. **Frank**, heel fijn en bedankt dat je als zesde lid van deze grote commissie deel uit wil maken, dankjewel voor de snelle feedback en leerzame momenten tijdens mijn bacheloropdracht en MRI-colleges in de master.

Anne, James, Maartje, Marcel, Martin, Willemijn, alle laboranten en andere medewerkers van de nucleaire geneeskunde bij wie ik met al mijn klinische vragen en leerdoelen terecht kon en mij uitleg bleven geven als ik weer iets nieuws in het Nucleaire vakgebied had ontdekt waar ik tijdens de koffie meer

over wilde weten. Maar ook die met mij mee hebben staan juichen toen de RGD synthese voor de eerste patiënt was gelukt na een veel te spannende 20 minuten. En natuurlijk **Willem Jan, Bianca en Hans** die mij hebben geholpen wegwijs te worden op andere afdelingen en mij nieuwe inzichten konden geven.

De interactie en openheid van de **NucMed** research groep vind ik erg bijzonder en buiten dat dit heeft bijgedragen aan de kwaliteit van mijn onderzoek, heeft dit geleid tot een erg hoog werkplezier. Een semi-vaste werkplek waar ik al mijn vragen kon stellen vanachter de computer, of wedstrijdje met Marti of de bus of fiets sneller was vanaf het station. Samen klagen met René en luisteren naar onhandige verhalen van Sanne. Verder alle andere hulp vanuit de andere afdelingen in het ziekenhuis die deze thesis toch niet zullen lezen; de andere co-researchers die mee hebben geholpen aan de onderzoeksaanvraag, maar ook de rest van de goed geoliede hoofd-hals oncologie groep met specifiek all medewerkers van de radiotherapie die mij alweer zagen aankomen met de volgende logistieke vraag.

Als allerlaatste de mensen die verder weinig van dit verslag zullen snappen, **Jasper**; na al die jaren kan ik eindelijk thuis komen en je misschien 1 minuutje spreken per dag ook al is één van ons half aan het slapen in ons prachtige huisje. Mijn ouders, broers en zus die het nooit raar vonden als ik weer wat nieuws had bedacht om te doen tijdens mijn studententijd. Verder alle fijne vriendschappen die ik heb overgehouden uit Enschede die mijn studententijd eentje hebben gemaakt om nooit te vergeten maar die me stiekem ook veel hebben geleerd over mezelf.

Contents

List of Abbreviations and Relevant Definitions

AATH	Adiabatic Approximation to the Tissue Homogeneity model
AATHFT	AATH model with Fixed Transit time
AF	Arterial flow
AIF	Artial Input Function
ALARA	As Low As Reasonably Practicable
Bq	Becquerel
BV	Blood Volume
CD44	A cel surface adhesion receptor, regulates metastasis
CDKN2A	Cyclin Dependant Kinase inhibitor gene, encoding for p16
CKD-EPI	Chronic Kidney Disease Epidemiology Collaboration
cm	centi meter
CMO	Committee on research involving human subjects (Commissie Mensgebonden Onderzoek)
CT	Computed Tomography
DLP	Dosis Length Product
DOTA	1,4,7,10-tetraazadodecane-N,N',N",N"'-tetraacetic acid
E6	HPV viral oncoprotein resulting in p53 degradation
E7	HPV viral oncoprotein binding pRB resulting in loss of function of pRB
EC	Endothelial Cell(s)
ECM	Extracellular Matrix
EGFR	Endothelial Growth Factor Receptor
ENT	Ear-Nose and Throat
ETM	Extended Tofts Model
^{18}F	Fluoride-18
[^{18}F]FDG	2-deoxy-2-(^{18}F)fluoro-D-glucose
FDG PET/CT	[^{18}F]FDG PET/CT
FE	Flow Extraction product
^{68}Ga	Gallium-68
^{68}Ga-RGD$_2$	[^{68}Ga]Ga-DOTA-RGD$_2$
g	grams
Gy	Gray
HNSCC	Head and Neck Squamous Cell Carcinoma
HPV	Human Papillomavirus
HU	Hounsfield units
ICRP	International Commission on Radiological Protection
IRF	Impulse Response Function
kV	kilo Voltage
kVp	peak kilo Voltage

mA	milli Ampere
mAs	milli Ampere second
MBq	Mega Becquerel
METC	Medical research ethics committee (Medische Ethische Toetsings Commissie)
min	minute/minutes
ml	milli liter
MMP	Matrix Metallo Proteases
MRI	Magnetic Resonance Imaging
mSv	milli sievert
MTT	Mean intravascular Transit Time
MTV	Metabolic Tumour Volume
MVD	Microvessel Density
NSAID	Non-Steroidal Anti Inflammatory Drug
OPSCC	Oropharyngeal Squamous Cell Carcinoma
OSCC	Oral Squamous Cell Carcinoma
p16	cyclin dependant kinase inhibitor, tumor suppressor protein
p53	tumor suppressor protein regulating cell division by transducing intracellular signals or activating other genes to fix DNA damage.
pRB	Rentinoblastoma protein, regulator in cell-cycle progression
PCR	Polymerase Chain Reaction
PET	Positron Emmision Tomography
p.i.	post injection
PS	Permeability Surface product
Radboudumc	Radboud University Medical Centre
RGD_2	Dimeric, cyclic Arginine-glycine-aspartic acid peptide, E-$[c(RGDfK)]_2$
RGD PET/CT	^{68}Ga-RGD_2 PET/CT
ROI	Region of Interest (2 dimensional)
s	second/seconds
SUV	Standardized Uptake Value
TLG	Total Lesion Glycolysis
TM	Tofts Model
TNM	Tumour, Node, Metastasis
TP53	Tumor Protein p53, a tumor suppressor gene that provides instructions for making p53
VEGF	Vascular Endothelial Grwoth Factor
VOI	Volume of Interest (3 dimensional)

Abstract

Introduction: The five year survival of patients with head and neck squamous cell carcinomas (HNSCC) has remained unchanged in the last decade even though the morbidity due to treatment remains high. Currently, treatment decisions are based on clinical presentation whereas the increased therapy response in HPV induced oropharyngeal carcinomas (OPSCC) suggests a large influence of biological factors. Genetic mutations do not accurately represent the complexity of individual specialized cell types and extracellular matrix that is known as the tumour microenvironment. In order to become malignant, a tumour has to acquire multiple capabilities, in an early phase of tumourigenesis induction of angiogenesis is upregulated. Multimodal imaging is proposed to characterize angiogenesis using ^{68}Ga-RGD$_2$ PET/CT, designed to target angiogenesis-related integrin $\alpha_v\beta_3$, and perfusion of blood within tumour and possible suspected lymph nodes by CT perfusion. Previous dynamic PET imaging results of HNSCC patients intravenously injected with ^{68}Ga-RGD$_2$ concluded a steady state in tumour uptake and good tumour to background signal after $10-15min$ incubation. A phantom and patient test concluded feasibility of the newly developed oropharyngeal carcinoma CT perfusion protocol.

Method: Ten patients with HPV$^+$ and ten with HPV$^-$ OPSCC scheduled for chemoradiotherapy are expected to be prospectively included in this clinical study. At the time of writing, one patient with a HPV$^+$ T2N1M0 OPSCC was included. The subject underwent CT perfusion imaging and list mode PET/CT imaging from 10 to $20min$ after an intravenous injection of ^{68}Ga-RGD$_2$ ($213.6 \pm 8.1MBq$) before commencement of therapy. During the second week of chemoradiotherapy, ^{68}Ga-RGD$_2$ PET/CT and CT perfusion scans were repeated (follow-up) to. MRI and [^{18}F]FDG PET/CT made per standard of care were correlated to the study results an on basis of the MRI, tissues were characterized as benign or malignant. Quantitative analysis of the tumour, suspected lymph nodes and benign reference tissue was expressed as Standardized Uptake Values (SUV) for the ^{68}Ga-RGD$_2$ PET/CT scans from 15 to $20min$ post injection and for the [^{18}F]FDG PET/CT scan. For these tissues, the arterial flow (AF), blood volume (BV) and flow extraction product (FE) were calculated on basis of the CT perfusion scan.

Results: SUV$_{mean}$ and SUV$_{max}$ of [^{18}F]FDG within the tumour were 8.1 and 28.7, respectively, resulting in a total lesion glycolysis (TLG) of $117.5g$. ^{68}Ga-RGD$_2$ uptake was increased during the follow-up scan (baseline SUV$_{max}$ 8.7 and follow-up 12.1) as well as the FE, BV and AF decreased slightly. CT perfusion parameters, ^{68}Ga-RGD$_2$ and [^{18}F]FDG uptake varied considerably for lymph nodes with and without central necrosis. AF, BV and ^{68}Ga-RGD$_2$ uptake was higher during follow-up in all suspected lymph nodes compared to baseline. A benign tooth abscess had high baseline characteristics comparable to necrotic lymph nodes, during the follow-up scan decrease in BV and ^{68}Ga-RGD$_2$ uptake was seen.

Discussion & Conclusion: Possible positive correlations with response to therapy were found on basis of comparison of TLG, AF and BV to literature. However, the [^{18}F]FDG SUV$_{max}$ and baseline ^{68}Ga-RGD$_2$ SUV$_{mean}$ were comparable to uptake in HPV$^-$ tumours which could indicate a worse prognosis. The difference in quantitative parameters between necrotic and non-necrotic lymph nodes is probably due to an accompanying inflammatory process. This is concluded on basis of pro-inflammatory signals that are shown to be released by necrotic cell death, the comparable values of a benign abscess and high [^{18}F]FDG uptake that can be a hallmark of extracapsular spread of tumour. Increased uptake of ^{68}Ga-RGD$_2$, and therefore increased expression of integrin $\alpha_v\beta_3$, is seen in the tumour and suspected lymph nodes during the follow-up scan. An hypothesis is that this sustained angiogenesis reflects the adaptation of the carcinoma to the treatment resulting in persistence of a non-hypoxic tumour environment and therefore persevering response to chemoradiotherapy. Characterization of the tumour microenvironment with multimodal imaging could possibly help us in the future to identify targets for therapy and monitor response.

1 General introduction

In 2018, head and neck cancer was the seventh most common cancer worldwide with 890.000 new cases and 450.000 deaths[1]. The marginal increase in 5-year survival rate from 60% (1989) to 68% (2011)[2] illustrates the pressing need to a better understanding aiding personalized treatment in this fragile patient population. The majority of tumours of the head and neck area originate from squamous cells. However, the biological behaviour and response to treatment depends not only on the tissue of origin but also on the associated risk factors, growth pattern and anatomical subsite.

Patients diagnosed with head and neck squamous cell carcinoma (HNSCC) are typically of older age and tumourigenesis is associated with heavy use of tobacco, alcohol and poor (oral) hygiene. Additionally, some viruses are linked to be carcinogenic in this area; the Epstein Barr virus is associated with predominantly nasopharynx carcinomas and the human papilloma virus (HPV) related cancers often arise from the tonsil crypts in the oropharynx.

1.1 Treatment modalities

HNSCC can arise from the skin, naso-, hypo- or oropharynx, larynx, lip, mouth cavity and nose. Lymph node metastases mainly occur in the cervical lymph nodes although drainage patterns differ between sites and patients. The gold standard for diagnosing HNSCC is histopathological examination of a biopsy of the primary tumour and cytology on suspicious metastatic lymph nodes. The treatment plan depends on the subsite of the tumour, performance status, the size and metastasis pattern; combined in different TNM classifications per subsite[3]. Treatment modalities are surgery including sentinel node or selective neck dissection. Furthermore, radiotherapy with possible addition of concomitant chemotherapy is the option of choice for oro- hypo- or nasopharyngeal tumours, when no dissection is possible - based on functional outcome - or when a dissection was irradical. In the palliative setting, immunotherapy (in study context) is an important new development. In the Radboudumc there is a strict head and neck oncology intake procedure. This incredibly fast diagnostic process facilitates that in 2018, 373 of 424 of patients began treatment within a month, with a mean start date of 22 days after initial intake in the Radboudumc.

These squamous cell tumours sometimes tend to grow cancerous, extranodal or perineural which makes the treatment area more challenging, especially because surgical resection requires a sufficient marge around the tumour to ensure no single cells are left behind. Radiotherapeutic treatment is planned on basis of anatomical scans of the patient. Even though the high dose on the tumour is delineated very thoroughly, the surrounding regions are still receiving high levels of radiation. For example salivary glands are impossible to avoid when planning accurate treatment and will virtually lose function due to the treatment. Additionally, mucositis, dermatitis, dysphagia, hearing impairment, fatigue and swallowing impediments are not uncommon side effects and are more severe when concurrent chemotherapy is added. Therefore, treatment of these tumours often has a significant effect on the quality of life of the patient.

While treatment plans are adjusted to the subsite and clinical presentation of the patient, instead of biological aspects of a tumour which might provide an opportunity to decrease the high morbidity caused by ineffective treatments.

1.2 Human papilloma virus

The incidence of HPV$^+$ oropharyngeal squamous cell carcinomas (OPSCC), arising from tonsil crypts, has increased over the years due to more (oral) sexual contacts and is also associated with cervical, vaginal, penile and anal cancer[4]. Patients with HPV related OPSCC typically present with smaller primary tumours and even though prominent lymph node metastases are not uncommon, these patients have a much higher 8-year overall survival of 70.9% compared to 30.2% when presenting at an advanced stage[5]. HPV can be divided into low and high-risk types; of these high risk types, HPV-16 is predominantly responsible for cervical, anogenital and HNSCCs. Most HPV infections are eliminated naturally by the immune system within weeks to months[6]. A major risk factor for development of high-grade lesions and cancer is when a virus evades the immune surveillance, resulting in persistence of the viral infection.

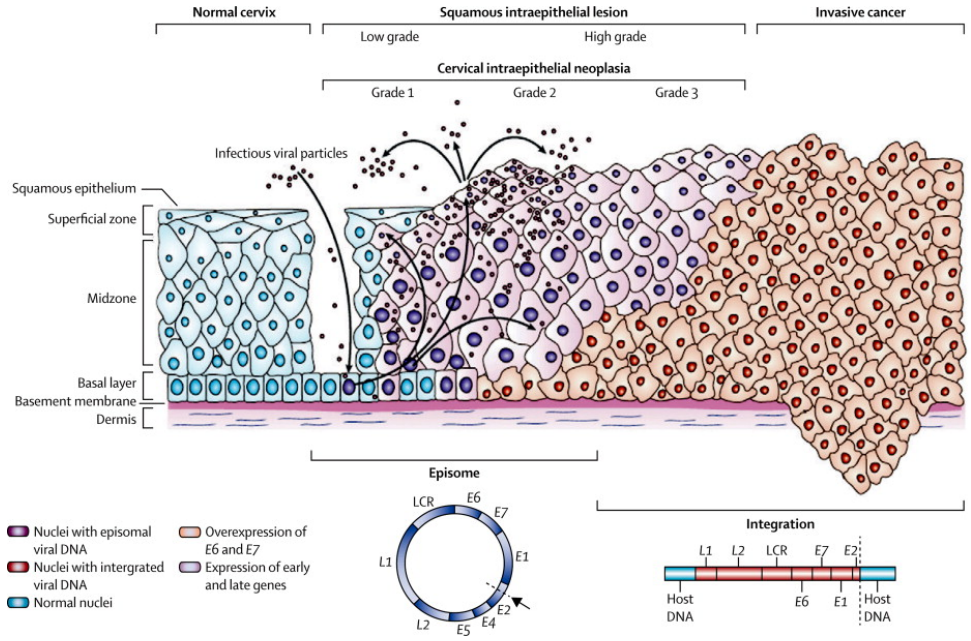

Figure 1: HPV mediated carcinogenesis in cervical epithelium: integration of viral DNA[7]. This mechanism corresponds to HPV related carcinogenesis in HNSCC.

1.2.1 Differences between HPV$^+$ and HPV$^-$ tumours

The HPV virus induces different mutations than the classical risk factors. Alcohol and tobacco induced tumours are characterized by TP53 mutation[8] and in 92% of HPV$^-$ tumours, the epidermal growth factor receptor (EGFR) is overexpressed[9]. If damage to the genome is excessive or other conditions within the cell are sub-optimal, p53 (the protein encoded by TP53) can intracellularly transducer these signals leading to halt in the cell-cycle progression[10]. EGFR associated pathways are linked to cellular apoptosis, proliferation, invasion, metastasis and angiogenesis. Additionally, in 70%, cyclin dependent kinase inhibitor (CDKN2A) is inactivated, which encodes the p16 protein[11].

In HPV related carcinogenesis, shown for cervical cancer in figure 1, viral DNA is integrated into the host DNA. Viral oncogene E6 induces p53 degradation and therefore substantial loss of p53 activity making the cells susceptible to genomic instability[12]. E7, a differnt viral oncogene, leads to cell cycle disruption by inactivating pRB, the retinoblastoma tumour suppressor gene product[13]. The RB protein integrates signals from outside the cell to decide if a cell can proceed in the cell-cycle of growth and division[10]. Furthermore, HPV$^+$ tumours often have intact p53 and are therefore more sensitive to restore apoptotic function[13].

One of the molecular hallmarks of HPV related tumours is considered the p16 protein which is found to be overexpressed in 96% in the HPV^+ tumours whereas it is inactivated in 70% of HPV^- tumours. The p16 overexpression is a result of pRB inactivation, thus caused by the viral oncogene[14]. HPV positive status of a tumour can be determined by performing polymerase chain reaction (PCR) on a biopsy to test for virus particles. However, because p16 overexpression is so strongly correlated with HPV positive tumours and the simplicity of the immunohistochemistry, p16 status is often used for preliminary staging of the tumour. Surprisingly, p16 positive status predicted improved survival independent of HPV PCR outcome[15].

Additional to these genetic differences; patients with HPV positive tumours represent a different population in the head and neck cancer patients. These patients are generally younger and more vital at diagnosis, have better oral hygiene and less field cancerization. Lastly, the absence of smoking is a positive influence on survival independent on HPV involvement[14].

1.2.2 Treatment deintensification

There have been studies to possibilities of reducing treatment in patients with HPV positive tumours and therefore the morbidity. It is suggested by Kelly et al.[16] that the de-intensification of the radiotherapy and/or chemotherapy dose may result in less toxicity while maintaining survival rates. They do suggest that a drop in survival rates should be avoided by appropriately selecting patients, for example based on pack years, lymph node status and size of the primary tumour. This is highlighted in a recent study of Gillison et al.[17] where cetuximab showed to be an inferior concomitant chemotherapy compared to cisplatinum in tumours with clinical TNM stage N2a or higher, or T3 or higher.

As of 2017 there is a different TNM staging for p16 positive tumours, which is mostly based on the association of the HPV positive tumours with extended lymphadenopathie, yet no treatment strategies are adjusted.HPV oncoproteins in oropharyngeal carcinomas demonstrated both direct and indirect induction of vascular endothelial growth factor (VEGF) expression[18]. Therefore it is hypothesized that one of the factors explaining the better response to treatment of HPV positive tumours is the distinct biology. Yet it is still not known how this distinct biology is related to a better prognoses.

Differences in tumour microenvironment of HPV^+ tumours could cause a better treatment response and higher survival.

1.3 Tumour microenvironment

Obtaining a tissue specimen by biopsy is still the golden standard in diagnosing a tumour and determining TNM stage. It is an invasive procedure for each patient and when imaging is planned after, the diagnostic accuracy can be influenced. Even though mutation analysis can take place in such a specimen, most treatment decisions are currently based on clinical presentation because of the limited knowledge of differences in underlying tumour biology.

In an extensive review, Hanahan and Weinberg[10] elaborated on biological capabilities a cell has to acquire in order to develop into a tumour. As visualized in figure 2, ten hallmarks of cancer are defined and the drugs designed to target these. The disease is characterized by the genomic instability initiating a diversity in mutations. What is previously thought as a collection of homogenous cells is now viewed as a complex tissue of individual specialized cells. Furthermore, indications are found, like the bi-directional stimulation of tumour-associated-macrophages and cancer cells, that the manifestation of high-grade malignancies cannot be characterized entirely on basis of mutations[10]. Therefore, the term tumour microenvironment is introduced to depict all the different aspects of a tumour.

It is proposed that the complex physiology of the tumour microenvironment can be better understood using non invasive imaging methods that allow us to image the whole tumour instead of the fragment

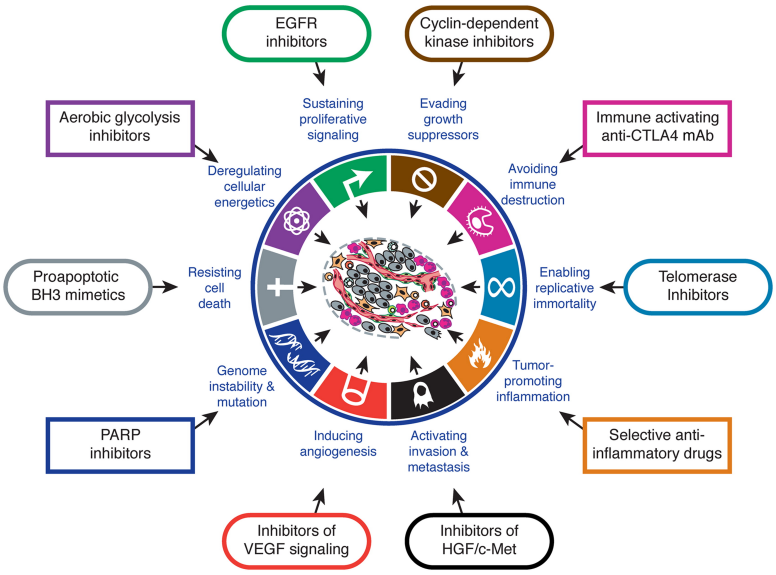

Figure 2: The hallmarks of cancer, as defined by Hanahan and Weinberg[10]

provided by biopsy. Characterization of the microenvironment with imaging could also help us to identify potential targets for future therapeutic strategies to monitor these while still in clinical trials as well as allow us to gain insight in the origin of differences in therapy responses. Furthermore, this improved understanding may lead to possibilities in (de-)intensify while treating with chemotherapy or radiotherapy, which might avoid unnecessary side effects of ineffective treatments.

Differences in the tumour microenvironement can be asessed with multimodal imaging.

1.3.1 Imaging modalities

To investigate the different aspects of the tumour microenvironment, different imaging modalities show potential. Positron Emission Tomography (PET) scans are a method of imaging physiological processes targeted by a specific radiolabeled tracer. When a positron emitted by a nucleus is annihilated by interaction with a free electron, two 511-keV gamma photons are emitted at 180° to each other. PET cameras have several rings of detectors, opposing detectors can identify a pair of rays emitted within a set time frame to measure annihilation. A low dose computed tomography (CT) scan is used to provide attenuation correction for the PET and to help localizing this occurrence more accurately within the body.

Uptake of a tracer within a tissue is mostly quantified with a Standard Uptake Value (SUV). This value is a decay and weight corrected representation of the activity within a region.

$$SUV = \frac{radioactivity\ concentration\ (kBq/mL)}{injected\ radioactivity\ kBq/weight(kg)} \tag{1}$$

CT is a fast, an widely available tool for diagnosing a wide variation of diseases. Often, iodinated contrast is used to better distinguish between tissue by enhancing the visibility of vascular structures, especially in oncology. Dynamic contrast enhanced CT, also referred to as CT perfusion, is an imaging technique used to assess intravascular distribution of contrast within regions of interest after the injection of a fast iodinated contrast bolus. On basis of this distribution, quantitative parameters describing the blood volume, flow and permeability of the vasculature can be calculated, reflecting aspects of the tumour microenvironment.

1.3.2 Biomarker imaging

Various PET tracers have been studied in HNSCC to predict response to (chemo)radiation and local recurrence. A better understanding of the complex physiology could allow us to gain more insight in the origin of differences in therapy responses and for identification of potential targets for future therapeutic strategies to avoid unnecessary side effects of ineffective treatments. Several studies are currently focusing on identifying the most optimal imaging biomarker of the tumour microenvironment to more accurately predict patient outcome. For example, CD44 (a transmembrane glycoprotein, cell surface adhesion receptor) blocking immunotherapy is being developed to reduce the metastatic potential of cancer regulated by CD44 mediated cell proliferation, migration and angiogenesis[19]. To identify targeted uptake, anti-CD44 antibodies labelled with ^{89}Zirconium were tested in a phase I immuno-PET study[19]. Another example is epidermal growth factor receptor (EGFR) imaging; ^{18}F-MPG PET has high specificity to activating EGFR mutant kinase to help identify an effective tyrosine kinase inhibitor[20] and ^{64}Cu-DOTA-cetuximab PET can help select, determine the dose and monitor the right patients for EGFR-targeted therapy[21].

In HNSCC, several hypoxia-related biomarkers are studied to investigate therapy outcome[22, 23, 24]. During hypoxia, radiotherapy can form less oxygen radicals and therefore resistance can be developed, additionally, hypoxia contributes to tumour progression by inducing tumour angiogenesis[25], changes in genetic mutations[26] and adaptation to a hypoxic environment represents more aggressive tumour phenotypes[27]. However, [^{18}F]-FAZA PET, designed to image hypoxia, could not help to definitively confirm a link between decreases prognosis and hypoxia[22]. It can be hypothesized that an increased radiosensitivity of tumours might not only be caused by hypoxia, but possibly also by changes in endothelial activation and tumour perfusion.

Angiogenesis Knowledge of underlying mechanisms and signalling pathways contributing to response to therapy is still limited, it is hypothesized that changes in endothelial activation and tumour perfusion can be of influence. Angiogenesis, one of the hallmarks of cancer defined by Hanahan and Weinberg[10] is the formation of new blood vessels from pre-existing ones. This process plays is upregulated in an early phase of tumourigenesis and plays a crucial role in tumour growth and progression. In order to grow beyond the size of 1-2 mm, the formation of new blood vessels in a tumour is required to facilitate the supply of oxygen and nutrients and dispose of waste[28]. When a growing tumour mass results in hypoxia, this angiogenic balance is tipped to pro-angiogenesis and a cascade of events is initiated. This angiogenic switch is typically associated with the progression from a benign to malignant stage[29]. One of the most important mediators in signaling during angiogenesis are the transmembrane protein family of integrins; integrin-mediated signaling affects cell survival, migration and invasion according to the appropriate microenvironment[28]. Integrins recognize the RGD sequence expressed on proteins, and by synthesizing this sequence, a suitable imaging agent can be developed. [^{68}Ga]Ga-DOTA-$(RGD)_2$ is a PET/CT tracer developed to bind integrin $\alpha_v\beta_3$, overexpressed at an early phase of angiogenesis. Exposure to persistent stimulatory signals results in tortuous vessels that are highly permeable causing irregular blood flow and vascular leakage. Imaging angiogenesis with the help of an RGD tracer thus does not provide a complete overview of the amount of blood flowing through the tissue and reaching the tumour cells whereas CT perfusion imaging can.

^{68}Ga-$(RGD)_2$ PET/CT and CT perfusion can provide insight in the differences in tumour microenvironement between HPV$^+$ and HPV$^-$ tumours.

1.4 Research aims

Multiple studies have unsuccessfully tried to link the substantial improved survival of HPV related OPSCC to several (imaging) biomarkers. Furthermore, treatment personalization on basis of HPV status is not used to its full potential. Therefore the need is identified for more knowledge of the differences in tumour microenvironment. A distinctive factor may include changes in endothelial activation before and during the treatment induced inflammatory response. In this research, uptake of [^{68}Ga]Ga-DOTA-(RGD)$_2$ and CT perfusion parameters in OPSCC are correlated to the HPV status of this tumour and to the FDG PET/CT and MRI scan made as part of standard diagnostics.

1.4.1 Study aims of PIVOT study

The PIVOT study (PET Imaging of Vasculature in Oropharyngeal Tumours) was set up to use multimodal imaging to improve the knowledge of differences in tumour microenvironment. 10 Patients with HPV$^+$ and 10 patients with HPV$^-$ OPSCC will be included in the clinical study when receiving a curative set up of chemoradiotherapy. Primary study aims are:

1. To assess the differences in baseline tumour uptake values of ^{68}Ga-(RGD)$_2$ between HPV$^+$ and HPV$^-$ tumours.
2. To assess the differences in baseline tumour perfusion between HPV$^+$ and HPV$^-$ tumours.
3. To determine the changes in ^{68}Ga-(RGD)$_2$ before the start and in the second week of treatment within all patients.
4. To determine the changes in perfusion before the start and in the second week of treatment within all patients.
5. To correlate the differences in ^{68}Ga-(RGD)$_2$ and perfusion to HPV status of the tumour.

The secondary study aim is to explore the differences in ^{68}Ga-(RGD)$_2$ and perfusion between patients with locoregional control and patients with locoregional recurrence within one year.

1.4.2 Aims and outline of this thesis

At the time writing this thesis, one patient completed the study scans, therefore the research questions in this thesis are different than the main questions of the PIVOT study. Furthermore, during my graduation internship much attention was paid to the set-up and CMO application of this study. Therefore, the study design will be discussed more extensively in this thesis and the CMO application will be discussed in the appendix, in the 'Verantwoording' of my graduation.

This thesis deals with characterizing of the tumour microenvironment of HPV positive and negative HNSCC. Of two imaging methods, the different protocols are evaluated and the most accurate protocol and analysis methods are chosen. First, a analysis of dynamic RGD uptake in patients with HNSCC in the radboudumc are discussed in **Chapter 2**. Different approaches to analyze the uptake within regions of interests are discussed and compared. Furthermore, tracer uptake within the tumour and background tissue in the head an neck region is evaluated to determine the most accurate tumour to background imaging time point.

CT perfusion scans can be used to calculate the amount of blood flow over time within a region and the permeability of the vessels. The different aspects of this complex but innovative technique and the proposed optimal acquisition protocol are discussed in **Chapter 3** as well as the influence of different analysis methods.

These two imaging techniques are used in a prospective study to research the tumour microenvironment in OPSCC described in **Chapter 4**. In the introduction and method, a feasible study design is outlined and on basis of some preliminary results, a conclusion is drawn.

These Chapters discuss different aspects of my graduation internship and therefore, **Chapter 5** is used to discuss the results of my graduation. The preliminary differences between the baseline and follow-up scans of the subject included in the PIVOT study are discussed as well as some recommendations for future analysis. Conclusions that can be drawn from this work are elaborated.

The research questions that will be answered in this thesis are:

- Chapter 2: What is the best method of VOI selection for quantitative PET analysis?
- Chapter 2: Can a HNSCC tumour be distinguished from the background with RGD PET/CT and what timeframe would be most suitable for tumour qunatification?
- Chapter 3: What is the best method to calculate blood flow, volume and vascular permeability with CT perfusion?
  - What is the most optimal calculation model?
  - What is the most optimal CT perfusion scan setting?
- Chapter 3: Is CT perfusion feasible in the Radboudumc?
- Chapter 4: Is it feasible to assess the tumour microenvironement with RGD PET/CT and CT perfusion in OPSCC?
- Chapter 5: What could the preliminary image analysis results imply for the tumour microenvironment?
- Chapter 5: What would be recommendations and future prospects of imaging the tumour microenvironment?

.

2

Dynamic ^{68}Ga-RGD$_2$ PET/CT analysis

^{68}Ga-RGD$_2$ is a newly developed PET/CT tracer that allows us to image integrin $\alpha_v\beta_3$, upregulated during an early phase of angiogenesis. Different methods of delineating a tissue on PET/CT scans are defining a volume of interest re discussed, and on basis of this conclusion the tumour to background PET signal in the first 60 minutes post injection of the RGD tracer is analyzed to determine the optimal time frame for imaging.

2.1 Introduction

2.1.1 Angiogenesis

Angiogenesis is an important process assisting in tissue growth and regeneration. Imbalance of the process can lead to angiogenic disorders, immunodeficiencies, inflammation and cardiovascular pathology[30]. In tumorigenesis, tumours cannot grow beyond $1-2mm$ in size without the induction of angiogenesis and thus the blood vessel supply of oxygen and nutrients and dispose of waste and carbon dioxide[28]. During the process of angiogenesis, new blood vessels are formed from existing vessels. Several angiogenesis pathways have been identified: In early phases of tumour expansion vessel co-option can be used where tumour cells grow towards the nearest blood vessel when expansion is restricted by oxygen, nutrients and growth factors[31]. Further increase in tumour size results in central hypoxia that evokes the upregulation of multiple angiogenic factors, from which Vascular endothelial growth factor (VEGF) is thought to be the most important[32]. Tumours can remain dormant for a prolonged period in this state until an angiogenic switch is activated, after which a strongly angiogenic state and accelerated growth is initiated[33]. This switch is correlated with tumour progression from benign to a malignant stage and is associated with endothelial cell activation, proliferation, migration, increased vascular permeability and basement membrane dissolution[34]. Cells identified in helping trigger this angiogenic switch are cells of the innate immune system like macrophages, neutrophils, mast cells and myeloid progenitors.[10] Pathological angiogenesis is paired with invasion of these cells which assemble at the margins of premalignant lesions or tumours[10]. Additionally, these cells can protect the neovasculature from anti-tumour drugs or endothelial cell signaling[10].

VEGF, released in an hypoxic, inflammatory microenvironment or by oncogene signalling can be sensed by quiescent vessels[32]. Consecutive degradation of the basement membrane is mediated by matrix metalloproteases (MMP) and endothelial cells (EC) detach from their junctional adhesion to neighbouring cells. The ECs sprout towards the pro-angiogenic factors, including cytokines and growth factors, released by the tumour[28]. Endothelial cells can migrate onto the extracellular matrix (ECM) surface in response to integrin signalling. Even though initially, the tumour is provided with more oxygen and nutrients, tumour endothelial cells are structurally abnormal. Exposure to persistent stimulatory signals result in improper vessel function: Excessive fenestrations, loosened intercellular junctions multilayered endothelia and uneven surfaces cause irregular blood flow and vascular leakage[29]. Furthermore, in comparison to normal quiescent tissue, endothelial cells in tumours have a unique activated phenotype.

2.1.2 Integrins

Adhesion to the ECM is primarily mediated by integrins, a family of heterodimeric transmembrane proteins important in the angiogenic cascade[32]. Growing endothelial cells can bind to matrix proteins in the tumour microenvironement, such as vitronectin and fibronectin through their amino acid Arg-Gly-Asp

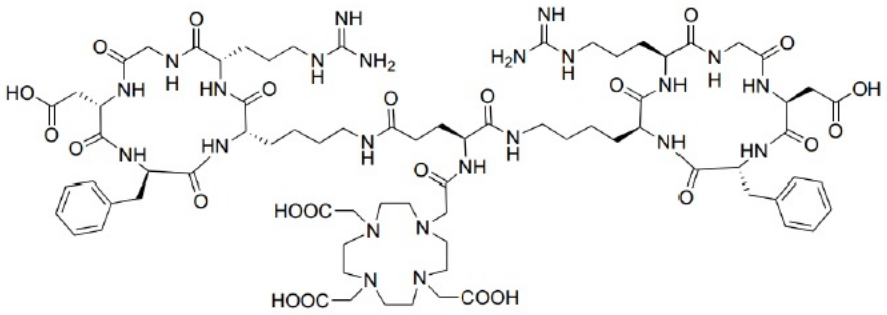

Figure 3: Structural formula of DOTA-E-[c(RGDfK)]$_2$

(RGD) sequence, by upregulation of integrin $\alpha_v\beta_3$ and $\alpha_v\beta_5$[35]. These integrins can interact in a bi-directional manner between endothelial cells and the ECM. By binding growth factor or cytokine receptors, the appropriate microenvironment of the EC can be assessed and accordingly, cell survival, migration and invasion can be stimulated. Also, integrin-mediated regulation of interactions between endothelial cells and the basement membrane promotes vessel maturation, provides survival cues and traction for invading endothelial cells[32]. Integrin $\alpha_v\beta_3$ is overexpressed on angiogegenic blood vessels during an early phase of angiogenesis[28] and can also be expressed on human tumours such as renal cell carcinomas[36], gliomas[37], ovarian carcinomas[38] or melanomas[39]. Furthermore, expression is associated with increased tumour growth and metastasis[28]. In vivo HNSCC tumour models showed that integrin $\alpha_v\beta_3$ was not necessarily expressed on tumour cells[40] which makes HNSCC one of the few tumour types where radiolabelled RGD, designed to target integrin $\alpha_v\beta_3$, can be used to monitor angiogenesis. Radiolabelled RGD is shown to target [41].

2.1.3 Previous studies with RGD imaging

Multiple radiolabeled RGD peptides have been researched, from which the most extensively studied is ^{18}F-Galacto-RGD. Even though this monomer peptide showed good results, in preclinical studies it is shown that tumour uptake of dimeric RGD peptides, with two binding sites for integrin $\alpha_v\beta_3$, is higher due to enhanced affinity for this integrin[42]. To identify a stable radiolabelled RGD peptide for PET imaging, four ^{68}Ga-labelled multimeric RGD peptides with good in vivo imaging characteristics were comparatively studied[43]. Imaging and biodistribution data showed tumour specific uptake for each of the four tracers. Considering tumour accumulation, tumour-to-blood radio and uptake in normal tissues, [^{68}Ga]Ga-DOTA-E-[c(RGDfK)]$_2$ is considered a suitable PET imaging agent with adequate and selective binding activity to integrin $\alpha_v\beta_3$[44]. A first in human injection of ^{68}Ga-RGD$_2$ was done in 2016, as part of a feasibility and safety study in five subjects with HNSCC[45]. A fast blood clearance was concluded and in the 22 subjects currently included in multiple studies with the RGD compound in the Radboudumc, no drug related adverse events were identified.

2.1.4 Research aims

To further investigate the pharmacokinetics of the ^{68}Ga-RGD$_2$ tracer, dynamic scans from injection until 60 minutes post injection (p.i.) are studied in more detail. To accurately determine the uptake within a structure, different methods of creating a volume of interest (VOI) are discussed to determine the best method for quantitative PET analysis. Furthermore, on basis of this conclusion, the uptake pattern of ^{68}Ga-RGD$_2$ is evaluated: It is assessed if the tumour can be distinguished from the background with RGD PET/CT and what timeframe would be most suitable for tumour quantification. A suitable time frame will have to meet certain demands: A good tumour-to-background ratio should be obtained as a result of scanning at the right moment after injection and scanning duration, additionally, subject comfort should be taken into account in terms of short incubation and scanning time.

2.2 Method

In a prospective study by Lobeek et al.[45], five subjects (2 female, 3 male) with a proven squamous cell carcinoma of the oral cavity were scanned with a dynamic PET/CT protocol. For $60min$ after start of injection, list mode PET scans were acquired with a Biograph 40 mCT scanner (Siemens Medical Solutions, Knoxville Tennessee, USA) of the head and neck region with time of flight (TOF) reconstruction (75 slices of $3mm$, reliable field of view (FOV) of $16cm$). Low dose CT scans were acquired for anatomical reference and attenuation correction (112 slices of $2mm$). Reconstruction of the list mode images consisted of 33 frames ($1x40s, 10x5s, 3x10s, 2x15s, 5x30s, 5x120s, 5x300s$,and$2x600s$). One subject underwent dynamic imaging for $25min$ instead of 60. Eligible subjects had a tumour diameter of at least $1.5cm$, classified on basis of an MRI or CT within four weeks prior to the screening visit and were planned for surgical resection 2-7 days after scanning. Contra-indications were pregnancy, breast-feeding, severe claustrophobia, other serious illness and/or impaired renal or liver function. Pathologic staging after resection concluded TNM stages without distant metastases (M0): pT4aN2b, pT2N1, pT4aN2b, pT2N1, T4aN2b. DOTA-E-$[c(RGDfK)]_2$ was synthesized according to the good manufacturing practice regulations for human use. Radiolabelling and quality control was performed in house. The subjects had no intake restrictions based on food or medicine. ^{68}Ga-RGD_2 was injected intravenously using a slow bolus injection of $8ml$ over $40s$ (208.7 ± 7.5 MBq).

2.2.1 Segmentation methods

To obtain an accurate VOI for the tumour but also for the background reference tissue, nine methods of defining a VOI were tested with the help of PMOD medical imaging program version 3.15 (PMOD technologies LLC, Zürich, Switzerland) which are listed in table 1. This was done with the CT scans for the first 7 methods and PET scans for the 8^{th} and 9^{th} method of subject 1. The tumour and carotid artery were delineated and as reference background tissue with high uptake, the contralateral parotid and the nasal septum were delineated, for the low-uptake reference, a VOI was drawn in the brain and contralateral sternocleidomastoid muscle. In the software a VOI could be drawn on each separate axial slice. In the coronal and sagittal slices, broad delineation was done and used as reference to adjust the axial delineation.

Table 1: Multiple methods can be used to define a volume of interest. The 9 segmentation methods used in this study are listed in this table.

no.	Method
1	Manual contour - not moved
2	Manual contour - moved in frame 26-31
3	Manual contour - half of the volume
4	Sphere with radius $5mm$
5	Sphere with radius $10mm$
6	Threshold 50% SUV_{max}, on basis last frame segmentation 1
7	Threshold 50% SUV_{max}, on basis each frame segmentation 1
8	Automatic contour on basis of last PET time frame
9	Automatic contour on basis of average PET of all time frames

Segmentation 1 of 9 was a delineation on basis of manually contouring the structure, this was copied to the PET scans from which the activity data was acquired per time frame. For segmentation 2, this VOI was placed on the PET but than, without adjusting the contour, moved to the location on the PET most likely to be the tissue. Because this subject moved most during the last frames, in these frames the location was adjusted: For frame 1-25, the location was the same as frame 25, in frame 26-28 the

VOI was moved without adjusting the contour. To simulate observer variance, half of the volume of the contour VOI (segmentation 2) was extracted in order to obtain segmentation 3.

A predefined sphere was placed in the region of interest for segmentation 4 and 5, such a sphere would reduce the effects of interobserver variability. Segmentation 4 was a sphere with a radius of $5mm$, placed in the middle of the reference tissue and segmentation 5 was a sphere with a radius of $10mm$ placed to include most of the reference tissue as possible.

The 6^{th} and 7^{th} segmentation methods were obtained by the setting in PMOD in which a relative threshold of 50% of the SUV_{max} was used on basis of the reference VOI of segmentation 2, as is a suggested method of Kao et al.[46]. For segmentation 6, the threshold of 50% of the SUV_{max} was set on basis of the last frame. For segmentation 7, this threshold was set for each time frame separately.

The last two segmentations were completely based on the PET images. For segmentation 8 the PMOD function 'generate contour' was used on the frame of the last time point. With the help of this function, the software draws a contour automatically on basis of differences in SUV values, when an observer clicks in the center of the region of interest. For the 9^{th} segmentation, this function was used on a PET image generated by PMOD in which the average of all frames were combined in one image.

2.2.2 Determining tumour-to-background

On basis of the previous paragraph, different segmentation methods can be used for different tissue in all five subjects. The contralateral parotid, as high background reference, and the blood vessels were delineated on basis of segmentation 2. A sphere was placed in the low background reference; the contralateral dorsolateral musculature on the CT. The volume was $14.2ml$, as this was the largest sphere that could be placed in this area in all subjects. These VOIs were subsequently copied to the dynamic data set. Finally, the tumour was delineated on basis of previous delineation done before my internship.

A one way ANOVA statistical test was done in order to check if the values found in the five subjects are comparable and specifically if the SUV values of the tumour are comparable.

2.3 Results

2.3.1 Segmentation methods

The activity within the tumour for the different methods of VOI selection are visualized in figure 4. The highest average in the tumour was achieved when drawing a sphere with a radius of $5mm$ within the center of the tumour. The highest activity within the other three tissues was obtained when using segmentation method 6. The lowest activity within the tumour and parotid gland was measured when the VOI in the last frames was not moved to correspond to the displacement of the subject. For the carotid artery, the lowest activity was measured when segmentation method 5 was used and for the muscle segmentation method 8 and 9.

Table 2: Average and maximal activity kBq/cc during the frame $900s$ to $1200s$ p.i.

	Subject 1		Subject 2		Subject 3		Subject 4		Subject 5	
	Av	max	av	max	av	max	av	max	av	max
Carotid artery	3.0	4.6	4.0	7.2	4.1	6.8	3.4	6.0	4.2	8.1
Jugular vein	3.1	4.9	3.4	5.3	4.1	7.3	3.9	6.5	3.9	6.8
Parotid gland	3.4	5.1	6.1	10.5	4.3	7.2	5.2	7.6	5.3	8.4
Muscle	2.0	3.3	2.3	4.9	1.9	3.7	2.2	3.9	2.0	2.9
Tumour	7.4	12.1	11.4	21.5	8.8	14.0	8.8	17.1	9.0	15.9

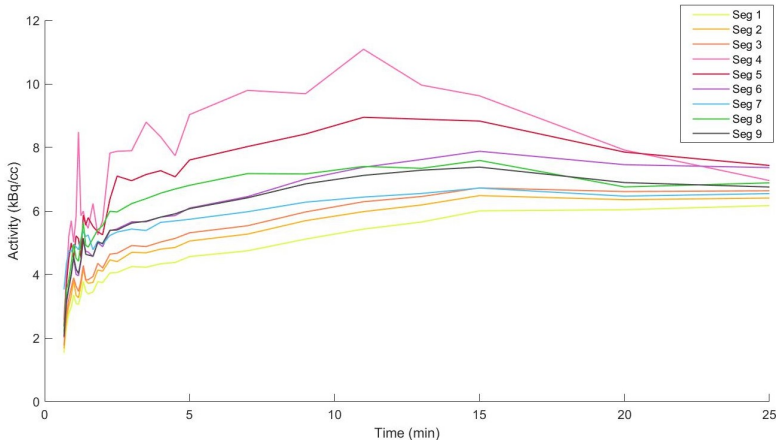

(a) Tumour

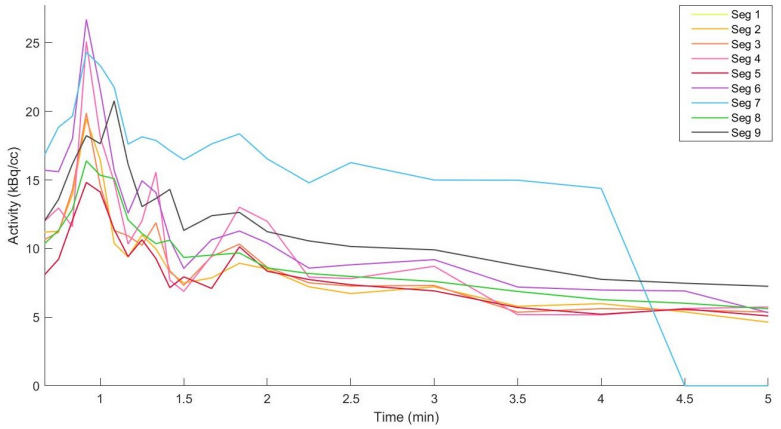

(b) Carotid artery

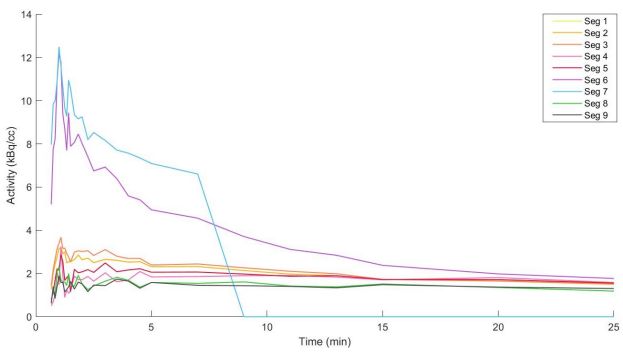

(c) Muscle

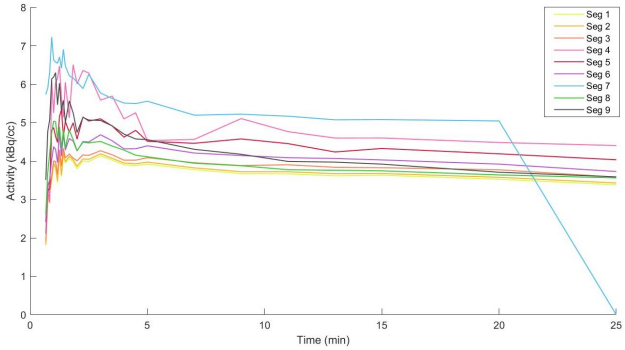

(d) Parotid gland

Figure 4: Activity within the three different structures until 60 minutes post injection of ^{68}Ga-RGD$_2$, the activity within the carotid is plotted until 5 minutes post injection. The mean activity based on the different segmentation (seg) methods is plotted.

2.3.2 Determining tumour-to-background

All primary tumours could be identified by heightened ^{68}Ga-RGD$_2$ uptake. The average uptake was higher than the background tissue from about 5 *min* p.i. The mean volume of the VOIs of the subjects were 2.86*ml* for the carotid artery, 5.24*ml* for the jugular vein, 22.44*ml* for the parotid gland and 14.2*ml* for the sphere in the dorsolateral musculature. The volume of the VOI drawn to segment the tumour for subject 1 was 23.8*ml*, subject 2 9.9*ml*, subject 3 8.1*ml*, subject 4 7.1*ml* and for subject 5 17.6*ml*.

The activity within the carotid artery and jugular vein was comparable for all five subjects (table 2).

The activity within the dorsolateral musculature was highest for subject 2 and lowest for subject 5 until 900s p.i., after which the uptake was similar for all subjects. In the parotid gland, subject 2 had the highest uptake, at 900 p.i. the highest and lowest uptake differ a factor 1.8.

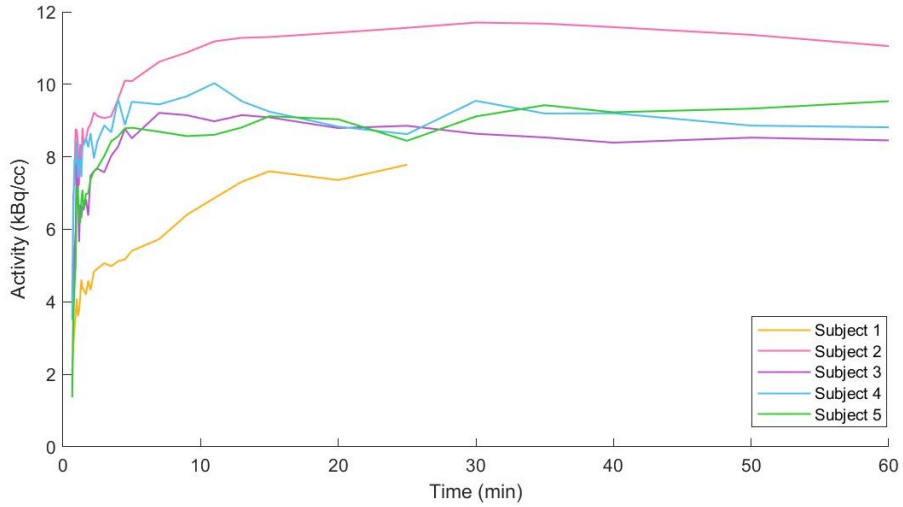

Figure 5: The mean activity within the tumour for the five different subjects, data is presented as cumulative activity and the end of each time frame.

In figure 6, the mean activity of subjects 2-5 within the five different VOIs are shown. The initial peak of activity in the carotid artery and jugular vein took place in the first 1.5min after which the slopes flattens until 5min p.i. and the steady state begins around 15min. For the background tissue, the plateau phase begins at 5min p.i. The average activity in the tumour of these four subjects is plotted in figures 7. The slope of subject 2 reached a steady state after 15min p.i. The activity located within the other three tumours stabilized after 5min p.i. When comparing the tumour to the signal from the background and the blood pool, the mean activity within the tumours of the four subjects was higher than the blood pool signal after 3.7min p.i.

When plotting the activity within the tumour for all subjects in figure 5, the mean activity within the tumour of subject 1 was much lower at every time point than of the other subjects, also when comparing the maximal uptake. In the parotid gland, the activity was also lower and in the carotid artery and jugular vein the activity was slightly lower. In the muscle, subject 5 has the lowest mean activity. The tumour of this first subject was the largest of the five. The tumour of subject 2 had the highest mean uptake after the initial phase, differing a factor 1.5 from the first subject, and has the third largest volume.

When using One Way ANOVA test on basis of the mean SUV values of the tumour, these did not significantly vary ($P < 0.05, P = 0.4060$). When using One Way ANOVA to test for significant differences between all five VOIs of all five subjects, significant differences were found ($P = 0.0198$). These significant differences ($P < 0.05$) were found for subject 1 versus subject 2 when performing Tukey's post-test. No other combination of subjects varied significantly.

2.4 Discussion

In this study, the binding of the newly developed ^{68}Ga-RGD$_2$ PET tracer was investigated in oral squamous cell carcinomas. First, the methods of VOI segmentation are discussed and after that the optimal imaging time point for the scans.

The analysis program required segmentation of VOIs to be on CT or PET slices in one orientation and these could not be adjusted in the other orientations. The method used to overcome this was to draw a VOI on the axial planes and on basis of this delineation, sagittal and coronal VOIs were defined.

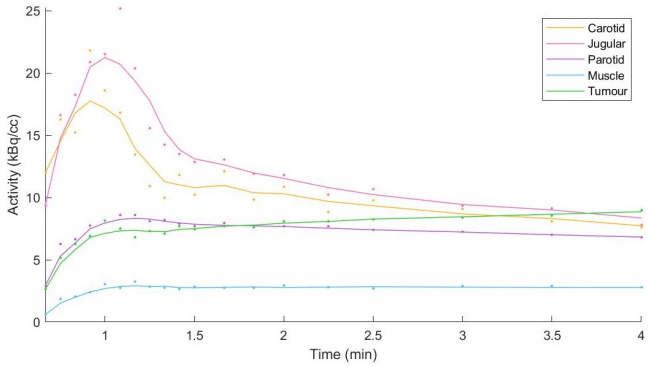

(a) Zoomed in from t=0-4 minutes

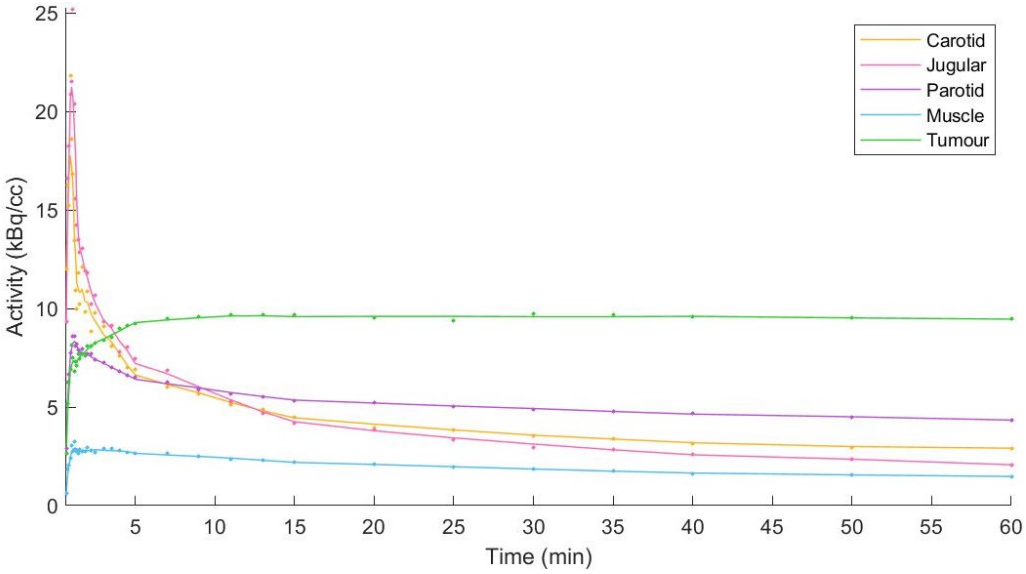

(b) t=0-60 minutes

Figure 6: A smoothed graph from the mean activity (dots, cumulative activity and the end of each time frame) within the different volumes of subjects 2-5

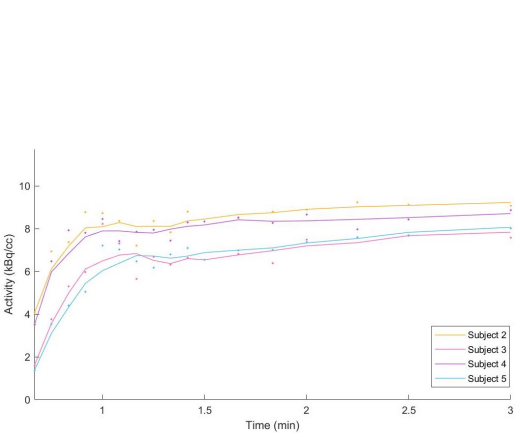

(a) Zoomed in from t=0-3 minutes

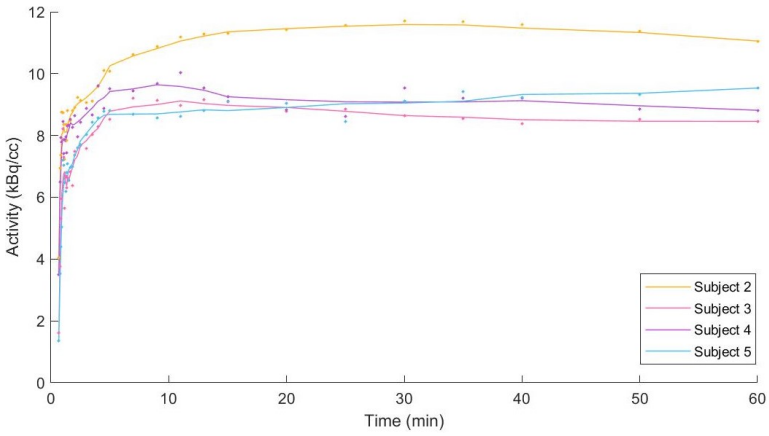

(b) t=0-60 minutes

Figure 7: A smoothed graph from the mean activity (dots, cumulative activity and the end of each time frame) within the tumour for the four different subjects

Using these last two VOIs as reference, the axial delineation was adjusted. Defining a new ROI on every subsequent slice is not only a time consuming method but can also lead to less precise delineation. By adjusting the axial delineation on basis of sagittal and coronal VOIs, the error marge is prevented as much as possible.

The spatial resolution, the full width at half maximum of Gallium-68 imaged with a human PET/CT scanner (Siemens Biograph 64), is estimated to be $7.0mm$ by measuring point spread functions at the center of the FOV using a $0.5mm$ diameter capillary[47]. The partial volume effect becomes important when a VOI is below two times this resolution; $2.74ml$. The sphere with a radius of $5mm$, and therefore a volume of $1.05ml$, is well below this cut off point which can explain the fluctuation in the mean activity in figure 4. The mean volume of the carotid artery VOIs, $2.86ml$, is just above this cut-off point. No such fluctuations as with the sphere of $5mm$ were observed in the carotid artery and therefore these are likely not influenced by this effect.

2.4.1 Segmentation methods

The different methods of VOI selection were tested on subject 1. As can be concluded from figure 5, the tumour uptake of this subject was much lower than in the other subjects, which could have influenced the activity measurements. The uptake in the parotid gland was also lower within this subject yet the activity located within the blood and musculature were comparable. Even though these values only varied significantly from subject 2, on MRI the tumour showed a distinct morphology as compared to the other subjects: A severe inflammatory process surrounds the tumour tissue. In inflammation, angiogenesis is also active, but it is expected that non-tumour endothelial cells express a lower concentration of integrin $\alpha_v\beta_3$. The inflammation surrounding the tumour was included in the tumour VOI but had a lower SUV value than tumour tissue and therefore resulting in underestimation of tumour SUV.

When delineating a tissue on basis of the CT, it is important to know whether the subject has moved between or during the CT and PET scan. This is highlighted by the underestimation of uptake measured in the tumour when using segmentation method 1, where the location of the VOI was not adjusted even though the subject moved between the CT and last frames of the PET scan.

A delineation is always observer dependent. Some methods, like a contour delineation are more dependent than a sphere with or without a pre-defined diameter. Nonetheless, a sphere is not an accurate representation of a non-spherical tissue. To overcome the partial volume effect, the sphere radius should be at least $0.81mm$ and preferably larger. Secondly, when a tissue is bigger than this sphere, the sphere will include the center of the tissue with often a higher activity than the not-included edges, as was the case with segmentation method 4 in the tumour and parotid gland. Contrarily, when the tissue is smaller than the sphere, the VOI will include background tissue and therefore the mean will underestimate the activity as was the case with segmentation method 5 in the carotid artery. In a tissue with little uptake variation between the edges and the center, like muscles, a sphere can be used to make a good estimate.

All delineation methods resulted in different sizes of the VOI and different parts of namely the periphery that were or were not included in the VOI, resulting in a higher or lower activity within a tissue with inhomogenenous uptake on all time points. However, for tissue with lower uptake, or with an artery running through the structure, a delineation on basis of a cut-off activity of 50% of the hottest voxel, will result in a large overestimation. Segmentation 6 and 7 overestimate the activity within the muscle especially during the arterial inflow of tracer. Even in tissue with higher activity like the carotid artery and parotid gland, segmentation method 7 overestimated the first part (arterial inflow) of the graph and underestimated the second part. Contrarily, this method did not affect the graph of the tumour.

The activity within an automatically generated contour, segmentation 8 and 9, did not really variate much from other segmentation methods. In the muscle these do resulted in a lower steady state than when using segmentation method 1-5.

Additional to these 9 segmentation methods, also methods on basis of a fixed SUV threshold are described in literature[46, 48]. However, these fixed thresholds are investigated thoroughly for FDG PET/CT scans. Considering that uptake of this specific RGD compound is not broadly described in

literature and before this dynamic study no mean SUV value was known for this specific tracer, it is difficult to decide which SUV value should be used as a cut-off point. Secondly, these fixed thresholds can not be used for background tissue, but only for tumours. Therefore, only relative thresholds were used in the segmentation analysis.

When delineating structures, the most important thing is that the VOI accurately represents the activity within the structure, also observer and PET scan characteristics should be kept in mind. Secondary considerations are the time it takes to delineate a structure, and comparison to literature. For example when contouring a whole lung for dosimetry this can be a time-consuming process even though in some tissues the segmentation method does not result in very different quantification, as could be concluded from segmentation methods 1-5, 8 and 9 in muscle tissue. Therefore, a choice can be made for a more time saving but still valid method. Moreover, it is important to be able to compare study results to other research done on the subject which is more accurate when a same segmentation method has been applied.

2.4.2 Determining tumour-to-background

Currently the smallest volume delineated was the carotid artery and as stated before the volume was just above the partial volume cut off. The reason this VOI was so small is that in some axial slices, this volume was very hard to distinguish from other tissue. Contrast-enhanced CT can make some of these discriminations more easy and therefore a larger part of the carotid artery can be contoured.

The external carotid artery runs close to the deeper lobe of the parotid gland and can influence the activity measurements when included in the VOI. Therefore, the deeper lobe of the parotid was not included in the VOI. Furthermore, within the spherical VOI in the dorsolateral musculature, also tendons, small fat planes and small arteries could be included that could have given an improper reflection of true muscle. When the sphere was copied to the PET image, effort was made to place it accurately to exclude blood vessels.

Comparison with different RGD-based tracers Few studies have been published about dynamic uptake of RGD tracers and corresponding tumour-to background ratios. Tumour-to-background ratios of ^{68}Ga-Galacto-RGD$_2$, ^{68}Ga-I2P-RGD$_2$ and ^{68}Ga-4P-RGD$_3$ in mice with glioma xenografts have been quantified in percentage of injected dose per gram of fresh tissue on 5, 30, 60 and 120 minutes p.i.[49]. The tumour-to-muscle ratios of ^{68}Ga-Galacto-RGD$_2$ were 2.92, 3.70, 6.74 and 4.67, for ^{68}Ga-I2P-RGD$_2$ 2.1, 4.37, 4.35 and 3.91 and for ^{68}Ga-4P-RGD$_3$ 1.55, 2.53, 4.10 and 2.56 for 5, 30, 60 and 120 *min* p.i. respectively, while overall tumour uptake was highest at 5*min* p.i. for ^{68}Ga-Galacto-RGD$_2$ and ^{68}Ga-4P-RGD$_3$[49]. The tumour-to-muscle ratio in our four subjects was 3.49, 5.28, 6.40 for 5, 30 and 60 *min* p.i. respectively and the mean tumour uptake was highest at 30*min* p.i. The values in this study were not corrected for grams of fresh tissue so no quantitative correlations of tumour-to-background can be acknowledged. Furthermore, our values were measured in humans instead of mice and in tumours of different origin with known integrin $\alpha_v\beta_3$ uptake on neovasculature in HNSCC instead of on tumour cells. Yet, the uptake pattern we saw in the dynamic scans is still similar to that of ^{68}Ga-Galacto-RGD$_2$ and ^{68}Ga-4P-RGD$_3$.

In eight patients with breast cancer, ^{18}F-FPPRGD$_2$ uptake in lesions was highest at 15 minutes, compared to 30, 45, 60 and 120 *min* after injection of the tracer[50]. The tumour, lymph node metastases and other metastases showed different ^{18}F-FPPRGD$_2$ uptake patterns: Cumulative activity decreased considerably over time without a steady state, contrary to our findings. This could possibly be due to a different compound or different tumour origin and consequential differences in $\alpha_v\beta_3$ expression. However, no uptake pattern of muscle tissue was defined for more accurate comparison or distinction between these two possible explanations.

In dynamic scans performed after injection of ^{18}F-Galacto-RGD in six HNSCC patients, a mean tumour-to-muscle ratio of 7.97 is found[51]. In a time activity plot, after rapid increase in tumour accumulation, a plateau phase in the tumour is observed after 10-15 *min* p.i. and subsequently only

minimal to no decrease in activity[51]. Both the high tumour-to-muscle ratio and the slope of the time activity curve can be matched to the data presented in this study.

2.5 Conclusion

The best method of VOI segmentation is dependant on multiple aspects, a manually drawn contour of a structure can best estimate the activity in all tissues but this is time-consuming and not always better than other methods. The placing of a sphere is only a good method for low-uptake tissue like muscles whereas a relative threshold works best in high-uptake tissue. Automatic generation of a contour works best in high uptake tissue and in low uptake tissue after the initial phase of arterial inflow of the tracer and when low noise is present.

The steady state of activity starts at 5 to 10min p.i. Even though the tumour to background ratio still increases after this time point, this is only minimal and subject comfort, for example shorter incubation time, should be taken into account. Additionally, in one subject, the steady state was only reached after 15min. Therefore, PET acquisition should take place from 15 tot 20min p.i. A list mode setting and imaging from 10 to 20min will ensure that different reconstructions of these PET images can be done when new insights are gained.

3
CT perfusion protocol

Another way to establish the angiogenetic capabilities of a tumour is by imaging the perfusion within tissue. A new oropharyngeal oncology CT perfusion protocol is being discussed in this chapter as well as methods that allow quantification of these scans. Furthermore, the feasibility of this scan protocol in the Radboudumc is assessed.

3.1 CT perfusion technique

Computed tomography (CT) has become an important diagnostic tool because of the wide logistic availability, low costs and wide spectrum of pathologies that can be investigated[52]. In oncology, iodinated contrast is often used to help distinguish between tissue during initial staging but also for monitoring response to therapy. CT perfusion, also called dynamic contrast enhanced (DCE) CT, is an imaging technique designed to not only assess the distribution of contrast within a tissue but also the exchanges between the blood and extravascular space. The passage of blood through the microcirculatory network of a tissue or organ is called blood perfusion[53]. Perfusion can also be assessed by DCE MRI protocols which have similar applications as DCE CT, however a clear distinction can be made on basis of characteristics of these imaging methods: Advantages of MRI are no ionizing radiation and non-limited z-direction coverage, whereas CT is more readily available and results in higher spatial resolution[54]. More importantly, in CT perfusion, a linear relationship between concentration of contrast and CT attenuation facilitates quantitative (versus relative) measurements[54].

The CT perfusion technique was developed about 40 years ago to quantify cerebral blood flow during an acute stroke[55]. Whereas with conventional contrast enhanced CT it is still difficult to separate malignant from benign lesions like cysts or hemangiomas, with the help of perfusion protocols lesions can be distinguished. The repetitive scanning of the tumour volume provides an opportunity to quantitatively assess several parameters related to the vasculature.

In this chapter the best model to calculate perfusion related parameters is discussed, dependent on this model the scan settings for a new oropharyngeal oncology CT perfusion protocol are assessed. Furthermore, the feasibility of using this CT perfusion protocol for this study is determined.

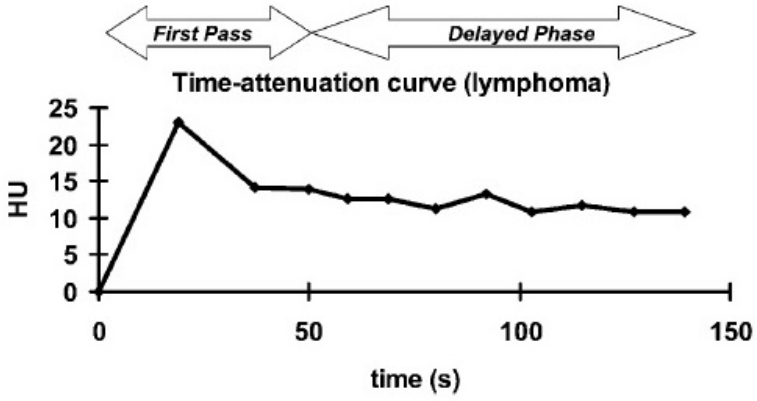

Figure 8: Time attenuation curve of a CT perfusion scan of a lymphoma [56]

Table 3: An overview of the CT perfusion parameters. EES = extravascular extracellular space

	Acronym for:	Interpretation	Unit
AF	Arterial flow	perfusion of whole blood per unit mass of tissue	$\frac{ml}{min*100ml}$
BV	Blood volume	within region of interest	$\frac{ml}{100ml}$
FE	Flow extraction product	estimate of K^{trans}	$\frac{ml}{min*100ml}$
K^{trans}	Transfer constant	between blood plasma and EES	$\frac{1}{min}$
K_{ep}	Rate constant	between EES and blood plasma	$\frac{1}{min}$
MTT	Mean Transit Time	between entering and leaving a compartment	
PS	Permeability surface area	product per mass of time	$\frac{ml}{min*g}$

3.2 Mathematical models

Different mathematical models and software are designed to estimate tracer kinetics in the human body. First, more simple models were used to describe DCE-MRI gadolinium kinetics until advances in imaging protocols and hardware have led to a higher quality of data. This introduced the application of more complicated models that were originally developed in physiology, and applied in nuclear medicine[57]. As these models have originally been used to image brain perfusion, these can not all be generalized to apply in oncology imaging: After intravenous injection of a contrast solution it is distributed over the vascular bed during which it has an intravascular distribution yet also extravascular leakage of contrast takes place. The amount of this leakage and the consecutive wash out depends on the permeability of the vessels which is different in tumours than in brain tissue. Cancerous tissues have immature capillary networks with distinct morphological and function characteristics formed by neoangiogenesis[53].

Models can estimate CT perfusion parameters on basis of the arterial contrast enhancement, a time attenuation curve known as the arterial input function (AIF). In CT this is linear with the concentration of contrast in the blood plasma of the feeding artery. During the curve of an AIF (see figure 8, where contrast enhancement in a lymphoma is tracked) there are two different phases; the initial or first phase is the the flow of contrast through the (micro)vasculature and typically comprises the first $45-60seconds$ p.i. After this first peak, the slope flattens ($1-2minutes$) and during the wash out phase up to 2 to $10min$ p.i., backflow of contrast into the intravascular space occurs[56]. Within 30-60 minutes the contrast is completely cleared from normal tissue. Between entering and leaving the tissue, a transit time of the blood can be indicated, furthermore the arterial flow (AF) and blood volume (BV) within a voxel can be calculated with the help of this AIF, as well as parameters representing the permeability which are described in table 3.

Mathematical models are developed based on different principles: Direct methods, methods using a non-linear regression, linearization models or deconvolution, additionally, a single or double compartment can be described[58, 59, 57]. A compartment is defined as a well-mixed space, diffusion of a tracer is very high and concentration differences are immediately levelled out[57]. The most used mathematical estimations of the blood perfusion are discussed below.

3.2.1 Direct methods

Fick principle The simplest method is a direct-measurement based on the Fick principle. The rate of influx of the contrast medium is the blood flow times the arterial concentration $C_a(t)$. The rate of efflux is the venous concentration $C_v(t)$ times the flow. The rate of accumulation $q(t)$ is the difference between influx and efflux rate of contrast. The accumulation $Q(t)$ only depends on the difference between the

total influx and efflux of contrast up to the imaging time point[60].

$$q(t) = \frac{dQ(t)}{dt} = AF[C_a(t) - C_v(t)] \tag{2}$$

$$Q(t) = AF[\int_0^t C_a(t)dt - \int_0^t C_v(t)dt] \tag{3}$$

When assuming no venous outflow occurs, the flow can be calculated by dividing the rate of accumulation by the arterial concentration.

$$AF = \frac{q(t)}{C_a(t)} \tag{4}$$

Maximum slope model The maximum slope model is based on this Fick principle. The accumulated contrast can be plotted over time within a voxel or region of interest (ROI) as is done in figure 9. When the assumption is made that in the first few seconds ($< 4 - 6s$) no venous outflow occurs, the maximal slope, or arterial flow (AF), can be calculated[54]. As the name suggests, it is the steepest slope of the time-attenuation-curve. This models assumes a single compartment where no exchange of contrast between extra- and intravascular space takes place. Typically, a contrast agent injection of at least $10ml/s$ is needed to make the assumption more reliable.

$$[\frac{dQ(t)}{dt}]_{max} = AF[C_a(t)]_{max} \tag{5}$$

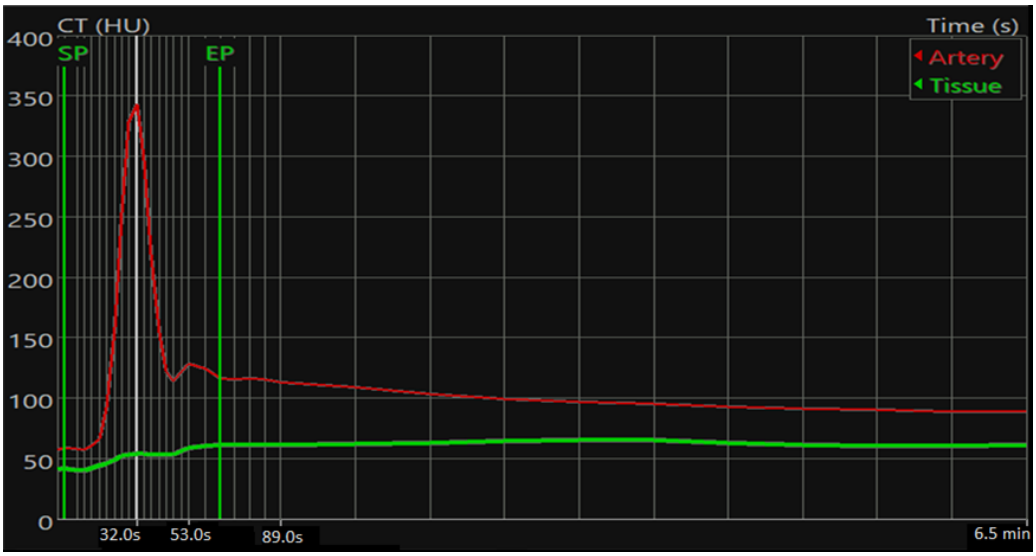

Figure 9: Tissue density curve of contralateral tongue (green) and arterial input function (AIF, red). The start point (SP) and end point (EP) indicate the range of the maximal slope.

3.2.2 Impulse response function

Other models use the AIF to describe the concentration within the tissue, a tissue density curve (TDC), with the help of a residual impulse response function (IRF) (see equation 6). The IRF is a theoretic curve and assumes that the concentration of contrast material is linearly dependent on the AIF when constant blood flow is retained. The Mean Transit Time (MTT), the mean time in which blood passes through the capillaries, is obtained by dividing BV by AF. This function cannot be measured directly and is therefore estimated by the tissue response tot the influx of contrast medium. The IRF can be

described by different perfusion models such as the Adiabatic Approximation to the Tissue Homogeneity model (AATH)[61], and the Tofts model (TM)[62]. Both models assume reversible leakage of tracer to the extravascular space.

$$TDC(t) = AIF(t) \circledast IRF(t) \tag{6}$$

$\circledast$ = convolution

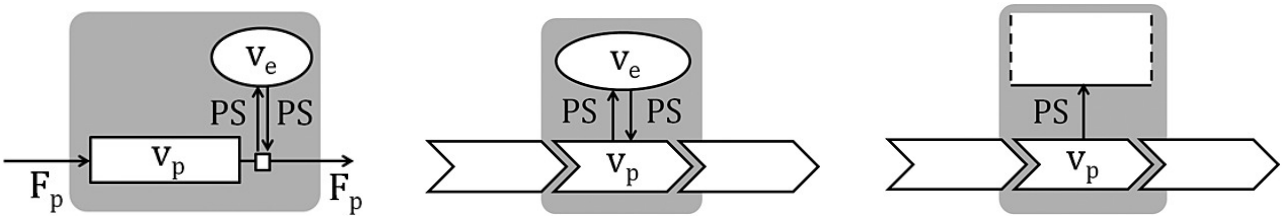

(a) AATH (b) ETM (c) Patlak

Figure 10: Representation of the adiabatic approximation to the tissue homogeneity model (AATH), extended tofts model (ETM) and Patlak model [57]

Non-linear regression AATH, shown in figure 10a, assumes that concentration of contrast in extravascular volume changes slowly relative to that in intravascular volume[58]. It models the blood plasma as a plug-flow system in which all particles move with constant velocity, as is the case in a single and structured capillary[57]. The interstitium is modeled as a compartment. A finite transit time exists for the passage of contrast from the artery to the vein, all particles have the same transit time and leakage is reversible [61]. AATH with with fixed transit time (AATHFT) is included because of the problems created by the transit time of AATH[63].

The TM assumes a highly perfused, high arterial flow, two-compartment model in with bidirectional transfer of contrast between intra- and extravascular space takes place. It is presumed that contrast is mixed instantaneously after arrival in the intravascular and interstitial space. The permeability of the extended tofts model (ETM) is identical, however the effect on mixing is delayed[62], as visualized in figure 10b. An other assumptions of this model is that contrast extravasation is low enough to ensure equal concentration in arteries and capillary beds[64].

Linearization The Patlak model is a simplified version of a compartment model, characterizing the perfusion into a linear regression problem. The Patlak model is a dual-compartment model and assumes, for a certain period of time, a unidirectional transfer of contrast from the arterial compartment (reversible) to the tissue (irreversible) as is visualized in figure 10c[65, 66]. A highly perfused tissue is assumed and it is modeled after the ETM, with negligible backflux from interstitium to the blood. A Patlak plot can be used to represent the data: A straight line with slope K^{trans} and intercept BV.

Deconvolution Deconvolution of the IRF is a frequently used method for brain perfusion; acquisition over only $60s$ is sufficient to estimate all parameters when the sample is very small[67]. The deconvolution can be calculated in several ways, for example by using the convolution theorem of the Fourier transform, yet this method is sensitive to noise[68]. More frequently, the singular value decomposition is applied; the convolution integrals are algebraic reformulated. Although this method has been validated in multiple studies, these were all studies to the perfusion aspects of the brain[54].

3.2.3 Which model to use for analysis of CT perfusion in oropharyngeal tumours

All mathematical models make assumptions in order to simplify the physiology within the human body. The Fick and maximum slope model assume no venous outflow. To make this assumption more reliable, a contrast injection with a rate of at least $10ml/s$ should be used, which cannot safely be achieved in clinical practice. Additionaly, even at increased rates, venous outflow does still occur[60]. The plug-flow system used by the AATH model can not be applied to oncology, as tumour vessels are generally tortuous making constant velocity of particles difficult if not impossible. The TM, ETM and Patlak model need a highly perfused tissue in order to correctly assess the perfusion parameters. This high perfusion is most likely correct in tumours although the Patlak model does not take into account reversible transfer between the intra- and extracellular compartment which in turn is likely incorrect due to the increased permeability of tumour vasculature. As for the deconvolution based calculations, contrast exchange between the intra- and extravascular compartment is likely to also takes place after the one minute of CT sampling in tumours, resulting in inadequate estimation of parameters.

Although much of these assumptions are not likely to adequately represent the tumour physiology, perfusion scans also have technical and resolution limitations. When the resolution of the CT scan is not sufficient, the parameters will also not be estimated satisfactorily. Additionally, the AIF is assumed to be sampled directly at the entrance of the tissue, yet is mostly measured more upstream. The actual AIF is both delayed and dispersed compared to the sampled AIF. Furthermore, in all models the lymphatic drainage is presumed to be immeasurably small, yet in physiological circumstances it is not[57].

Next to the mathematical basis of the models, the availability of software in the Radboudumc also plays a vital role. There are two different software modalities available for CT perfusion evaluation: Vitrea (Canon Medical Systems, Japan) and Olea sphere (Olea Medical, Paris, France). Vitrea has embedded a maximum slope and Patlak model for 4D Body Perfusion and the Olea sphere has an embedded Tofts model based calculation. Based on availability, the Vitrea software is used even though otherwise the Olea software would be preferable. The Patlak model does determine the vessel permeability which is assumed to be of importance in the tumour microenvironment we want to assess but the Tofts model can be used to also estimate the backflow of contrast from the tissue into the vascular compartment.

3.3 Scan protocol

3.3.1 CT acquisition settings

The choice for a protocol depends on the target organ, configuration of the CT scanner and clinical objective[58]. As previously explained, a CT perfusion protocol consists of a series of scans and therefore the radiation dose can become quite high. According to the ALARA principle, a good trade-off between image quality and radiation dose should be established.

A CT scanner has multiple settings and technical specifications; a cranio-caudal distance (pitch) within a specified gantry rotation time. The tube voltage (kV) influencing the average energy of the X-rays and peak kilovoltage (kVp), the peak maximum energy. These parameters are mostly identical in the modern systems due to a constant potential. The electrons can flow at a specific rate through the X-ray tube measured in milliamperes (mA) and in mA-seconds (mAs); the rate over time. Additional to these CT setting, the contrast solution used can have different concentrations and can be injected into the patient at different rates. A higher concentration will cause more attenuation. A good trade off between CT settings should be made: A low tube voltage results in excessive image noise while high voltage increases scatter. Furthermore, low voltage decreases radiation exposure and increases attenuation of iodine. By increasing the mAs, more photons of the set energy are produced resulting in increased resolution but also increased radiation.

In order to provide sufficient volume of a possible heterogenous tumour and sufficiently high time resolution, the CT scanner should be multi-slice and should have a minimum of $4cm$ cranio-caudal distance within $2s$ of gantry rotation time[69].

A tube voltage of $80 - 100kV$ is typically recommended for head or neck imaging and because these areas do not variate much with increasing patient body size, this can be applied for all patients[69, 70]. A voltage of $120kVp$ is previously used in a study to image tumour invasion of the laryngeal cartilage[71], although when researching mandibular invasion of tumour[72] and in a review of imaging with CT perfusion in HNSCC, $80kV$ is recommended based on iodine attenuation and the contrast-to-noise ratio[55]. Furthermore, an increased radiation exposure of 2.8 times is estimated when using $80kV$ in stead of 120[55].

The tube current must be set as low as possible to minimize radiation exposure while maintaining good resolution, though no clear consensus can be found in literature. Dankbaar et al.[71] use $200mAs$, whereas Oei et al.[72] use $100mAs$. In the review of HNSCC by Faggioni et al.[55], low values ranging between $60 - 120mAs$ are described and it is argued that with the addition of angular and z-axis tube current modulation within $20-100mA$ good resolution is possible when compensated by the high contrast-to-noise resulting from $80kV$ and high iodine delivery rate.

The injected agent, iodine, should have a concentration of at least $300mg/ml$ when injecting $40 - 60ml$ at a rate of more than $4ml/s$, resulting in a total dose of $12 - 18g$[69]. Higher rates may be advantageous but will cause a higher pressure when injected; which the infuse system and the patients veins might not be able to handle. Dankbaar et al.[71] used Ultravist 300 ($300mg\ iodine/ml$) $5ml/s$ with a total dose of $50ml$, Oei et al.[72] inject Ultravist 300 $50ml$ at $5ml/s$ and Faggioni et al.[55] recommendd $40ml$ of iodine with a concentration of $320mg/ml$ at a rate of $5ml/s$. It is established that a higher concentration enhances contrast enhancement, but also beam hardening artefacts adjacent to large vessels[69, 55]. A saline flush of $40ml$ should be subsequently administered at $5ml/s$.

Conclusion To accomplish the optimal settings and keep radiation dose as low as possible, the most advanced CT scanner is used; Canon Aquillion one [not yet on the market, therefore type cannot be specified] (Canon Medical Systems, Japan). A rotation time of $0.5s$ is accomplished for a cranio-caudal range of $8cm$. The tube voltage is set to $80kV$ and tube current to $100mA$ for the first 24 volumes and $150mA$ for the last 10 resulting in $50mAs$ and $75mAs$, respectively. Iomeron 300 is injected at a rate of $5ml/s$ and total dose of $60ml$ followed by a $40ml$ saline flush at the same rate.

3.3.2 Time resolution

As is visualized in figure 8, two phases of attenuation occur after injection of contrast and different imaging frequencies are needed to optimally sample these periods as described by Miles et al.[56]. The time it takes for contrast to reach the carotid artery can vary between patients, therefore a test bolus is injected to calculate the time at which the first perfusion scan should take place. The frequency of the first series, until $45 - 60s$ p.i., should be every $1s$ for deconvolution analysis, and $3 - 5s$ for protocols using single- or double compartment models[27, 52]. The first part of the interstitial phase, until $2min$ p.i., is when the return of contrast material from the extra- into the intravascular space is significant and a $6s$ interval is recommended[71]. The period between $2 - 10min$ p.i. is required to measure vascular permeability and as changes in attenuation are less rapid, a lower frequency of imaging is needed of about $10 - 20s$[56, 52].

Conclusion We use and interval of $3s$ for the duration of 16 scans to make sure we image the first minute after injection in every patient. The interstitial phase is imaged with 6 at a $6s$ interval followed by 10 scans with a time resolution of $30s$. The $30s$ interval in stead of $20s$ will result in imaging up to $6.5min$ p.i. while maintaining a lower radiation dose.

3.4 Motion Correction

In previous research, the most difficulties arose when alignmening of the images. CT perfusion protocols image the same region over a longer time, during which head movement is not uncommon. Even though there is no beating heart or diaphragm in the field of view, physiological processes like swallowing or breathing can also cause deformation of the region of interest. When deformation of the region of interest takes place during scanning, it is imaginable that the calculated parameters are not reflecting the physiological behaviour of the tissue correctly. This might be one of the reasons why the values indicated in literature still include high standard deviations and are not comparable. Accurate estimation of tumour parameters cannot be obtained without accurate motion correction and patient instruction.

3.5 Feasibility

3.5.1 Logistics

For radiotherapy, it is also very important to immobilize the patient so that the treatment is delivered to the accurate region every time, during 34 sessions. Therefore, a thermoplastic mask is made which can be clicked on to the table of the radiotherapy apparatus. To select the correct region for treatment, a radiotherapy plan CT scan of the tumour is made, also while the patient is wearing this mask. For more accurate radiotherapy planning, FDG PET/CT or MRI images provide additional information about the tumour spreading and lymph node metastases. Therefore, customized boards for these MRI, PET/CT and radiotherapy CT scanners are present in the Radboudumc to scan the patient while wearing the mask. Such an immobilization method could be ideal to minimize the motion during the CT perfusion. However, the CT scanner embedded in the PET/CT is not advanced enough for the CT perfusion protocol and there is no radiotherapy board fitted to the CT scanner that can be used. However, it might be possible to stabilize the board of the PET/CT on the CT scanner with some additions.

In this CT scanner, multiple headrests can be used; the click mechanism designed for the different head rests (shown in the appendix in figure A2) can be used to immobilize the radiotherapy-planning board of the PET/CT scanner on the CT. Therefore, a 3D model is segmented and printed, after some adjustments and an additional stabilizing band, the board is accurately immobilized by inserting the 3D print into the slot for the headrest, as is visualized in figure 12.

(a) Front view (b) Back view (c) Front view (d) Back view

Figure 11: The different views of the 3D printed model. (a&b) are images of the segmentation done with the help of 3D slicer. (c&d) are pictures of the 3D printed model

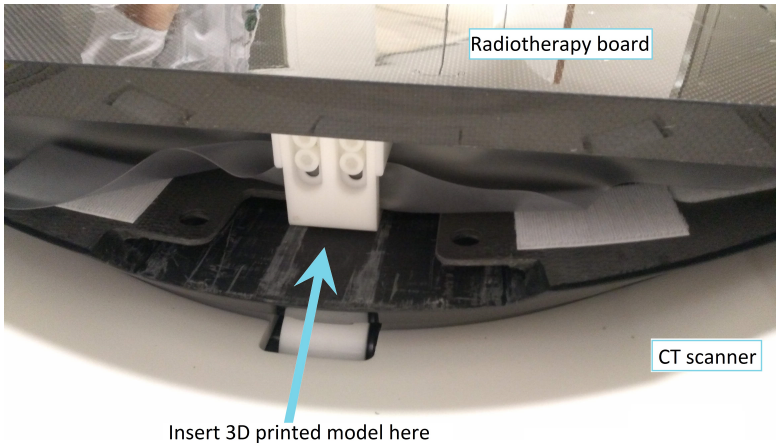

Figure 12: The insertion place of the 3D model within the CT scan

3.5.2 Phantom tests

A second question is whether the use of the radiotherapy board also provides images that can be accurately registered to the PET/CT scan and the radiotherapy planning. Therefore, a small test was done with a head phantom, as can be seen in figure 13. A customized thermoplastic mask was made for this phantom and CT scans were made on the PET/CT and CT scanner. During a series of test scans on these scanners, the phantom was displaced and the mask adjusted to simulate the movement between different scans on one scanner. When aligning all scans with the Mirada software (Mirada Medical, Oxford, United Kingdom), rotation matrices could be extracted. The rotation matrix to align one scan made on CT (CT_{CT}) to the CT made on the PET scanner $CT_{PET,1}$; $M_{CT,PET}$ and the rotation matrix to align another CT scan made on the PET scanner after repositioning the phantom and mask $CT_{PET,2}$ to $CT_{PET,1}$; $M_{PET,PET}$.

$$Rotationmatrix = \begin{bmatrix} R_{11} & R_{21} & R_{31} & 0 \\ R_{12} & R_{22} & R_{32} & 0 \\ R_{13} & R_{23} & R_{33} & 0 \\ T_x & T_y & T_z & 1 \end{bmatrix}$$

$$M_{CT,PET} = \begin{bmatrix} 0.9996 & 0.0256 & -0.0146 & 0 \\ -0.0254 & 0.9996 & 0.0128 & 0 \\ 0.0149 & -0.0124 & 0.9998 & 0 \\ -17.5677 & 234.2246 & -1977.0570 & 1 \end{bmatrix}$$

$$M_{PET,PET} = \begin{bmatrix} 0.99 & 0.0111 & 0.0042 & 0 \\ -0.0113 & 0.9992 & 0.0392 & 0 \\ -0.0037 & -0.0392 & 0.992 & 0 \\ -1.1753 & 33.3756 & 9.3467 & 1 \end{bmatrix}$$

The translation is clearly larger for the alignment of the CT_{CT} to the $CT_{PET,1}$ scan, this is however an alignment that is easily made and the scandata is not influenced by only translating the scan. The rotation of a scan can be more predictive for when image warping is needed to correctly align scans.

The calculated Euler angles in degrees for $M_{CT,PET}$ are: $\alpha = 1.47 \quad \beta = 0.83 \quad \gamma = 0.73$ The calculated Euler angles in degrees for $M_{PET,PET}$ are: $\alpha = 0.64 \quad \beta = -0.24 \quad \gamma = 2.25$

The rotation of α and β are larger when the CT_{CT} was aligned with the $CT_{PET,1}$ by a factor 2.3 and a factor 3.5. The γ rotation was a factor 3.1 more when the $CT_{PET,2}$ was aligned with $CT_{PET,1}$ compared to repositioning the phantom one the same scanner. It can be concluded that the scans made on CT and PET/CT can be aligned; because after repositioning the phantom and mask, a larger angle was observed than when aligning CT_{CT} and $CT_{PET,1}$.

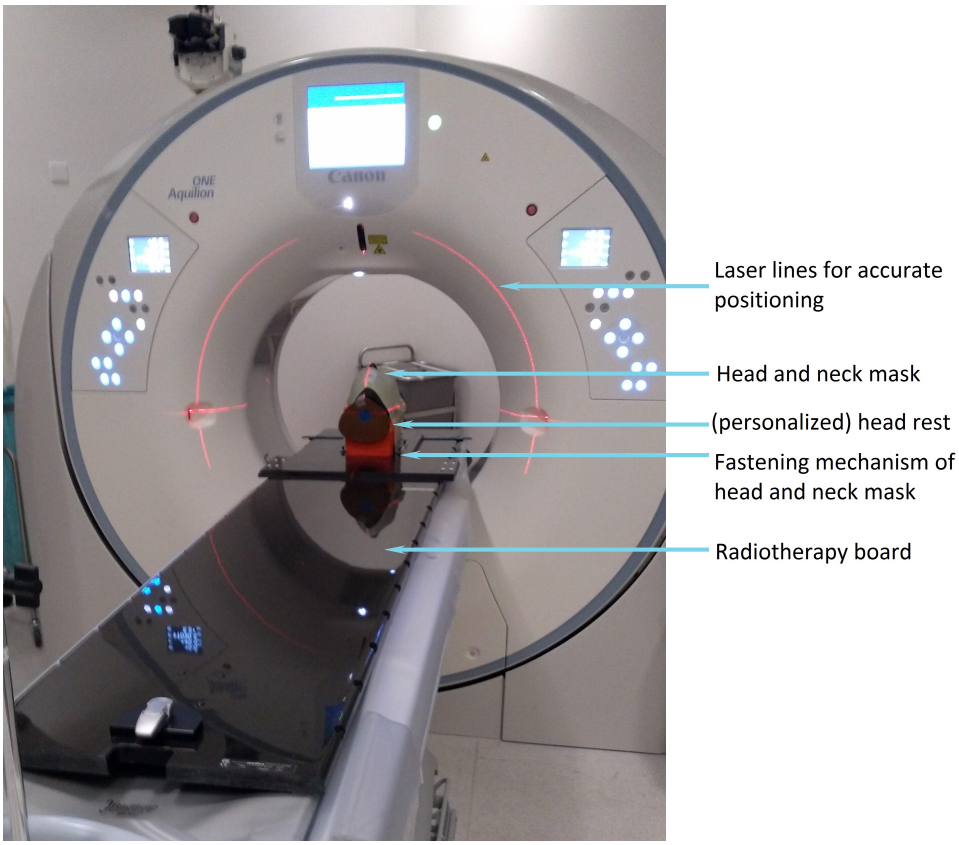

Figure 13: The phantom test scan in which the different attributes are noted

3.5.3 Test scan on a patient

With this phantom test we could not conclude if the newly developed CT perfusion protocol had a sufficient flow rate, accurate timing after injection and whether sufficient image resolution was obtained to perform analysis. Therefore, after this phantom scan, the scan protocol was tested on a patient. This patient had to meet certain criteria; CKD-EPI > 60 (Chronic Kidney Disease Epidemiology Collaboration), no previously known contrast allergies, malignancy of the head and neck with a diameter $> 1cm$ and planned for a contrast enhanced CT scan as part of diagnostic work-up. These criteria were set so that the patient did not only receive contrast for the test but also for diagnostic purposes, possible contrast reactions would therefore not only be related to the test. Because of the extra contrast administered, a good kidney clearance is necessary. Additionally, the tumour needs to be clearly visible on the scan, therefore the minimal diameter of $1cm$ was set. Finally, the patient should give consent for the extra scan.

From this test it was concluded that the protocol needs blank scans to calculate the increased HU on the scans p.i. Therefore, we added two mask scans at 0 and $3s$ after injection, before the contrast

arrives in the head and neck region, to the protocol described in section 3.3.2. Secondly, the scans were loaded into the Vitrea software to check if the resolution was appropriate. The software could calculate a BV, BF and FE map, so therefore it was concluded that the accuracy of the mA and kV was sufficient.

3.6 Conclusion

To conclude, the settings of the CT scanner that will be used for CT perfusion imaging of patients included in the clinical study with oropharynx tumours are located within table 4. A test bolus of $15ml$ of Iomeron is injected at $5ml/s$ to determine the time at which the contrast arrives in the carotid artery. This time point minus $1s$ is the start time of the first pass series.

Table 4: CT scan settings for perfusion imaging of oropharyngeal tumours

	Preset	Setting
CT scanner	Canon Aquillion one	[not yet on the market]
Contrast agent	Iomeron 300	$5ml/s$, total $60ml$
Saline flush	NaCl 0.9%	$5ml/s$, total $40ml$
Mask scans	scan at $0s$ and $3s$ p.i.	$80kV$, $100mA$
First pass	16 scans $*$ $3s$ interval	$80kV$, $100mA$
Interstitial phase	6 scans $*$ $6s$ interval	$80kV$, $100mA$
Permeability imaging	10 scans $*$ $30s$ interval	$80kV$, $150mA$
Total imaging time	$\pm 6.5min$	
Rotation time	$0.5s$	
Cranio-caudal range	$8cm$	
Slice thickness	$0.5mm$	
DLP	479.4	$6.7mSv$

4

The PIVOT study: Study design and first results

^{68}Ga-RGD$_2$ PET/CT and CT perfusion imaging provide an opportunity to non-invasively assess the angiogenesis aspects of the tumour microenvironement in HNSCC. It is hypothesized that early changes in this tumour microenvironment are related to the increase in response to therapy in HPV induced oropharyngeal carcinomas. Therefore, it is proposed to image patients with HPV$^+$ and HPV$^-$ OPSCC before and during chemoradiation and correlate the findings to the local control within one year of follow-up.

4.1 Introduction

Patients presenting with squamous cell carcinomas arising from the oropharynx have one of the worst 5-year survival rates of all HNSCC patients. In 2018, 521 patients presented with head and neck malignancy in the Radboudumc, from which 28 arose from the oropharynx. In this subsite, not only the classical risk factors of extensive alcohol and tobacco intake are involved in tumourigenesis, but also the HPV virus. Notable is the increasing incidence of the virus related tumours as well as the substantially increased 8-year survival; 70.9% versus 30.2%[73]. In OPSCC the preferred option is radiotherapy treatment with addition of concomitant chemotherapy once a week in vital patients with large lymph node metastases. Despite current advancements like determining the HPV status of a tumour and an accelerated radiotherapy scheme of 5,5 weeks, a large number of recurrent diseases occur while treatments still cause high morbidity. Most treatment decisions are currently based on clinical presentation of the patient resulted from limited knowledge of differences in underlying tumour biology.

4.1.1 Multimodal imaging

Several studies are currently focusing on identifying the most optimal biomarker of the tumour microenvironment to research tumour characteristics, improve diagnosis and identify options in therapy monitoring as discussed in previous chapters. We believe imaging with the help of RGD radiolabelled with Gallium-68 provides such an opportunity and will help us better understand the differences in microenvironment between HPV$^+$ and HPV$^-$ OPSCC. By binding to integrin $\alpha_v\beta_3$ on active endothelial cells, the angiogenesis activity of the tumour can be mapped. This however does not provide us with information on how the tumour is perfused, whereas CT perfusion imaging does. The hypothesis is that, next to the initial differences in microenvironment, HPV related tumours react differently to treatment which can possibly be explained by a different response during the early phase of treatment.

To test this hypothesis, both RGD PET/CT and CT perfusion are performed before and in the second week of chemoradiation treatment. The RGD and CT perfusion scan parameters are discussed in chapter 2 and 3 respectively. In experiments with SPECT imaging of ^{111}In-labeled RGD in FaDu xenografts (human pharynx squamous cell carcinoma), uptake within the tumour already decreased 1 day after a single irradiation but was enhanced 10 days after[74]. This could indicate that the tracer can help detect early effects of the treatment. To exclude effects of the radiosensitizing chemotherapy, imaging should not occur within 24 hours after administration of the chemotherapy whereas the imaging should take place between the same two fraction of chemo. Additionally, differences during early phases of treatment can help steer timely treatment decisions in the future. To correlate the characteristics of the tumour microenvironment to response, local control and the end of therapy and during one year follow-up is recorded.

To further investigate the tumour microenvironment and how this can be characterized with the help of multimodal imaging, FDG PET/CT and MRI scans of the patient are correlated to the RGD and CT perfusion. MRI scans are made during the diagnostic workup for tumour delineation and identification of possible malignant lymph nodes. CT or FDG PET/CT scans are made for radiotherapy planning while the patients is wearing a custom made head and neck mask. It has been concluded previously that while FDG PET/CT is superior for tumour staging, RGD PET/CT can provide complementary information for planning and response evaluation[75]. Additionally, FDG PET/CT has a significantly higher sensitivity for identification of nodal metastasis than CT or MRI[76].

Radiation ethics A CT perfusion scan protocol consists of multiple CT scans of the same volume and can therefore provide a significant dose in patients. As described in Chapter 3 this can be minimized by lowering the tube current and voltage and increase the time interval between scans. The estimated dose for one CT perfusion scan is $6.7mSv$, according to the mSv/DLP conversion described in ICRP 102 and the DLP estimated by the scanner. This dose is comparable to 2.5times that of a routine head CT and less than a CT thorax: The median effective radiation of one head CT is $2.1mSv$, and $8.0mSv$ of a thorax CT[77]. One RGD PET including low-dose CT of the head and neck region is estimated to be $5.7mSv$, on basis of dosimetry done by Lopez et al.[78]. The total dose of a patient participating in the study will be $27mSv$ when a diagnostic CT of the head is added to the follow-up CT perfusion scan. This dose can be multiplied by a relative detriment factor defined in ICRP 62, which is 1 for patients between 18 and 50 years old and $1/5 - 1/10$ for patients older than 50. Patients older than 18 years are allowed to participate in the study, we can not predict if every subject is 50 years or older, so therefore the estimated relative effective dose is $27mSV$. According to radiation ethics, an added dose over $20mSv$ should have a high level of benefit: 'Acquisition of knowledge, directly aimed at saving lives or mitigation of serious diseases'. However, the radiotherapy treatment plan of the subjects participating in the study will include a tumour dose of $68Gy$ and this field is mostly expanded to encompass the suspected lymph nodes. Therefore, we concluded that the additional radiation dose is negligible in these patients.

4.1.2 Inclusion and exclusion criteria

The patients that are allowed to participate in this study should have a histologically proven squamous cell carcinoma arising from the oropharynx and are scheduled for chemoradiotherapy in a curative setting. P16 immunohistochemical analysis should take place to determine the HPV status of the tumour. As explained previously, p16 can act as a surrogate marker for HPV status but could also predict treatment independent of HPV status. Nonetheless polymerase chain reaction (PCR) still remains the gold standard and is preferably done to correlate to the p16. Furthermore, the lesion diameter should be at least $1.0cm$ concluded from CT, MRI or FDG PET/CT within 4 week prior to intake, for accurate PET detection. To take part in the clinical trial, the patients should be at least 18 years old and are able to provide written informed consent. Under-aged or mentally impaired patients can only participate in clinical trials when the research question cannot be sufficiently researched without these patient groups which is not the case in this study.

Exclusion criteria are based on contra-indications for PET and contrast enhanced CT. Pregnant or breast feeding woman should receive as little radiation as possible and can therefore not participate, as well as patients suffering from serious claustrophobia. Unnecessary suffering can be caused by lying in the PET scanner two additional times for 20 minutes as well as a high risk on dropping out of the study due to anxiety. Iodine-containing contrast agent can lead to kidney problems or can cause problems in patients with pre-existing kidney disease; contrast induced nephropathy and nephrogenic systemic fibrosis are two rare but serious disorders associated with CT contrast. To reduce the risk on obtaining one of these disorders, patients should have a creatinine clearance of at lest $30ml/min/1.73m^2$ according to the CKD-EPI formula (chronic kidney disease epidemiology collaboration) and should be able to discontinue NSAIDs (non-steroidal anti-inflammatory drugs) 24 hours before the CT perfusion scan and diuretics for 48 hours. Furthermore, no severe iodine-contrast related allergic reaction should have taken place in the

past and the patients should not suffer from multiple myeloma or Waldenströms macroglobulinemia with light chains in the urine. Finally, the patient should not have been irradiated before in the area of the tumour because this could have caused a whole different tumour microenvironment.

4.1.3 Imaging data

In this study, much data is acquired from a patient and state-of-the-art techniques are used to image the tumour microenvironment. To ensure this data can be used even when new insights in reconstruction methods are used, all raw PET and CT data is saved on the servers. Furthermore, this study is monitored by a trained monitor of the Radboud Technology Center Clinical Studies to make sure the study including all files and data are according to the guidelines.

4.1.4 Research question

What are the differences in tumour microenvironment between HPV^+ and HPV^- oropharyngeal squamous cell carcinomas treated with chemoradiotherapy assessed with the help of RGD PET/CT and CT perfusion?

4.2 Method and materials

4.2.1 Study population

Patients with a histologically proven OPSCC who are primary treated with chemoradiotherapy were asked to participate in the clinical study when the inclusion and exclusion criteria were met. The research proposal was approved by the Radboudumc medical ethical committee and when patients agreed to participate, the informed consent procedure was started. The one patient included at this time of writing had a diagnostic MRI from which the tumour volume was determined. The tumour type and p16 status were obtained from the biopsies performed at the tumour location with flexible endoscopy and from fine needle aspiration cytology of possible pathological lymph nodes. The patient was discussed at the weekly multidisciplinary board meeting and scheduled for radiotherapy with concomitant chemotherapy. The patient was recruited during the intake consult at the radiotherapy department. 24 hours after the patient had been given information about the study, the patient was contacted again to perform an informed consent procedure.

4.2.2 Treatment

For the radiation treatment, a thermoplastic head-and-neck mask was custom-made per patient and used to immobilize the patient during treatment and during the scans used to plan the treatment. For the first patient, an MRI (multiple t1 and t2-weighed series, with and without gadolinium-based contrast, FOV from caudal cerebrum until cranial glottis) and FDG PET/CT scan (158 PET slices of $3mm$, low-dose CT 316 slices of $1.5mm$) including diagnostic CT (964 slices of $0.5m$) were made for radiotherapy planning to more accurately determine tumour and lymph node regions.

The radiation treatment regime consisted of an estimated dose of $68Gy$, divided into 34 fractions, 6 fractions a week on the tumour and ipsilateral neck lymph node levels. The contralateral neck received an elective dose of $50.3Gy$. Before the first fraction and hereafter once every week for 6 weeks, a dose of $40mg/m^2$ cisplatin was administered to the subject as radiosensitizer.

4.2.3 Follow-up

After the last fraction radiotherapy and hereafter every 3 months the subject will be seen by the radiotherapist or Ear-Nose and Throat (ENT) physician. During these follow-up visits, clinical examination of

the neck, inspection of the previous tumour site and flexible endoscopy will be performed. When possible clues for a residue or recurrence are recognized, an MRI or CT scan will be ordered and biopsies will be taken.

This preliminary report was written when no subject has had their first follow-up. Although important for the relevance of scan values, these aspects are not discussed further in this thesis.

4.2.4 Imaging protocol

The RGD PET/CT and CT perfusion scan were made before the commencement of treatment and the follow-up scans were made between the second and third fraction of chemotherapy. To better align the scans and to prevent motion artefacts, the subject was scanned while in radiotherapy head and neck mask.

For the RGD PET/CT scan, 213.6 ± 8.1 MBq of [^{68}Ga]Ga-DOTA-$(RGD)_2$ was injected into the subject. Hereafter, a topogram and low dose CT scan (148 slices of $1.5mm$) were made. From 10 to 20 minutes post injection of the tracer, PET images in list mode were acquired (74 slices of $3mm$). In list mode, only one bedposition with a FOV of $16cm$ can be accurately evaluated with PET.

The CT perfusion images were made with the help of the scan sequence and settings discussed in section 3.6 encompassing a volume of $8cm$. After the follow-up CT perfusion, a diagnostic, contrast-enhanced CT (1127 axial slices of $0.5mm$) was made for more accurate delineation and comparison of the regions of interest.

4.2.5 Image analysis

Image analysis of one subject was done, therefore all important structures were delineated. These regions of interest included the tumour and the lymph nodes that the radiologist labeled malignant on the diagnostic MRI. Lymph nodes labeled malignant on the MRI did not have a fatty hilus, had central necrosis or were too big (larger than $1cm$ in diameter). Additionally, one lymph node on the left side that was labeled benign was also delineated, as well as a benign tooth abscess, the parotid and submandibular gland, the thyroid and the sternocleidomastoid muscle. These reference structures were all delineated on the ipsilateral side of the tumour except for the thyroid glad because of an FDG-avid focus in the ipsilateral side. For the CT perfusion, the carotid artery and the semispinalis capitis muscle were also delineated for reference. On basis of the MRI, the radiologist mentioned if lymph nodes were necrotic.

PET In the Oasis software (Segami, Columbia, United States of America) the FDG PET with diagnostic CT was analysed as well as the RGD PET scans of the baseline and follow-up. First, the SUV_{max} values of the RGD scans of 10 to $15min$ p.i. were compared to the RGD scans of 15 to $20min$ p.i. Hereafter, the most adequate time frame was used to compare SUV_{max} and SUV_{mean} values of the FDG and RGD baseline scan and the RGD baseline scan to the follow-up RGD scan. For the volumes of interest, a VOI was drawn to encompass the structure, except for the carotid and the muscle tissue where only a part of the tissue was delineated. This VOI was adjusted for all three PET scans to more accurately represent these tissues. Additionally, the total lesion glycolysis (TLG) of the tumour was determined by multiplying the SUV_{mean} and the volume (ml).

CT perfusion In the Vitrea software, the 4D body perfusion protocol was used to analyse the scans. For the arterial input an ROI within the ipsilateral carotid artery was drawn, and for the tissue reference, an ellipsoid was drawn in the contralateral tongue. On basis of these parameters, the Patlak plot can be opened. The first time point was chosen where the contrast enters into the extravascular space, the time point when the contrast reabsorbs to the intravascular space was also set. The program estimates a Patlak flow line on basis of these two points. On basis of the Patlak plot, the program computes the arterial flow (AF), flow extraction product (FE) and the equivalent blood volume (BV) for each voxel. A 2D region of interest was drawn in all structures mentioned above with the help of an ellipsoid.

4.2.6 Statistical analyses

No statistical analysis could be done when reviewing one subject, however the method to be used when more subjects are included is described.

The primary endpoint of the study is to find effects between HPV^+ and HPV^- tumours, leading to two groups to compare. A two sided test should be done when comparing the two means of the groups. The hypotheses are $H_0 : \mu_A = \mu_B$ and $H_1 : \mu_A \neq \mu_B$. n represents the sample size of one group, $n = 10$. The sampling ratio between the two groups ($k = n_A/n_B$) is one.

In a previous studies with this tracer, ($n = 10$), SUV_{max} tumour uptake was 7.5 ± 2.6. These represent the mean of group A and standard deviation. The sample size n is set to 10. When checking what the mean of group B should be to accomplish a power of 0.8, a μ_B of 4.25 is calculated. Considering a more likely mean of group B, for example 5.5, a sample size of 27 per group is needed.[79]

4.3 Results

The tumour in this case study was classified on basis of MRI (figure 14) as T2N1M0, p16 positive and HPV PCR positive, with tumour volume as listed in figure 19 and malignant lymph nodes in ipsilateral levels 1b, 2, 4 and retropharyngeal. On basis of MRI characterization, a radiologist labeled if lymph nodes had central necrosis, listed in figure 19. All malignant and benign structures delineated on the different scans are annotated on MR images in the appendix figures A3 & A4.

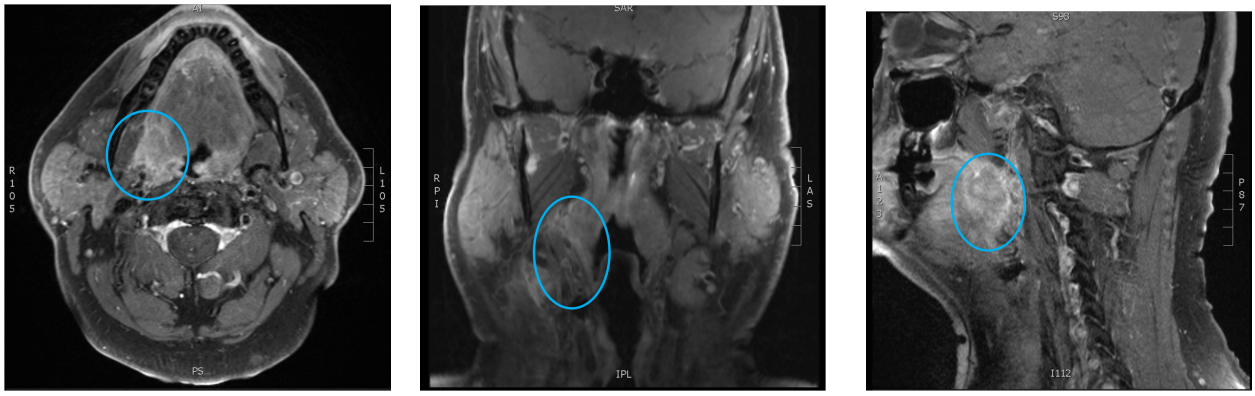

(a) axial (b) coronal (c) sagittal

Figure 14: The tumour in the right tonsil loge in three different views on MRI, T1 weighted, contrast enhanced, turbo spin echo sequence

RGD time frame The SUV_{mean} and SUV_{max} values for the time frame from $10 - 15min$ p.i. and the time frame from $15 - 20min$ p.i. of the RGD scan were evaluated. The highest tumour uptake was seen in the time frame 15 to $20min$ p.i. (for the follow-up 10.2 vs. 11.3) time frame as well as lower thyroid uptake (9.4 vs. 8.4 for both scans). Considering the thyroid has the highest background uptake in this patient, the second time frame, with lower thyroid SUV, was used for further analysis.

FDG compared to baseline RGD Uptake of FDG and RGD in the tumour is visualized in PET/CT images in figure 15 and A7, the SUV_{mean} and SUV_{max} values are plotted in graph 19. Total lesion glycolysis of the tumour was $117.5g$. FDG and RGD values correspond relatively good in non-necrotic nodes and benign tissue but not in the tumour and the retropharyngeal non-necrotic node.

RGD baseline compared to follow-up Overall, the SUV_{mean} and SUV_{max} of the tumour and the necrotic lymph nodes were increased in the follow-up scan. The RGD uptake in the parotid gland increased slightly compared to the more notable increase in uptake in the submandibular gland.

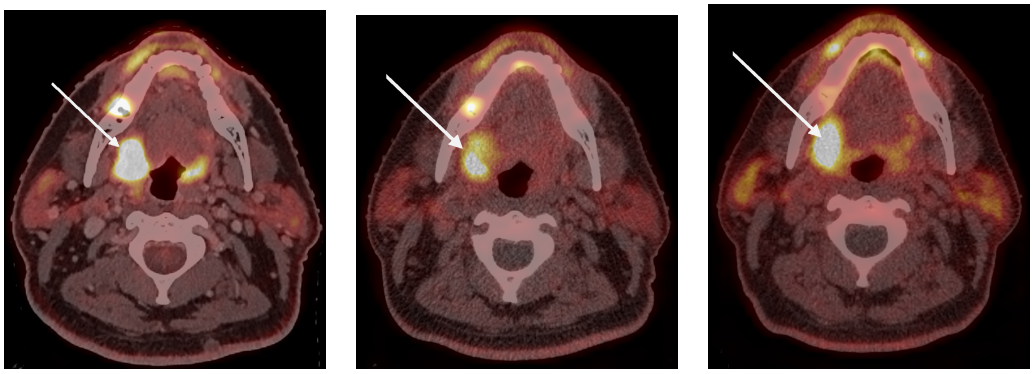

(a) FDG PET/CT (b) Baseline RGD PET/CT (c) Follow-up RGD PET/CT

Figure 15: The tumour in the right tonsil loge on the three different PET/CTs

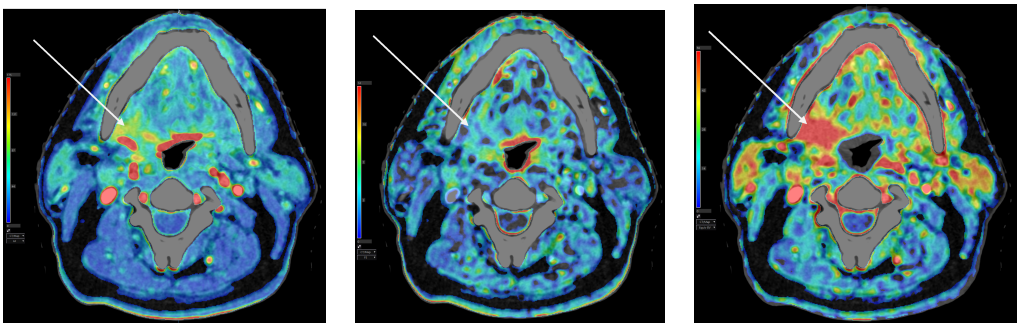

(a) AF map (b) FE map (c) BV map

Figure 16: The tumour in the right tonsil loge on the three different CT perfusion maps of the baseline scan.

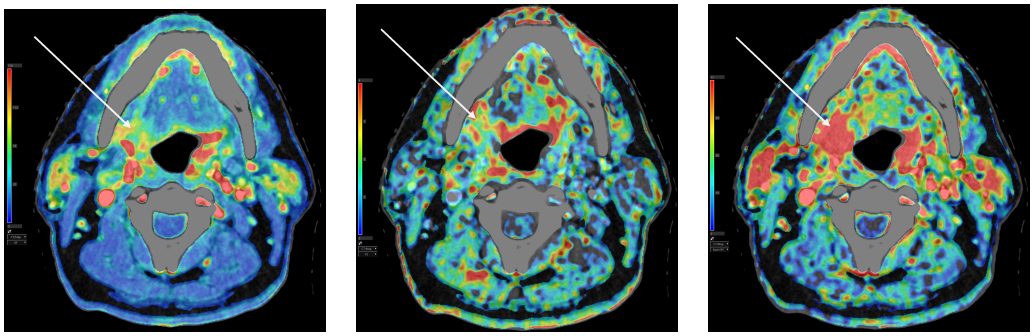

(a) AF map (b) FE map (c) BV map

Figure 17: The tumour in the right tonsil loge on the three different CT perfusion maps of the follow-up scan.

CT perfusion In figure 18, the analysis results of the different structures delineated on the CT perfusion scan are visualized. The field of view of the baseline scan was different than that of the follow-up scan.

In the baseline scan, two lymph nodes in level 2 were not in the field of view and in both scans, lymph nodes located in level 4 were not in the field of view. Visual inspection of the images concluded that the AF in tumour in the follow-up images was more heterogeneous. The distribution area of high BV values in the tumour region was larger in the follow-up scan as in the baseline scan as can be visually concluded from figures 16 and 17.

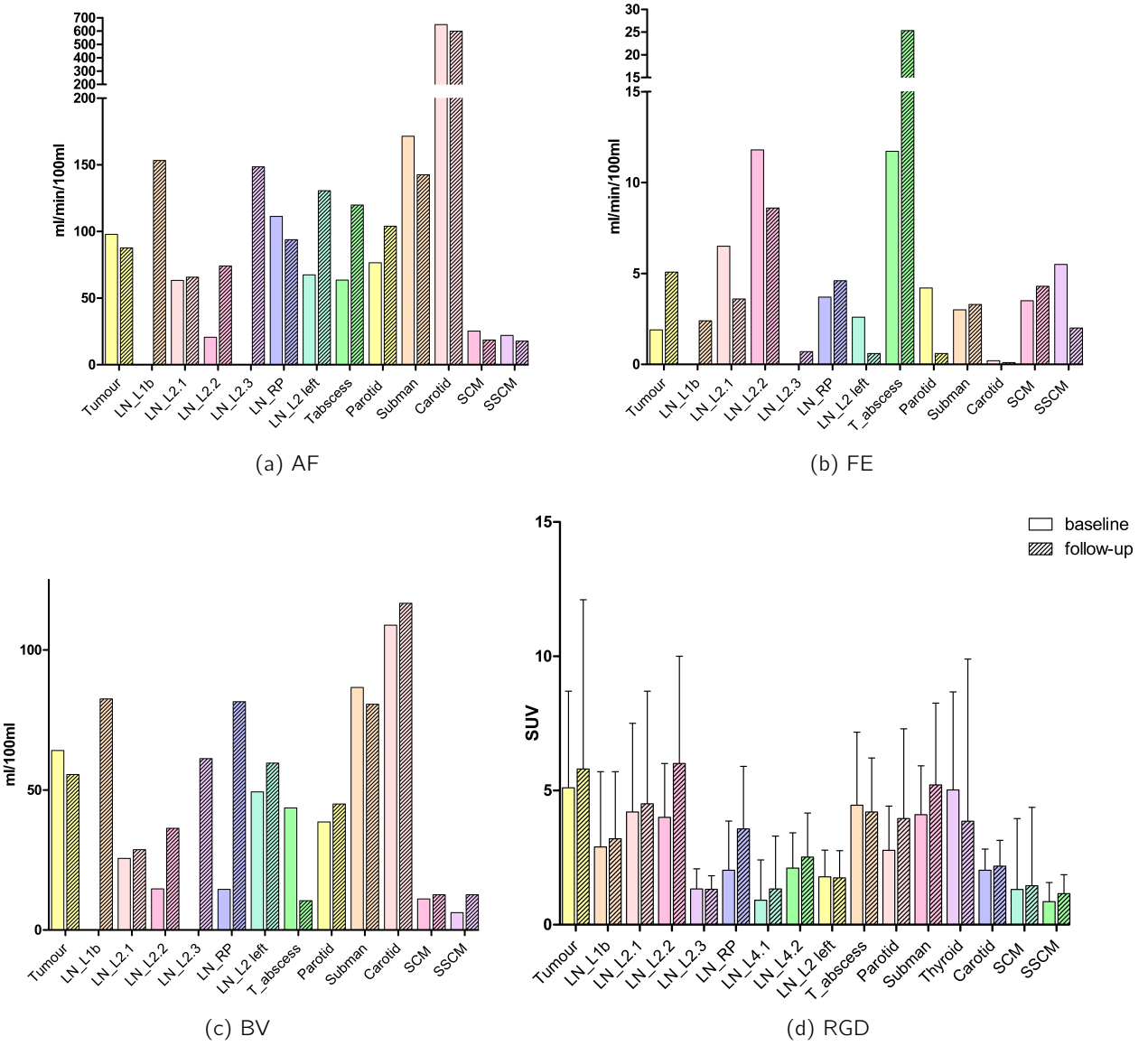

(a) AF

(b) FE

(c) BV

(d) RGD

Figure 18: CT perfusion and RGD PET analysis results. The paired columns represent the measurements from the base line and follow-up, respectively. LN = lymph node, L2 = lymph node level 2, RP = retropharyngeal, ipsi = ipsilateral, subman = submandibular gland, SCM = sternocleidomastoideus muscle, SSCM = semispinalis capitis muscle

4.4 Conclusion

Concluding from these results, it is feasible to assess the tumour microenvironment with RGD PET/CT and CT perfusion in OPSCC.

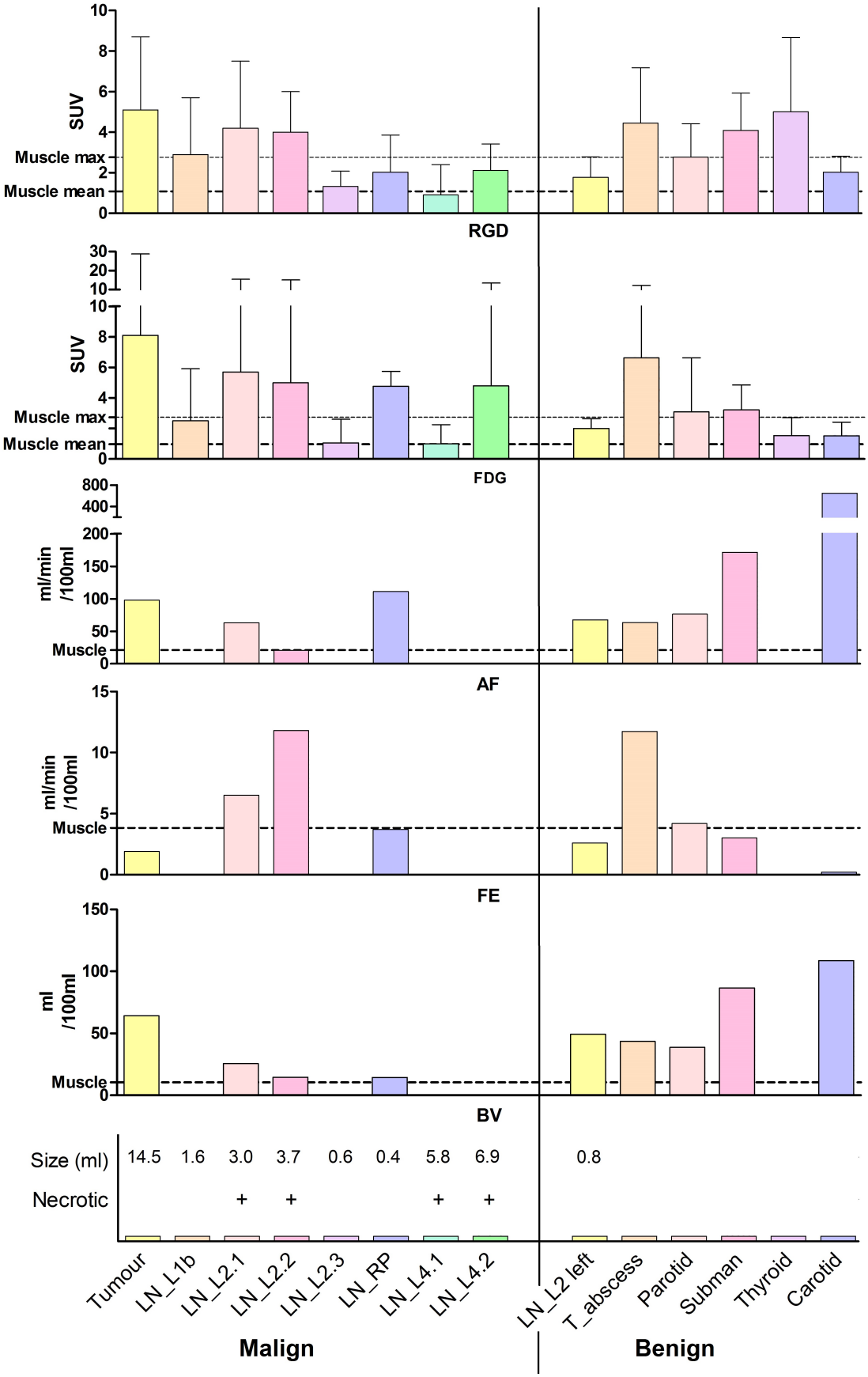

Figure 19: Baseline scan characteristics vs. mean of the muscular background. LN = lymph node, L = lymph node level, T_abscess = tooth abscess, subman = submandibular gland

5
General discussion

It is interesting to compare multiple imaging methods to look at the different aspects of the tumour. The golden standard of determining the TNM status of a tumour remains immunohistochemistry. However, it is imaginable that when cytology of a necrotic lymph node, like the ones in level 4 of the case study, is collected, no tumour material would be obtained whereas on imaging the lymph node is clearly malignant due to its size and necrotic area. It would be interesting if multimodality imaging does provide more certainty in identifying malignancies to prevent repetitive uncomfortable examinations leading to inconclusive histology reports. Moreover, on basis of cytology, no extranodal invasion can be diagnosed, whereas with imaging, central node necrosis could be identified. This necrosis and higher SUV_{max} has been shown to correlated strongly with extracapsular spread of tumour which, in turn, is a negative prognostic factor[80]. Even though no pathology report is available to confirm extracapsular spread, the necrotic lymph nodes do have higher SUV values than the non-necrotic pathologic lymph nodes on PET scans with both the [^{18}F]FDG and [^{68}Ga]Ga-DOTA-RGD$_2$ tracer.
All the different aspects of the multimodal imaging performed in the case study are discussed in this chapter. Not only the aspects of the primary tumour, but also of the suspected and not-suspected lymph nodes and benign tissue to get a total view of the disease within this subject.

5.1 Imaging of the tumour

The TLG has been associated with a negative correlation to disease free survival in oropharyngeal carcinomas[48]. Whereas no cut-off values are noted by Gouw et al.[48], the TLG of the subject described in Chapter 4 ($117.5 grams$) can be placed in the top of the second quartile of HPV$^+$ tumours as well as the tumour volume. Contrarily, the SUV_{max} is higher than all found in HPV$^+$ tumours and in the top of the the range of the values found in T2 tumours, although these parameters had less correlation with disease free survival compared to volume and TLG. The TLG is calculated with the help of the SUV_{mean} and not the SUV_{max}, so only a small part of the tumour has a very high uptake. It is suggested by Smeets et al.[81] that intratumoural heterogeneity, caused by different genetic mutations within one tumour, can better classify the underlying tumour biology than single voxel parameters like SUV_{max} in pancreatic ductal adenocarcinomas. For example, a higher entropy was correlated to a lower overall survival, indicating that the large difference in SUV_{max} and SUV_{mean} could possibly result in lower overall survival. Therefore it is recommended to research the correlations between heterogeneity and survival in squamous cell carcinomas.

The tumour RGD SUV_{max} of 7.9 of the case study is comparable to that of the mean of 7.5 ± 2.6 found in HPV$^-$ tumours of the head and neck[45]. Therefore, no hint of pre-therapy difference is observed based on HPV positive status of this subject described in Chapter 4. The RGD uptake of the tumour in the case study did increase over time to 10.3, which is also observed in tumour models after irradiation[74]. For future evaluation of this research, it is interesting to see if this increase in uptake is correlated to therapy response or non-response.

In literature, CT perfusion parameters vary considerably due to a variation in analysis methods and software resulting in difficult correlation of absolute values. A study with a similar image analysis method performed CT perfusion in HNSCC and analysed this with the Patlak calculation model. Here, a mean flow of $55.6 \pm 29.5 ml/100ml/min$ was related to the patients not responding to therapy, whereas a mean of 76.9 ± 26.6 correlated with response[82]. In other studies in HNSCC, different calculation models are used, but mean AF values of $55.6 - 90.1 ml/100ml/min$ were correlated to non-responders and values ranging from $72.6 - 125.3 ml/100ml/min$ were found in patients responding to therapy[83, 84, 85, 86].

Furthermore, on basis of the Patlak model, a BV of $73.84 \pm 24.43 ml/100ml$ was correlated to response and 34.51 ± 7.4 was found in non-responders[82]. A baseline mean arterial flow of $97.9 ml/100ml/min$ and blood volume of $64.1 ml/100ml$ in the tumour of the case study can therefore suggest response to therapy.

The AF of the tumour is higher than of muscle tissue and interestingly, the submandibular and non-necrotic lymph node flow is even higher than the tumoural flow. Increased flow of blood within the tumour compared to normal tissue can be explained by the opening of arteriovenous shunts causing increased flow in microvessels and a higher production of new blood vessels[52]. Nevertheless, the benign lymph node in level 2 left has a higher BV and lower SUV_{max} and SUV_{mean} on the RGD scan which makes this explanation less likely. Furthermore, Goh et al.[87] researched the combination of CT perfusion parameters in rectal carcinomas, concluding that a pattern of high flow (AF) and low permeability (FE) was related to high interstitial pressure and a high vascularisation (AF) and high metabolism (FDG SUV_{max}) reflected matched perfusion. This high interstitial pressure in the tumour of this case study could in turn reflect acute vascular collapse and the matched perfusion may indicate a less aggressive phenotype. Mismatched perfusion concluded from high metablism and poor vascularisation, as is the case for especially LN_2.2, might possibly be an indicator of adaptation to intratumoural hypoxia and therefore a poorer prognosis due to therapy resistance[87].

The tumour and necrotic lymph node uptake of RGD is increased in the follow-up scan in the case study. A possible explanation might be that the tumour mass is trying to recover from irradiation. The CT perfusion differences in this study between the baseline and follow-up suggest a change in vascular permeability (FE) in the tumour. It can be hypothesized that this increased FE and slightly decreased BV and AF cause a shortage in nutrients and oxygen in a damaged tissue trying to recover. This shortage results in upregulated angiogenesis pathways and therefore RGD uptake. However, in a previous study to RGD imaging in irradiated tumour models, altered tumour uptake of RGD was not due to general tumour physiologic changes like vascular permeability or perfusion but only due to angiogenic changes[74]. Furthermore, in a study to rectal carcinomas, chemoradiation has been shown to decrease AF, FE and BV in the acute setting additionally, baseline lower values of AF or AF and BV were correlated to non-responders[88, 89, 90]. These values are however measured after completion of the 6 weeks of neo-adjuvant chemoradiotherapy and not during.

5.2 Imaging of the lymph nodes

In the case study, a distinction between necrotic and non-necrotic lymph nodes is made, additionally, a distinction between necrotic and cystic nodes can be made. Cystic nodes are defined as round or ovoid masses with an enhancing capsule of less than $2mm$ without an internal complex, irregular or solid area, closely correlated with HPV status of a tumour[91]. Therefore, the LN_L4.1 can be defined as a more cystic lymph node in stead of necrotic. From benign cysts, the central photopenia in FDG PET/CT scans is recognized because fluid does not have glucose uptake, and the thin capsule is too small for accurate PET recognition, explaining the lack of heightened uptake of RGD and FDG in this lymph node.

What is a surprising finding is that the oval necrotic lymph node LN_L4.2 and the non-necrotic retropharyngeal node (LN_RP) have, compared to the only slightly heightened RGD uptake, increased FDG uptake. The other necrotic lymph nodes have both heightened FDG and RGD uptake and the other non-necrotic nodes have similar uptake as muscle background. The FDG uptake in LN_L4.2 is localized in the borders of the mass. In previous studies with the ^{68}Ga-RGD$_2$ tracer, not all lymph node metastases could be identified, especially not when smaller than $5mm$[45] which can explain the SUV found in LN_L4.2 which had a large necrotic centre and in LN_RP with a volume of only $0.4ml$. This could possibly indicate that FDG might be superior for staging but RGD provides complementary information. This complementary information could in the future possibly be used for diagnostics, treatment planning and response evaluation of (personalized) therapies.

This complementary aspect of an RGD tracer compared to FDG PET scans is also previously concluded by Beer et al.[75]. In their study of malignant lesions (multiple origins), integrin $\alpha_v\beta_3$ expression and glucose metabolism was not closely linked. Other reports in literature describe contradictory results: In human lung adenocarcinomas, the microvessel density (MVD), a surrogate marker for proliferating endothelial cells in excised tumours, positively correlated with [^{18}F]FDG uptake[92]. Contrarily, in patients with non small cell lung cancer, no correlation was found between FDG and MVD by staining with von Willebrand factor, a regulator in blood vessel formation[93]. In this study, FDG and RGD values correspond relatively good in non-necrotic nodes and benign tissue but not in the tumour and the retropharyngeal non-necrotic node.

No differences in CT perfusion values have been documented for (necrotic) lymph nodes, while higher values have been observed in tumours without central necrosis[52]. In the case study, the non-necrotic lymph nodes had higher arterial flow and blood volume, whereas the FE and RGD uptake was higher in necrotic lymph nodes. The CT perfusion and PET parameters of these necrotic lymph nodes were similar to those of the tooth abscess at baseline, possibly indicating an inflammatory process as a result of the tumoural process in the lymph nodes with possible extranodal growth. Additionally, necrotic cell death has been shown to release proinflammatory signals into the surrounding tissue microenvironment[10]. Secondary, or due to this inflammation, possibly very leaky vasculature is present, as indicated by a high FE, which causes turbulance within the arteries and therefore inadequate and decreased blood flow. Furthermore, a low AF and BV could indicate insufficient perfusion and therefore resulting in central necrosis while the heightened RGD uptake could be due to the ability of the metastatic tumour cells to respond to hypoxia[87]. A hypothesis is that this previously noted combination might lead to clonal adaptation and the selection of more aggressive tumour-cell-clones[87]. In both RGD scans, the RGD uptake in the non-necrotic nodes is not very high, which could hint a sustained balance between the nutrient and oxygen delivery (AF) and the tumour metastases needs for these nutrients and therefore no heightened angiogenesis.

5.3 Benign tissue

After injection of the tracer, RGD uptake is dominated by the bladder, liver, kidneys and spleen[78]. Additionally the salivary glands, choroid plexus and thyroid tissue also have high uptake[45] which is also seen in the RGD scans in the case study. It is known that integrin $\alpha_v\beta_3$ bears a receptor site for T3 and T4 hormones of the thyroid[94]. Nonetheless, on basis of this preliminary evaluation, the thyroid FDG uptake of this subject is also enhanced. In the right lobe of the thyroid, a more focal enhanced FDG uptake is shown, evaluation with ultrasound showed no indication yet for malignancy but the focality indicates the potential for malignancy. Additionally, inflammation and an immune response also have a need for more glucose which could indicate that this heightened FDG and RGD uptake arises due to a (mild) thyreoiditis.

The highest FE value is found in the benign inflammation in the tooth abscess. Even though the RGD uptake is decreased during the follow-up scan which could indicate a milder inflammation or clearance of this inflammation, the FE is increased in the follow-up scan which could in turn indicate a more advanced inflammatory process. This discrepancy could be caused by a less reliable method of measuring the FE, explained in the sections below, and a partial volume effect due to the very small ROI that could be placed in this small region. The FE is the parameter for which the most assumptions should be made. Additional, in the FE color map photopenic areas can be seen (figure 16) demonstrating the inability of the software to calculate the FE in certain areas.

5.4 Analysis methods

The RGD tracer is developed to bind to integrin $\alpha_v\beta_3$, although other subtypes of integrins have also demonstrated to recognize the RGD sequence in a nanomolar range [44, 95] and showed its overexpression in several types of HNSCC[96]. In an evaluation study to ligands for RGD binding integrins, the c(RGDfK) has shown to predominantly bind integrin $\alpha_v\beta_3$,and has only in nanomolar range specificity for $\alpha_v\beta_6$[44]. Therefore, the uptake values of [^{68}Ga]Ga-DOTA-E-[c(RGDfK)]$_2$ could be generally correlated with integrin $\alpha_v\beta_3$ expression.

For more accurate CT perfusion analysis it is recommended to use a different calculation model, the Patlak model wrongly assumes irreversible transfer of contrast from the arterial to tissue compartment which can greatly influence the quantitative parameters. A more accurate model for especially the prediction of vascular leakage would be the Tofts or Extended Tofts model. A correct estimation is important because correlation between RGD uptake and vascular leakage could give insight in the functional capabilities of the new endothelium. As stated in Chapter 2, exposure to persistent stimulatory signals results in improper vessel function leading to, among others, increased vascular leakage. The measurement of the FE with the help of the used Patlak model is not very accurate including multiple areas in which no accurate measurement could take place, represented by a color void in the FE map in figure 16. Furthermore, the placement of 2D spheres do not accurately represent the structures with high uptake as concluded in Chapter 2, so a more accurate delineation is also needed that could be provided by different software.

5.5 Recommendations

In this preliminary analysis, only one subject was analysed. Important factors to take into account in the future when more data is acquired, is the correlation with uptake, the HPV status and local recurrence or control. Secondly, because in this subject a difference is found between necrotic and non-necrotic nodes, it is suggested that this could also be correlated to the uptake and local control when analysing more subjects. Furthermore, age and life style factors including smoking have been shown to correlate to overall survival[48]. This is an important confounder to take into account, considering that patients with HPV$^+$ tumours tend to have life style factors related to improved prognosis whereas patients HPV$^-$ tumours are likely to have worse life style factors.

An overall advantage of this study is the scanning in head and neck mask, resulting in less deformation of anatomical structures between different scans. Even though the head is stabilized, a swallowing motion can not be prevented during the relatively long scanning times and increasing irritation in a subject treated with radiation therapy and therefore the motion correction embedded in the CT perfusion software used did not suffice. Furthermore, between the three PET/CT scans some structures have deviated which makes the copying of a VOI to the other scans impossible resulting in having to adjust the VOIs for each scan. A possible solution might be a more accurate registration method.

Regarding tumour delineation, a deliberation between a method reflecting the uptake best and a correlation to values found in literature should be made. Next to the VOI definition methods discussed in Chapter 2, it is shown that fixed threshold of SUV 2.5 on FDG PET/CT outperformed a fixed threshold of SUV 3 and relative thresholds on basis of percentages of SUV_{max} for determination of metabolic tumour volume (MTV)[46]. The performance of this delineation method could not be compared to the other segmentation methods because only RGD PET/CT data was available.

For more accurate CT perfusion analysis it is recommended to use a different calculation model, the Patlak model wrongly assumes irreversible transfer of contrast from the arterial to tissue compartment which can greatly influence the quantitative parameters. A more accurate model would be the Tofts or Extended Tofts model.

Many methods and values can be used to analyse PET images. Parameters of potential added benefit could be which define the heterogeneity of SUV values within the tumour[81], as it is suggested that decreased tumour heterogeneity is measured in HPV positive tumours compared to HPV negative[97]. The question whether the analysis method has added value and if it indeed correctly reflects the parameter it should represent should be kept in mind. For example, the SUV values of a lesion of $1mm$ do not correctly represent the activity located within that region because of the resolution limitations of PET.

5.6 Conclusion

The multimodal imaging case study provides possible positive correlations but also negative correlations with overall survival when compared to literature. The most and best comparable parameters like TLG, the AF and BV could point towards a response, which is also expected on basis of the HPV^{+} status of the tumour and the life style parameters correated to good prognosis of this subject.

Furthermore, increased RGD uptake is seen in necrotic lymph nodes and in the tumour when comparing the baseline and follow-up scan. It could be hypothesized that enhanced angiogenesis capabilities during therapy would result in a persistence of a non-hypoxic tumour environment and therefore persistent response to concomitant chemoradiotherapy.

If during early phases of treating a HNSCC (in)effectiveness of the treatment can be indicated by a combination of scans like RGD PET/CT and CT perfusion, the morbidity due to ineffective treatments can be reduced in this fragile patient population.

References

[1] F. Bray, J. Ferlay, I. Soerjomataram, R. Siegel, L. Torre, and A. Jemal, "Global cancer statistics 2018: GLOBOCAN estimates of incidence and mortality worldwide for 36 cancers in 185 countries," *CA: A Cancer Journal for Clinicians*, vol. 68, no. 6, pp. 394–424, 2018.

[2] https://www.cijfersoverkanker.nl/, "Date Accessed: 12-11-2019," 2019.

[3] J. Honings, "Samenvatting van protocollen en richtlijnen diagnostiek en behandeling van maligne hoofd-hals tumoren in het RadboudUMC," tech. rep., Radboud UMC, Nijmegen, 2018.

[4] R. Nunes, M. Morale, G. Silva, L. Villa, and L. Termini, "Innate immunity and HPV: Friends or foes," *Clinics*, vol. 73, no. Suppl 1, 2018.

[5] P. Nguyen-Tan, Q. Zhang, K. Ang, R. Weber, D. Rosenthal, D. Soulieres, H. Kim, C. Silverman, A. Raben, T. Galloway, A. Fortin, E. Gore, W. Westra, C. Chung, R. Jordan, M. Gillison, M. List, and Q. Le, "Randomized phase III trial to test accelerated versus standard fractionation in combination with concurrent cisplatin for head and neck carcinomas in the radiation therapy oncology group 0129 trial: Long-term report of efficacy and toxicity," *Journal of Clinical Oncology*, vol. 32, no. 34, pp. 3858–3867, 2014.

[6] A. Andersen, A. Koldjaer Sølling, T. Ovesen, and M. Rusan, "The interplay between HPV and host immunity in head and neck squamous cell carcinoma," *International Journal of Cancer*, vol. 134, no. 12, pp. 2755–2763, 2014.

[7] E. Crosbie, M. Einstein, S. Franceschi, and H. Kitchener, "Human papillomavirus and cervical cancer," *The Lancet*, vol. 382, no. 9895, pp. 889–899, 2013.

[8] L. Barnes, J. Eveson, P. Reichart, and D. Sidransky, *World Health Organization Classification of Tumours: Pathology and Genetics of Head and Neck Tumours*. Lyon: IARC, 3rd ed., 2005.

[9] J. Grandis and D. Tweardy, "Elevated Levels of Transforming Growth Factor a and Epidermal Growth Factor Receptor Messenger RNA Are Early Markers of Carcinogenesis in Head and Neck Cancer," *cancer research*, vol. 53, pp. 3579–3584, 1993.

[10] D. Hanahan and R. Weinberg, "Hallmarks of cancer: The next generation," *Cell*, vol. 144, no. 5, pp. 646–674, 2011.

[11] M. Sartor, H. Steingrimsdottir, F. Elamin, J. Gäken, S. Warnakulasuriya, M. Partridge, N. Thakker, N. Johnson, and M. Tavassoli, "Role of p16/MTS1, cyclin D1 and RB in primary oral cancer and oral cancer cell lines," *British Journal of Cancer*, vol. 80, no. 1-2, pp. 79–86, 1999.

[12] B. Werness, A. Levine, and P. Howley, "Association of human papillomavirus types 16 and 18 E6 proteins with p53," *Science*, vol. 248, no. 4951, pp. 76–79, 1990.

[13] http://atlasgeneticsoncology.org/Tumors/HeadNeckSCCID5078.html, "Date Accessed: 06-01-2020."

[14] M. Gillison, J. Harris, W. Westra, C. Chung, R. Jordan, D. Rosenthal, P. Nguyen-Tan, W. Spanos, K. Redmond, and K. Ang, "Survival outcomes by tumor human papillomavirus (HPV) status in stage III-IV oropharyngeal cancer (OPC) in RTOG 0129," *Journal of Clinical Oncology*, vol. 27, no. 15s, p. 6003, 2009.

[15] C. Wittekindt, E. Gültekin, S. Weissenborn, H. Dienes, H. Pfister, and J. Klussmann, "Expression of p16 Protein Is Associated with Human Papillomavirus Status in Tonsillar Carcinomas and Has Implications on Survival," *Current Research in Head and Neck Cancer*, vol. 62, pp. 72–80, 2004.

[16] J. Kelly, Z. Husain, and B. Burtness, "Treatment de-intensification strategies for head and neck cancer," *European Journal of Cancer*, vol. 68, pp. 125–133, 2016.

[17] M. Gillison, A. Trotti, J. Harris, A. Eisbruch, P. Harari, D. Adelstein, E. Sturgis, B. Burtness, J. Ridge, J. Ringash, J. Galvin, M. Yao, S. Koyfman, D. Blakaj, M. Razaq, A. Colevas, J. Beitler, C. Jones, N. Dunlap, S. Seaward, S. Spencer, T. Galloway, J. Phan, J. Dignam, and Q. Le, "Radiotherapy plus cetuximab or cisplatin in human papillomavirus-positive oropharyngeal cancer (NRG Oncology RTOG 1016): a randomised, multicentre, non-inferiority trial," *The Lancet*, vol. 393, no. 10166, pp. 40–50, 2019.

[18] S. Jo, A. Juhasz, K. Zhang, C. Ruel, S. Loera, S. Wilczynski, Y. Yen, X. Liu, J. Ellenhorn, D. Lim, B. Paz, G. Somlo, N. Vora, and S. Shibata, "Human papillomavirus infection as a prognostic factor in oropharyngeal squamous cell carcinomas treated in a prospective phase II clinical trial.," *Anticancer research*, vol. 29, no. 5, pp. 1467–1474, 2009.

[19] Y. Jauw, M. Huisman, T. Nayak, D. Vugts, R. Christen, V. Naegelen, D. Ruettinger, F. Heil, A. Lammertsma, H. Verheul, O. Hoekstra, G. van Dongen, and C. Menke-van der Houven van Oordt, "Assessment of target-mediated uptake with immuno-PET: analysis of a phase I clinical trial with an anti-CD44 antibody," *European Journal of Nuclear Medicine and Molecular Imaging Research*, vol. 8, no. 1, p. 6, 2018.

[20] X. Sun, Z. Xiao, G. Chen, Z. Han, Y. Liu, C. Zhang, Y. Sun, Y. Song, K. Wang, F. Fang, X. Wang, Y. Lin, L. Xu, L. Shao, J. Li, Z. Cheng, S. Gambhir, and B. Shen, "A PET imaging approach for determining EGFR mutation status for improved lung cancer patient management," *Science Translational Medicine*, vol. 10, no. 431, 2018.

[21] W. Cai, K. Chen, L. He, Q. Cao, A. Koong, and X. Chen, "Quantitative PET of EGFR expression in xenograft-bearing mice using 64Cu-labeled cetuximab, a chimeric anti-EGFR monoclonal antibody," *European Journal of Nuclear Medicine and Molecular Imaging*, vol. 34, no. 6, pp. 850–858, 2007.

[22] E. Graves, R. Hicks, D. Binns, M. Bressel, Q. Le, L. Peters, R. Young, and D. Rischin, "Quantitative and qualitative analysis of [18F]FDG and [18F]FAZA positron emission tomography of head and neck cancers and associations with HPV status and treatment outcome," *European Journal of Nuclear Medicine and Molecular Imaging*, vol. 43, no. 4, pp. 617–625, 2016.

[23] I. Grassi, C. Nanni, G. Cicoria, C. Blasi, F. Bunkheila, E. Lopci, P. Colletti, D. Rubello, and S. Fanti, "Usefulness of 64Cu-ATSM in head and neck cancer: A preliminary prospective study," *Clinical Nuclear Medicine*, vol. 39, no. 1, pp. 59–63, 2014.

[24] M. Kikuchi, T. Yamane, S. Shinohara, K. Fujiwara, S. Hori, Y. Tona, H. Yamazaki, Y. Naito, and M. Senda, "18F-fluoromisonidazole positron emission tomography before treatment is a predictor of radiotherapy outcome and survival prognosis in patients with head and neck squamous cell carcinoma," *Annals of Nuclear Medicine*, vol. 25, no. 9, pp. 625–633, 2011.

[25] L. Ellis and I. Fidler, "Angiogenesis and metastasis," *European Journal of Cancer*, vol. 32, no. 14, pp. 2451–2460, 1996.

[26] T. Reynolds, S. Rockwell, and P. Glazer, "Genetic instability induced by the tumor microenvironment," *Cancer Research*, vol. 56, no. 24, pp. 5754–5757, 1996.

[27] K. Miles, C. Charnsangavej, F. Lee, E. Fishman, K. Horton, and T. Lee, "Application of CT in the investigation of angiogenesis in oncology," *Academic Radiology*, vol. 7, no. 10, pp. 840–850, 2000.

[28] S. Weis and D. Cheresh, "Tumor angiogenesis: molecular pathways and therapeutic targets," *Nature Medicine*, vol. 17, no. 11, pp. 1359–1370, 2011.

[29] M. De Palma, D. Biziato, and T. Petrova, "Microenvironmental regulation of tumour angiogenesis," *Nature Reviews Cancer*, vol. 17, no. 8, pp. 457–474, 2017.

[30] H. Hong, F. Chen, Y. Zhang, and W. Cai, "New radiotracers for imaging of vascular targets in angiogenesis-related diseases," *Advanced Drug Delivery Reviews*, vol. 76, no. 1, pp. 2–20, 2014.

[31] J. Holash, P. C. Maisonpierre, D. Compton, P. Boland, C. R. Alexander, D. Zagzag, G. D. Yancopoulos, and S. J. Wiegand, "Vessel cooption, regression, and growth in tumors mediated by angiopoietins and VEGF," *Science*, vol. 284, no. 5422, pp. 1994–1998, 1999.

[32] P. Carmeliet and R. Jain, "Molecular mechanisms and clinical applications of angiogenesis," *Nature*, vol. 473, pp. 298–307, 2011.

[33] N. Almog, L. Ma, R. Raychowdhury, C. Schwager, R. Erber, S. Short, L. Hlatky, P. Vajkoczy, P. Huber, J. Folkman, and A. Abdollahi, "Transcriptional switch of dormant tumors to fast-growing angiogenic phenotype," *Cancer Research*, vol. 69, no. 3, pp. 836–844, 2009.

[34] R. García-Figueiras, A. Padhani, A. Beer, S. Baleato-González, J. Vilanova, A. Luna, L. Oleaga, A. Gómez-Caamaño, and D. Koh, "Imaging of Tumor Angiogenesis for Radiologists-Part 1: Biological and Technical Basis," *Current Problems in Diagnostic Radiology*, vol. 44, no. 5, pp. 407–424, 2015.

[35] J. Humphries, A. Byron, and M. Humphries, "Integrin ligands at a glance," *Journal of Cell Science*, vol. 119, no. 19, pp. 3901–3903, 2006.

[36] N. Withofs, N. Signolle, J. Somja, P. Lovinfosse, E. Nzaramba, F. Mievis, F. Giacomelli, D. Waltregny, D. Cataldo, S. Gambhir, and R. Hustinx, "18F-FPRGD2 PET/CT imaging of integrin $\alpha v\beta 3$ in renal carcinomas: Correlation with histopathology," *Journal of Nuclear Medicine*, vol. 56, no. 3, pp. 361–364, 2015.

[37] H. Wu, H. Chen, Y. Sun, Y. Wan, F. Wang, B. Jia, and X. Su, "Imaging integrin $\alpha v\beta 3$ positive glioma with a novel RGD dimer probe and the impact of antiangiogenic agent (Endostar) on its tumor uptake," *Cancer Letters*, vol. 335, no. 1, pp. 75–80, 2013.

[38] M. Janssen, W. Oyen, I. Dijkgraaf, L. Massuger, C. Frielink, D. Edwards, M. Rajopadhye, H. Boonstra, F. Corstens, and O. Boerman, "Tumor targeting with radiolabeled $\alpha v\beta 3$ integrin binding peptides in a nude mouse model," *Cancer Research*, vol. 62, no. 21, pp. 6146–6151, 2002.

[39] R. Haubner, H. Wester, W. Weber, C. Mang, S. Ziegler, S. Goodman, R. Senekowitsch-Schmidtke, H. Kessler, and M. Schwaiger, "Noninvasive imaging of $\alpha v\beta 3$ integrin expression using 18 F-labeled RGD-containing glycopeptide and positron emission tomography," *Cancer Research*, vol. 61, no. 5, pp. 1781–1785, 2001.

[40] S. Terry, K. Abiraj, C. Frielink, L. Van Dijk, J. Bussink, W. Oyen, and O. Boerman, "Imaging integrin $\alpha v\beta 3$ on blood vessels with 111In-RGD2 in head and neck tumor xenografts," *Journal of Nuclear Medicine*, vol. 55, no. 2, pp. 281–286, 2014.

[41] I. Dijkgraaf, C. Yim, G. Franssen, R. Schuit, G. Luurtsema, S. Liu, W. Oyen, and O. Boerman, "PET imaging of $\alpha v\beta 3$ integrin expression in tumours with 68Ga-labelled mono-, di- and tetrameric RGD peptides," *European Journal of Nuclear Medicine and Molecular Imaging*, vol. 38, no. 1, pp. 128–137, 2011.

[42] I. Dijkgraaf, J. Kruijtzer, S. Liu, A. Soede, W. Oyen, F. Corstens, R. Liskamp, and O. Boerman, "Improved targeting of the $\alpha v\beta 3$ integrin by multimerisation of RGD peptides," *European Journal of Nuclear Medicine and Molecular Imaging*, vol. 34, no. 2, pp. 267–273, 2007.

[43] D. Lobeek, G. Franssen, M. Ma, H. Wester, C. Decristoforo, W. Oyen, O. Boerman, S. Terry, and M. Rijpkema, "In vivo characterization of four 68Ga-labeled multimeric RGD peptides to image $\alpha v\beta 3$ integrin expression in two human tumor xenograft mouse models.," *Journal of nuclear medicine*, vol. 59, no. 8, pp. 1296–1301, 2018.

[44] T. Kapp, F. Rechenmacher, S. Neubauer, O. Maltsev, E. Cavalcanti-Adam, R. Zarka, U. Reuning, J. Notni, H. Wester, C. Mas-Moruno, J. Spatz, B. Geiger, and H. Kessler, "A comprehensive evaluation of the activity and selectivity profile of ligands for RGD-binding integrins," *Scientific Reports*, vol. 7, no. 93805, 2017.

[45] D. Lobeek, M. Rijpkema, S. Terry, J. Molkenboer-Keunen, L. Joosten, E. van Genugten, I. van Engen-van Grusven, S. Pegge, W. Oyen, O. Boerman, W. Weijs, M. Merkx, C. van Herpen, R. Takes, and E. Aarntzen, "Imaging angiogenesis in patients with head an neck squamous cell carcinomas by [68Ga]Ga-DOTA-E-[c(RGDfK)]2 PET/CT," *Manuscript submitted for publication*, 2020.

[46] C. Kao, S. Lin, T. Hsieh, K. Yen, S. Yang, Y. Wang, J. Liang, C. Hua, and S. Chen, "Use of pretreatment metabolic tumour volumes to predict the outcome of pharyngeal cancer treated by definitive radiotherapy," *European Journal of Nuclear Medicine and Molecular Imaging*, vol. 39, no. 8, pp. 1297–1305, 2012.

[47] A. Sanchez-Crespo, "Comparison of Gallium-68 and Fluorine-18 imaging characteristics in positron emission tomography," *Applied Radiation and Isotopes*, vol. 76, pp. 55–62, 2013.

[48] Z. Gouw, M. La Fontaine, S. Van Kranen, J. Van De Kamer, W. Vogel, E. Van Werkhoven, J. Sonke, and A. Al-Mamgani, "The Prognostic Value of Baseline 18F-FDG PET/CT in Human Papillomavirus-Positive Versus Human Papillomavirus-Negative Patients with Oropharyngeal Cancer," *Clinical Nuclear Medicine*, vol. 44, no. 5, pp. E323–E328, 2019.

[49] Z. Zhao, S. Ji, X. Li, W. Fang, and S. Liu, "68 Ga-labeled dimeric and trimeric cyclic RGD peptides as potential PET radiotracers for imaging gliomas," *Applied Radiation and Isotopes*, vol. 148, pp. 168–177, 2019.

[50] A. Iagaru, C. Mosci, B. Shen, F. Chin, E. Mittra, M. Telli, and S. Gambhir, "18F-FPPRGD2 PET/CT: Pilot Phase Evaluation of Breast Cancer Patients," *Radiology*, vol. 273, no. 2, pp. 549–559, 2014.

[51] A. Beer, A. Grosu, J. Carlsen, A. Kolk, M. Sarbia, I. Stangier, P. Watzlowik, H. Wester, R. Haubner, and M. Schwaiger, "[18F]Galacto-RGD positron emission tomography for imaging of $\alpha v\beta 3$ expression on the neovasculature in patients with squamous cell carcinoma of the head and neck," *Clinical Cancer Research*, vol. 13, no. 22, pp. 6610–6616, 2007.

[52] G. Petralia, L. Bonello, S. Viotti, L. Preda, G. D'Andrea, and M. Bellomi, "CT perfusion in oncology: How to do it," *Cancer Imaging*, vol. 10, no. 1, pp. 8–19, 2010.

[53] C. A. Cuenod and D. Balvay, "Perfusion and vascular permeability: Basic concepts and measurement in DCE-CT and DCE-MRI," *Diagnostic and Interventional Imaging*, vol. 94, no. 12, pp. 1187–1204, 2013.

[54] A. A. Konstas, G. V. Goldmakher, T. Y. Lee, and M. H. Lev, "Theoretic basis and technical implementations of CT perfusion in acute ischemic stroke, part 1: Theoretic basis," *American Journal of Neuroradiology*, vol. 30, no. 4, pp. 662–668, 2009.

[55] L. Faggioni, E. Neri, and C. Bartolozzi, "CT perfusion of head and neck tumors: How we do it," *American Journal of Roentgenology*, vol. 194, no. 1, pp. 62–69, 2010.

[56] K. Miles, "Perfusion CT for the assessment of tumour vascularity: which protocol?," *The British Journal of Radiology*, vol. 76, pp. S36–S42, 2003.

[57] S. Sourbron and D. Buckley, "Classic models for dynamic contrast-enhanced MRI," *NMR in Biomedicine*, vol. 26, no. 8, pp. 1004–1027, 2013.

[58] T. Niu, P. Yang, X. Sun, T. Mao, L. Xu, N. Yue, Y. Kuang, L. Shi, and K. Nie, "Variations of quantitative perfusion measurement on dynamic contrast enhanced CT for colorectal cancer: Implication of standardized image protocol," *Physics in Medicine and Biology*, vol. 63, no. 16, 2018.

[59] J. Oosterbroek, E. Bennink, M. E. Philippens, C. P. Raaijmakers, M. A. Viergever, and H. W. De Jong, "Comparison of DCE-CT models for quantitative evaluation of Ktrans in larynx tumors," *Physics in Medicine and Biology*, vol. 60, no. 9, pp. 3759–3773, 2015.

[60] J. Hsieh, *Computed Tomography: Principles, Design, Artifacts, and Recent Advances*. Bellingham: SPIE, 2003.

[61] K. St Lawrence and T. Lee, "An adiabatic approximation to the tissue homogeneity model for water exchange in the brain: I. Theoretical derivation.," *Journal of cerebral blood flow and metabolism : official journal of the International Society of Cerebral Blood Flow and Metabolism*, vol. 18, p. 1377, 12 1998.

[62] P. Tofts, G. Brix, D. Buckley, J. Evelhoch, E. Henderson, M. Knopp, H. Larsson, T. Lee, N. Mayr, G. Parker, R. Port, J. Taylor, and R. Weisskoff, "Estimating kinetic parameters from dynamic contrast-enhanced t1-weighted MRI of a diffusable tracer: Standardized quantities and symbols," *Journal of Magnetic Resonance Imaging*, vol. 10, no. 3, pp. 223–232, 1999.

[63] L. Kershaw and H. Cheng, "Temporal resolution and SNR requirements for accurate DCE-MRI data analysis using the AATH model," *Magnetic Resonance in Medicine*, vol. 64, no. 6, pp. 1772–1780, 2010.

[64] A. Heye, M. Thrippleton, P. Armitage, M. Valdés Hernández, S. Makin, A. Glatz, E. Sakka, and J. Wardlaw, "Tracer kinetic modelling for DCE-MRI quantification of subtle blood-brain barrier permeability," *NeuroImage*, vol. 125, pp. 446–455, 2016.

[65] C. Patlak, R. Blasberg, and J. Fenstermacher, "Graphical evaluation of blood-to-brain transfer constants from multiple-time uptake data," *Journal of Cerebral Blood Flow and Metabolism*, vol. 3, no. 1, pp. 1–7, 1983.

[66] J. Logan, J. Fowler, N. Volkow, A. Wolf, S. Dewey, D. Schlyer, R. MacGregor, R. Hitzemann, B. Bendriem, S. John Gatley, and D. Christman, "Graphical analysis of reversible radioligand binding from time-activity measurements applied to [N-11C-methyl]-(-)-cocaine PET studies in human subjects," *Journal of Cerebral Blood Flow and Metabolism*, vol. 10, no. 5, pp. 740–747, 1990.

[67] F. Mazzei, L. Volterrani, S. Guerrini, N. Squitieri, E. Sani, G. Bettini, C. Pozzessere, and M. Mazzei, "Reduced Time CT Perfusion Acquisitions Are Sufficient to Measure the Permeability Surface Area Product with a Deconvolution Method," *BioMed Research International*, pp. 1–6, 2014.

[68] L. Ostergaard, A. Sorensen, K. Kwong, R. Weisskoff, C. Gyldensted, and B. Rosen, "High resolution measurement of cerebral blood flow using intravascular tracer bolus passages. Part II: Experimental comparison and preliminary results.," *Magnetic resonance in medicine*, vol. 36, no. 5, pp. 726–736, 1996.

[69] K. A. Miles, T. Y. Lee, V. Goh, E. Klotz, C. Cuenod, S. Bisdas, A. M. Groves, M. P. Hayball, R. Alonzi, and T. Brunner, "Current status and guidelines for the assessment of tumour vascular support with dynamic contrast-enhanced computed tomography," *European Radiology*, vol. 22, no. 7, pp. 1430–1441, 2012.

[70] E. Klotz, U. Haberland, G. Glatting, S. Schoenberg, C. Fink, U. Attenberger, and T. Henzler, "Technical prerequisites and imaging protocols for CT perfusion imaging in oncology," *European Journal of Radiology*, vol. 84, no. 12, pp. 2359–2367, 2015.

[71] J. Dankbaar, J. Oosterbroek, E. Jager, H. de Jong, C. Raaijmakers, S. Willems, C. Terhaard, M. Philippens, and F. Pameijer, "Detection of cartilage invasion in laryngeal carcinoma with dynamic contrast-enhanced CT," *Laryngoscope Investigative Otolaryngology*, vol. 2, no. 6, pp. 373–379, 2017.

[72] M. Oei, J. van Gemert, J. Abbink, F. Meijer, J. Dankbaar, K. Thijn, S. Willems, R. van Es, A. Rosenberg, R. Koole, M. Prokop, and E. van Cann, "Assessment of mandibular invasion by oral squamous cell carcinoma with perfusion CT – a pilot study," *Manuscript submitted for publication*, 2020.

[73] D. Longo and L. Chow, "Head and Neck Cancer," *New England Journal of Medicine*, vol. 382, no. 1, pp. 60–72, 2020.

[74] S. Terry, K. Abiraj, J. Lok, D. Gerrits, G. Franssen, W. Oyen, and O. Boerman, "Can 111In-RGD2 Monitor Response to Therapy in Head and Neck Tumor Xenografts?," *Journal of Nuclear Medicine*, vol. 55, no. 11, pp. 1849–1855, 2014.

[75] A. Beer, S. Lorenzen, S. Metz, K. Herrmann, P. Watzlowik, H. Wester, C. Peschel, F. Lordick, and M. Schwaiger, "Comparison of integrin $\alpha v\beta 3$ expression and glucose metabolism in primary and metastatic lesions in cancer patients: A PET study using 18 F-galacto-RGD and 18 F-FDG," *Journal of Nuclear Medicine*, vol. 49, no. 1, pp. 22–29, 2008.

[76] R. Khan, "Lymph Node Disease and Advanced Head and Neck Imaging: A Review of the 2013 Literature," *Current Radiology Reports*, vol. 2, no. 8, 2014.

[77] R. Smith-Bindman, J. Lipson, R. Marcus, K. Kim, M. Mahesh, R. Gould, A. Berrington De González, and D. Miglioretti, "Radiation dose associated with common computed tomography examinations and the associated lifetime attributable risk of cancer," *Archives of Internal Medicine*, vol. 169, no. 22, pp. 2078–2086, 2009.

[78] V. López-Rodríguez, C. Galindo-Sarco, F. García-Pérez, G. Ferro-Flores, O. Arrieta, and M. Ávila-Rodríguez, "PET-based human dosimetry of the dimeric $\alpha v\beta 3$ integrin ligand 68 Ga-DOTA-E-[c(RGDfK)]2 , a potential tracer for imaging tumor angiogenesis," *Journal of Nuclear Medicine*, vol. 57, no. 3, pp. 404–409, 2016.

[79] http://powerandsamplesize.com/Calculators/Compare-2-Means/2-Sample-Equality, "Date Accessed: 01-04-2019," 2018.

[80] Y. H. Joo, I. R. Yoo, K. J. Cho, J. O. Park, I. C. Nam, and M. S. Kim, "Extracapsular spread and FDG PET/CT correlations in oral squamous cell carcinoma," *International Journal of Oral and Maxillofacial Surgery*, vol. 42, no. 2, pp. 158–163, 2013.

[81] E. Smeets, D. Withaar, W. Grootjans, J. Hermans, K. van Laarhoven, L. de Geus-Oei, M. Gotthardt, and E. Aarntzen, "Optimal respiratory-gated [18F]FDG PET/CT significantly impacts the quantification of metabolic parameters and their correlation with overall survival in patients with pancreatic ductal adenocarcinoma," *European Journal of Nuclear Medicine and Molecular Imaging Research*, vol. 9, no. 24, 2019.

[82] K. Surlan Popovic, S. Lukic, and P. Popovic, "Pretreatment perfusion CT and CT volumetry in squamous cell carcinoma of the head and neck region," *J Buon*, vol. 19, no. 4, pp. 937–943, 2014.

[83] K. Surlan-Popovic, S. Bisdas, Z. Rumboldt, T. S. Koh, and P. Strojan, "Changes in perfusion CT of advanced squamous cell carcinoma of the head and neck treated during the course of concomitant chemoradiotherapy," *American Journal of Neuroradiology*, vol. 31, no. 3, pp. 570–575, 2010.

[84] A. Zima, R. Carlos, D. Gandhi, I. Case, T. Teknos, and S. K. Mukherji, "Can pretreatment CT perfusion predict response of advanced squamous cell carcinoma of the upper aerodigestive tract treated with induction chemotherapy?," *American Journal of Neuroradiology*, vol. 28, no. 2, pp. 328–334, 2007.

[85] L. Rana, S. Sharma, S. Sood, B. Singh, M. Gupta, R. Minhas, A. Jhobta, V. Bhatia, and B. Venkat, "Volumetric CT perfusion assessment of treatment response in head and neck squamous cell carcinoma: Comparison of CT perfusion parameters before and after chemoradiation therapy," *European Journal of Radiology Open*, vol. 2, pp. 46–54, 2015.

[86] D. Gandhi, D. Chepeha, T. Miller, R. Carlos, C. Bradford, R. Karamchandani, F. Worden, A. Eisbruch, T. Teknos, G. Wolf, and S. Mukherji, "Correlation between initial and early follow-up CT perfusion parameters with endoscopic tumor response in patients with advanced squamous cell carcinomas of the oropharynx treated with organ-preservation therapy.," *AJNR. American journal of neuroradiology*, vol. 27, no. 1, pp. 101–106, 2006.

[87] V. Goh and R. Glynne-Jones, "Perfusion CT imaging of colorectal cancer.," *The British journal of radiology*, vol. 87, no. 1034, p. 20130811, 2014.

[88] L. Curvo-Semedo, M. Portilha, C. Ruivo, M. Borrego, J. Leite, and F. Caseiro-Alves, "Usefulness of Perfusion CT to Assess Response to Neoadjuvant Combined Chemoradiotherapy in Patients with Locally Advanced Rectal Cancer," *Academic Radiology*, vol. 19, no. 2, pp. 203–213, 2012.

[89] M. Bellomi, G. Petralia, A. Sonzogni, M. Zampino, and A. Rocca, "CT perfusion for the monitoring of neoadjuvant chemotherapy and radiation therapy in rectal carcinoma: Initial experience," *Radiology*, vol. 244, no. 2, pp. 486–493, 2007.

[90] D. Sahani, S. Kalva, L. Hamberg, P. Hahn, C. Willett, S. Saini, P. Mueller, and T. Lee, "Assessing tumor perfusion and treatment response in rectal cancer with multisection CT: Initial observations," *Radiology*, vol. 234, no. 3, pp. 785–792, 2005.

[91] D. Goldenberg, S. Begum, W. Westra, Z. Khan, J. Sciubba, S. Pai, J. Califano, R. Tufano, and W. Koch, "Cystic lymph node metastasis in patients with head and neck cancer: An HPV-associated phenomenon," *Head & Neck*, vol. 30, no. 7, pp. 898–903, 2008.

[92] J. Guo, K. Higashi, Y. Ueda, M. Oguchi, T. Takegami, H. Toga, T. Sakuma, H. Yokota, S. Katsuda, H. Tonami, and I. Yamamoto, "Microvessel density: correlation with 18F-FDG uptake and prognostic impact in lung adenocarcinomas.," *Journal of nuclear medicine : official publication, Society of Nuclear Medicine*, vol. 47, no. 3, pp. 419–425, 2006.

[93] M. Cherk, S. Foo, A. Poon, S. Knight, C. Murone, A. T. Papenfuss, J. I. Sachinidis, T. H. Saunder, G. J. O'Keefe, and A. M. Scott, "Lack of correlation of hypoxic cell fraction and angiogenesis with glucose metabolic rate in non-small cell lung cancer assessed by18F- fluoromisonidazole and18F-FDG PET," *Journal of Nuclear Medicine*, vol. 47, no. 12, pp. 1921–1926, 2006.

[94] B. LaFoya, J. Munroe, A. Miyamoto, M. Detweiler, J. Crow, T. Gazdik, and A. Albig, "Beyond the matrix: the many non-ECM ligands for integrins," *International Journal of Molecular Sciences*, vol. 19, no. 2, pp. 314–346, 2018.

[95] E. Ruoslahti, "RGD and other recognition sequences for integrins," *Annual Review of Cell and Developmental Biology*, no. 12, pp. 697–715, 1997.

[96] H. Ahmedah, L. Patterson, S. Shnyder, and H. Sheldrake, "RGD-Binding Integrins in Head and Neck Cancers," *Cancers (Basel)*, vol. 9, no. 6, p. 56, 2017.

[97] C. Schouten, S. Hakim, R. Boellaard, E. Bloemena, P. Doornaert, B. Witte, B. Braakhuis, R. Brakenhoff, C. Leemans, O. Hoekstra, and R. de Bree, "Interaction of quantitative 18F-FDG-PET-CT imaging parameters and human papillomavirus status in oropharyngeal squamous cell carcinoma," *Head & Neck*, vol. 38, no. 4, pp. 529–535, 2016.

A
Appendices

A.1 Additional figures

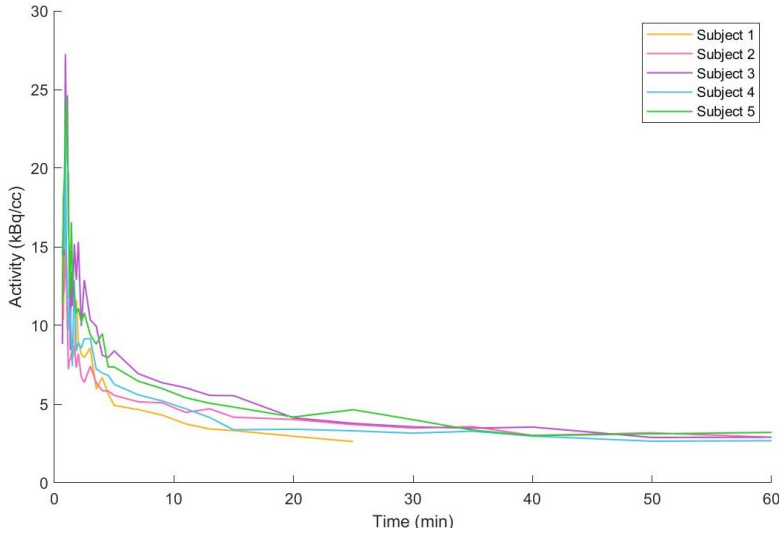

(a) Carotid artery

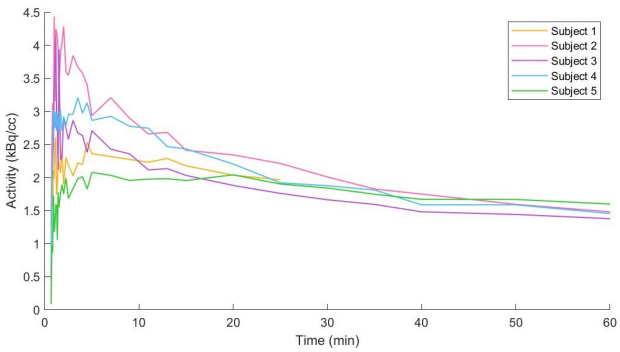

(b) Muscle

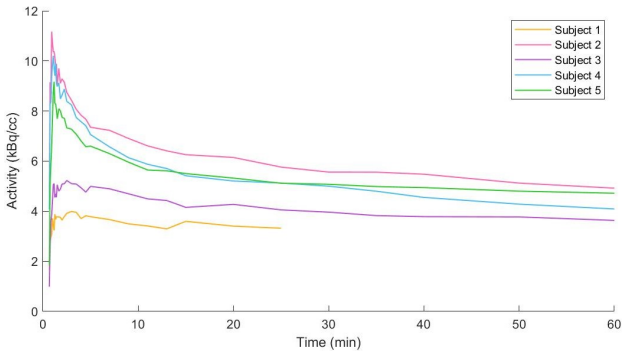

(c) Parotid gland

Figure A1: Mean activity within the three different structures until 60 minutes post injection of ^{68}Ga-RGD$_2$, for all the five subjects.

(a) A CT headrest

(b) The CT headrest insertion place

Figure A2: The fastening mechanism of CT headrests to the CT board

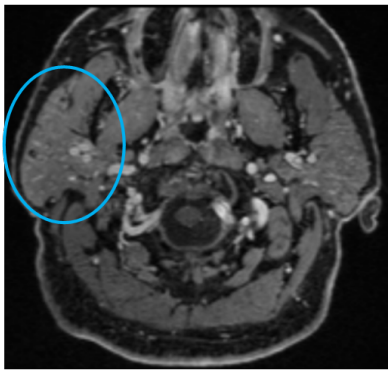

(a) Ipsilateral parotid gland

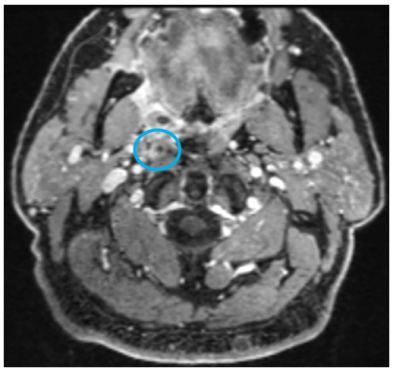

(b) Retropharyngeal lymph node

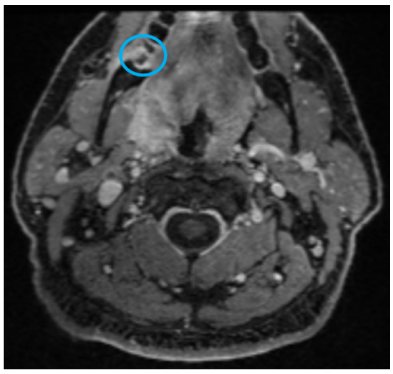

(c) Tooth abcess

Figure A3: The structures that are delineated on the different scans, annotated on the MR images, from cranial to caudal. T1 weighted, contrast enhanced, turbo spin echo sequence.

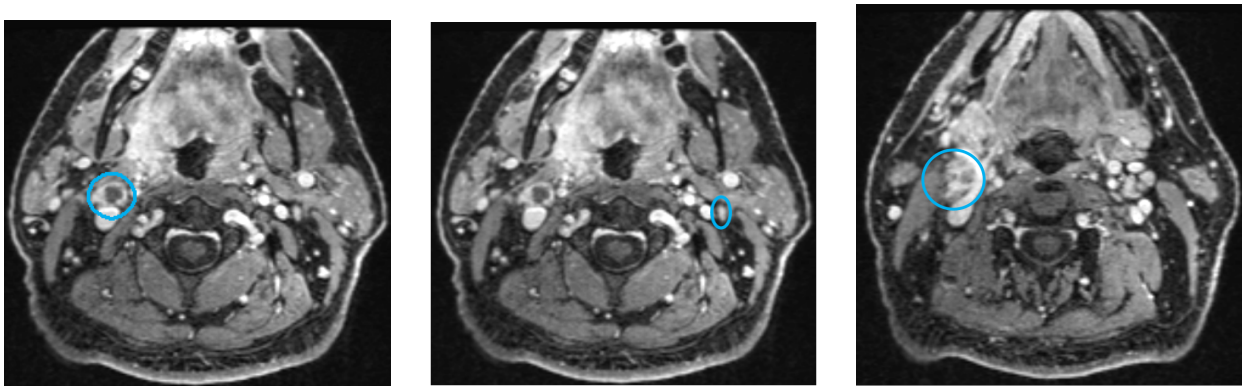

(a) Lymph node level 2 right (1) (b) Lymph node level 2 left (c) Lymph node level 2 right (2)

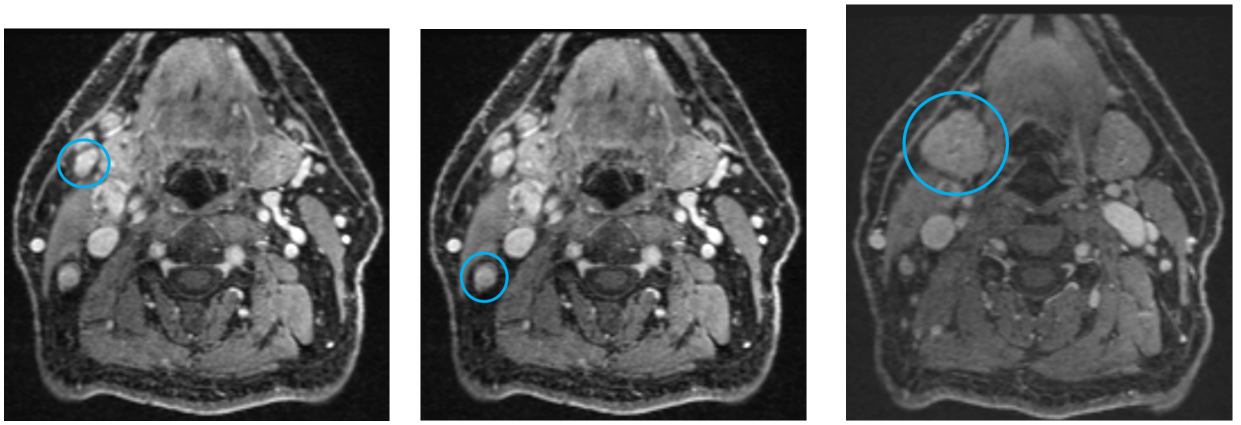

(d) Lymph node level 1b right (e) Lymph node level 2 right (3) (f) Ipsilateral submandibular gland

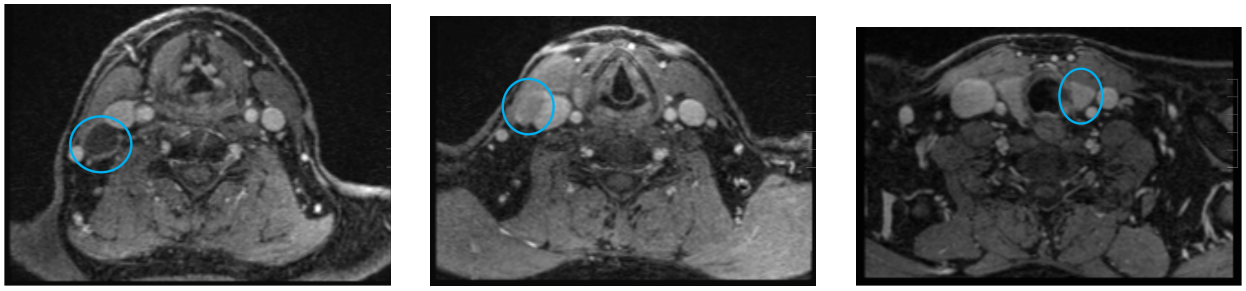

(g) Lymph node level 4 right (1) (h) Lymph node level 4 right (2) (i) Contralateral thyroid

Figure A4: The structures that are delineated on the different scans, annotated on the MR images, from cranial to caudal. T1 weighted, contrast enhanced, turbo spin echo sequence.

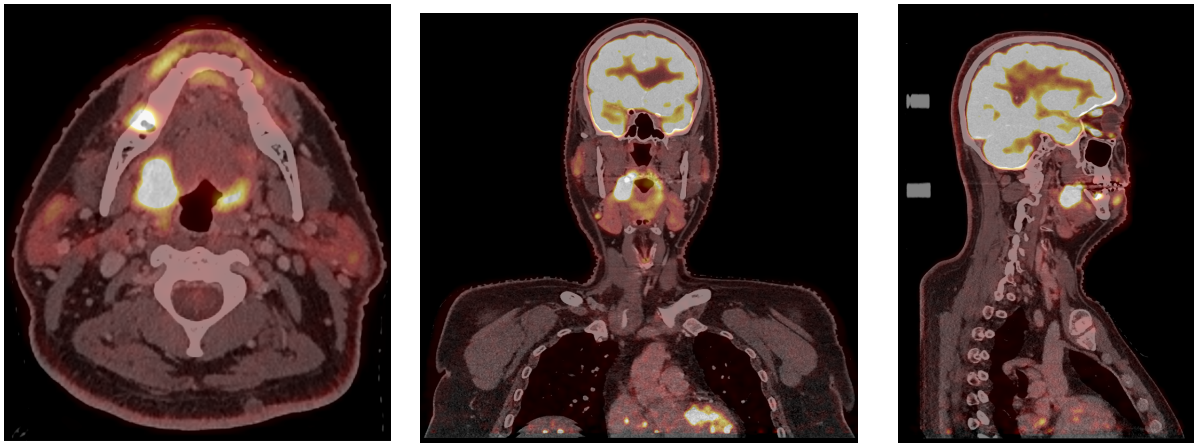

(a) axial (b) coronal (c) sagittal

Figure A5: The tumour in the right tonsil loge in three different views on FDG PET with a diagnostic CT

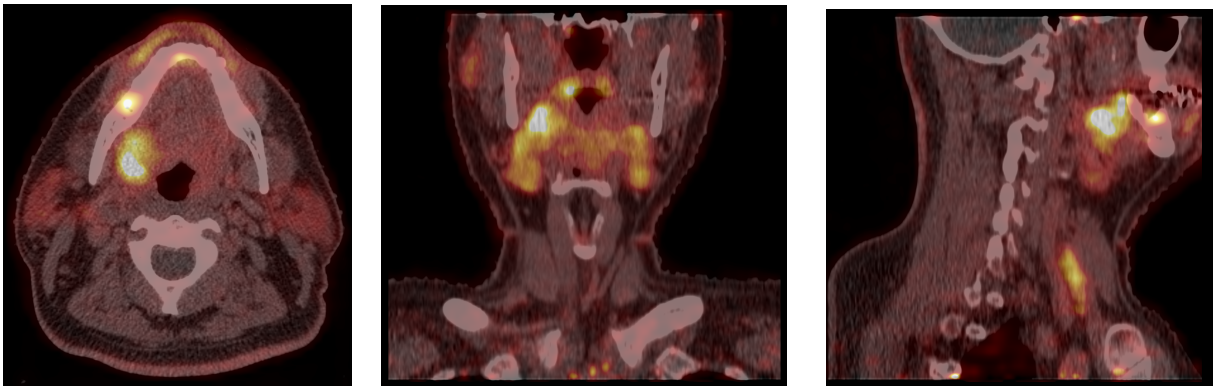

(a) axial (b) coronal (c) sagittal

Figure A6: The tumour in the right tonsil loge in three different views on baseline RGD PET with a low-dose CT

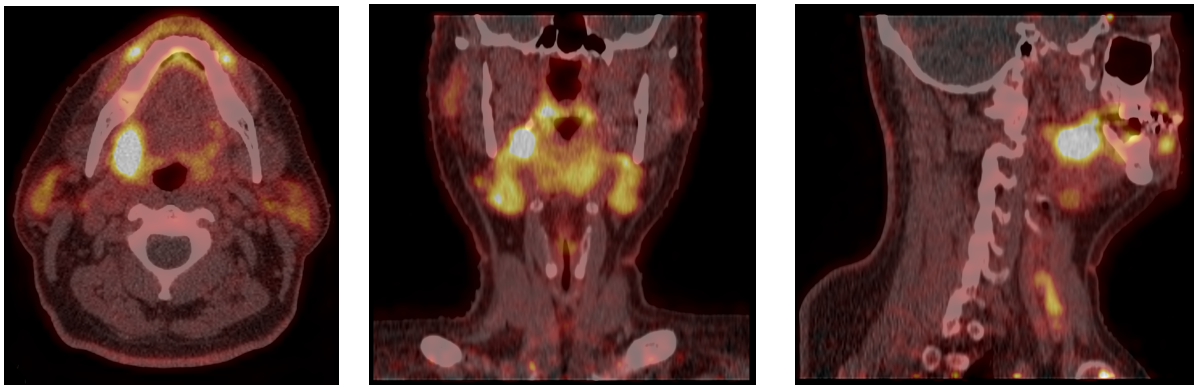

(a) axial (b) coronal (c) sagittal

Figure A7: The tumour in the right tonsil loge in three different views on follow-up RGD PET with a low-dosec CT

A.2 Letter of Approval of the Research Protocol

Included are the positive letter of approval of the CMO Regio Arnhem-Nijmegen on the 6^{th} of August 2019. Subsequently are included the letters of approval by the competent authority, the Centrale Commissie Mensgebonden Onderzoek and the letter of approval for local feasibility by the Radboud university medical center Executive Board.

Radboud universitair medisch centrum
Concernstaf Kwaliteit en Veiligheid
Commissie Mensgebonden Onderzoek
Regio Arnhem-Nijmegen

Postbus 9101, 6500 HB Nijmegen
Huispost 628
Geert Grooteplein 10
Radboudumc hoofdingang, route 629
T (024) 361 31 54

commissiemensgebondenonderzoek@radboudumc.nl
KvK 41055629/4

628

Mw. D. Lobeek
Radboudumc
Radiologie en Nucleaire Geneeskunde
Huispost 756

Ons Kenmerk
DE/CMO 407

Datum
6 augustus 2019

Titel: Imaging of tumour microenvironment in patients with oropharyngeal head and neck squamous cell carcinoma using RGD PET/CT imaging
RGD PET Imaging of Vasculature in Oropharyngeal Tumours (PIVOT)
Dossiernummer: 2019-5439
NL-nummer: NL69928.091.19

Geachte mevrouw Lobeek,

Bijgevoegd treft u aan het positieve oordeel van de CMO Regio Arnhem-Nijmegen over bovengenoemd onderzoek.

Dit betekent dat het onderzoek kan worden uitgevoerd in het centrum dat in het positieve oordeel wordt genoemd nadat de Raad van Bestuur/Directie van het centrum daarvoor toestemming heeft verleend.

Indien het voornemen bestaat het onderzoek ook nog in een ander centrum uit te voeren, dan dient aan de CMO Regio Arnhem – Nijmegen een onderzoeksverklaring (zie website www.ccmo.nl) van het betreffende centrum te worden overlegd. De CMO Regio Arnhem-Nijmegen kan vervolgens het positieve oordeel uitbreiden naar het betreffende centrum.

Voorwaarde voor het uitvoeren van een WMO-onderzoek in het Radboudumc is niet alleen het positieve oordeel van de CMO regio Arnhem-Nijmegen (of een andere erkende METC) maar ook de toestemming van de Raad van Bestuur van het Radboudumc. Informatie over de lokale uitvoerbaarheid is gepubliceerd in het Integraal Kwaliteitssysteem voor Wetenschappelijk Mensgebonden Onderzoek.

Ik vertrouw erop u met dit schrijven van dienst te zijn en namens de commissie wens ik u succes met de uitvoering van het onderzoek.

Met vriendelijke groet,
Namens de CMO Regio Arnhem-Nijmegen

Drs. R.B. Keus, vicevoorzitter

BESLUIT
Primaire beoordeling

NL nummer:	**NL69928.091.19**	**METC nr.**	**2019-5439**
Titel onderzoek:	**Imaging of tumour microenvironment in patients with oropharyngeal head and neck squamous cell carcinoma using RGD PET/CT imaging RGD PET Imaging of Vasculature in Oropharyngeal Tumours (PIVOT)**		

Contactgegevens: Mw. D. Lobeek, Radboudumc, Radiologie en Nucleaire Geneeskunde, Huispost 756
Verrichter: Radboudumc te Nijmegen

Besluit
De medisch-ethische toetsingscommissie CMO Regio Arnhem-Nijmegen heeft zich, op grond van artikel 2, tweede lid, sub a van de *Wet medisch wetenschappelijk onderzoek met mensen* (WMO), beraden over bovenstaand onderzoeksdossier.

De commissie oordeelt positief over het onderzoeksdossier uit te voeren in het volgende centrum:
- Radboudumc te Nijmegen (hoofdonderzoeker: E. Aarntzen)

Documenten
Het oordeel is gebaseerd op de documenten die in bijlage 1 zijn vermeld.

Achtergrond
Op 6 mei 2019 is het onderzoeksdossier ter beoordeling bij de commissie ingediend.
Daarna heeft de commissie nadere informatie opgevraagd waarop naar tevredenheid is geantwoord.

Met inachtneming van haar reglement is het onderzoeksdossier besproken in de vergadering van 4 juni 2019; zie bijlage 2 voor de bij de beoordeling betrokken commissieleden.

Overwegingen
De commissie is van oordeel dat aan de voorwaarden in artikel 3 van de WMO is voldaan.

De commissie heeft de inhoud van de onderzoeksverklaring van de deelnemende instelling bekeken. Zij heeft geconstateerd dat is voldaan aan de voorwaarden in artikel 3, onderdeel f, van de WMO. De commissie is van oordeel dat in redelijkheid is voldaan aan het bepaalde in artikel 5 WMO.

Naar de mening van de commissie betreft het geneesmiddelenonderzoek zoals bedoeld in artikel 1, eerste lid onder n, van de WMO. Tevens is artikel 13a van de WMO van toepassing en is voldaan aan alle in artikel 13d van de WMO genoemde aanvullende voorwaarden.

De commissie is van oordeel dat het onderzoeksprotocol in een toestemmingsprocedure voorziet die overeenstemt met artikel 6, eerste lid, van de WMO.

De commissie is van mening dat is voldaan aan de voorwaarden in artikel 6, vijfde t/m negende lid, van de WMO. De proefpersonen (en/of degenen die mede/in hun plaats bevoegd zijn tot het geven van toestemming voor deelname aan het onderzoek) worden op gepaste, volledige en begrijpelijke wijze schriftelijk over het onderzoek geïnformeerd en over de mogelijkheid om de toestemming te allen tijde in te trekken.

Verzekeringen
De commissie heeft geconstateerd dat is voldaan aan de verzekeringsplicht. Er is een proefpersonenverzekering afgesloten zoals bepaald in artikel 7, eerste lid, van de WMO en zoals nader uitgewerkt in het Besluit verplichte verzekering bij medisch-wetenschappelijk onderzoek met mensen 2015 (Besluit van 24 november 2014).

Het onderzoek valt onder de proefpersonenverzekering van Radboudumc.

De commissie heeft geconstateerd dat een aansprakelijkheidsverzekering is afgesloten zoals bepaald in artikel 7, negende lid, van de WMO.

Ten slotte wijst de commissie u op de voorwaarden en verplichtingen die in bijlage 3 zijn vermeld.

Hoogachtend,
Namens de CMO Regio Arnhem-Nijmegen

Drs. R.B. Keus, vicevoorzitter

Nijmegen, 6 augustus 2019

Beroepsprocedure
Tegen dit besluit kan een belanghebbende op grond van artikel 23 van de WMO binnen zes weken na de dag waarop het besluit is bekend gemaakt, administratief beroep instellen bij de Centrale Commissie Mensgebonden Onderzoek (CCMO). Het beroepschrift dient u te adresseren aan CCMO, Postbus 16302, 2500 BH Den Haag.

Radboudumc

Bijlage 1

Documenten:

A Aanbiedingsbrief van dr. E.H.J.G. Aarntzen en prof. dr. W.M. Prokop d.d. 01 mei 2019
Aanbiedingsbrief van dr. E.H.J.G. Aarntzen en prof. dr. W.M. Prokop d.d. 08 mei 2019
Ontvangstbewijs EudraCt-nummer d.d. 17 april 2019
Aanbiedingsbrief van dr. E.H.J.G. Aarntzen en prof. dr. W.M. Prokop d.d. 04 juli 2019 in reactie op vergaderbrief
Aanbiedingsbrief van dr. E.H.J.G. Aarntzen en prof. Dr. W. M. Prokop d.d. 24 juli 2019 in reactie op cie-vragen 15 juli 2019

B ABR-formulier, versie 02 d.d. 4 juli 2019
Clinical trial Application Form d.d. 01 mei 2019

C Onderzoeksprotocol versie 3 d.d. 24 juli 2019

D Investigator's Brochure Ga-68-DOTA-E-(cRGDfK)2 versie 5.0 d.d. 01 mei 2019
IMPD 68Ga-RGD-D0TA d.d. 07 september 2018
Bereidingsvoorschrift RGD-DOTA d.d. 08 oktober 2012
Voorbeeldetiketten in het Nederlands flacon RGD-DOTA d.d. 08 oktober 2012
Voorbeeldetiketten in het Nederlands Radiofarmaca
Voorbeeldetiketten in het Nederlands verpakkingsdoos d.d. 08 oktober 2012
Certificaat GMP compliance

E Proefpersoneninformatie en toestemmingsformulier versie 2 d.d. 04 julli 2019
Algemene informatie voor de proefpersoon (Minvws) d.d. februari 2019

G WMO-proefpersonenverzekering van het Radboudumc: van verzekeringsmaatschappij Centramed d.d. januari 2019, datum afgifte RTC CS d.d. 01 mei 2019
Bewijs dekking aansprakelijkheid van het Radboudumc: van verzekeringsmaatschappij Centramed d.d. januari 2019

H CV onafhankelijk arts, M. Gotthardt

I Onderzoeksverklaring van het Radboudumc te Nijmegen, getekend door het afdelingshoofd
van Radiologie en Nucleaire Geneeskunde d.d. 01 mei 2019 inclusief:
- CV lokale onderzoeker (E. Aarntzen)

K Radiation Ethics Form d.d. 08 mei 2019

Radboudumc

Bijlage 2

CMO Regio Arnhem-Nijmegen

Bij de beoordeling betrokken commissieleden

Arts/(vice)voorzitter	R. Keus
Arts(en)	F. Abdo
Kinderarts	S. Henriet
Ziekenhuisapotheker	R. Bruggemann
/klinisch farmacoloog	K. Kramers
Ethicus	A. Oerlemans
Jurist	F. van Agt
Methodoloog	E. Bronckhorst
Proefpersonenlid	W. Harmsen
Verpleegkundige	S. Bossmann
Klinisch fysicus	E. Baerends

Radboudumc

Bijlage 3

Voorwaarden en verplichtingen*

- **geen bezwaar bevoegde instantie *[alleen bij geneesmiddelenonderzoek]***:
  er kan pas met het onderzoek worden gestart, wanneer eveneens geen bezwaar wordt gemaakt binnen de voorgeschreven termijn door de bevoegde instantie;
- **geldigheid oordeel**:
  het positieve oordeel verliest zijn geldigheid als de inclusie van de eerste proefpersoon niet heeft plaatsgevonden binnen twee jaar nadat dit besluit is genomen;
- **amendementen**:
  amendementen dienen ter beoordeling aan de CMO Regio Arnhem-Nijmegen te worden voorgelegd;
- **startdatum onderzoek**:
  de CMO Regio Arnhem-Nijmegen dient op de hoogte te worden gesteld van de definitieve startdatum van het onderzoek. Dat is de datum waarop de inclusie van de eerste proefpersoon plaatsvindt;
- **voortgangsrapportage**:
  één jaar na de startdatum, en ieder jaar daaropvolgend, dient de METC op de hoogte te worden gebracht van de voortgang van de studie middels het formulier 'Voortgangsrapportage';
- **geldigheid verzekering**:
  in het geval het verzekeringscertificaat tijdens de voortgang van het onderzoek zijn geldigheid verliest, dient aan de CMO Regio Arnhem-Nijmegen tijdig een afschrift van een nieuw geldig certificaat te worden toegestuurd;
- **melding artikel 10**:
  indien het onderzoek een verloop neemt dat in noemenswaardige mate voor de proefpersoon ongunstiger is dan in het onderzoeksdossier is voorzien, moet daarvan terstond mededeling worden gedaan aan de CMO Regio Arnhem-Nijmegen met een verzoek tot een nader oordeel;
- **melding SAE's**
  SAE's dienen aan de CMO Regio Arnhem-Nijmegen gemeld te worden (raadpleeg de website van de commissie voor de te volgen procedure).
- **melding SUSAR's en jaarlijkse veiligheidsrapportage *[alleen bij geneesmiddelenonderzoek]*:**
  SUSAR's en jaarlijkse veiligheidsrapportage dienen aan de CMO Regio Arnhem-Nijmegen gemeld te worden (raadpleeg de website van de commissie voor de te volgen procedure).
- **Advies DSMB *[alleen indien een DSMB is ingesteld]***
  indien een advies van de DSMB niet volledig wordt opgevolgd, dient de CMO Regio Arnhem-Nijmegen het advies met toelichting over het niet (volledig) opvolgen van het advies te ontvangen en toestemming te geven voor voortzetting van het onderzoek;
- **melding (voortijdige) beëindiging**:
  (voortijdige) beëindiging van het onderzoek dient, met redenen omkleed, te worden gemeld aan de CMO Regio Arnhem-Nijmegen.
- **eindrapportage**:
  de CMO Regio Arnhem-Nijmegen dient op de hoogte te worden gebracht van de resultaten van het onderzoek middels een eindrapport / (gesubmitte) publicatie.

* Termijnen en overige uitleg ten aanzien van de indiening van de verschillende documenten aan de CMO Regio Arnhem-Nijmegen vindt u op de website van de CCMO bij het standaard onderzoeksdossier en de toelichting daarop en onder stap 4 van het Stappenplan toetsing TC

Radboudumc

Bijlage 4

Title: Imaging of tumour microenvironment in patients with oropharyngeal head and neck squamous cell carcinoma using RGD PET/CT imaging
RGD PET Imaging of Vasculature in Oropharyngeal Tumours (PIVOT)
Filenumber CMO : 2019-5439

Dear Mrs. Lobeek,

The medical ethical reviewing committee CMO Regio Arnhem-Nijmegen has reviewed the above-mentioned research file on the grounds of section 2, paragraph 2, sub a of the Medical Research Involving Human Subjects Act (WMO).

The committee has approved the research file on the 6th of August 2019.

The decision is based on the documents mentioned in appendix 1 of the original decision written in Dutch.

With kind regards,

On behalf of the CMO Region Arnhem-Nijmegen

Drs. R.B. Keus, vice-chairman

Geachte D., MSc Lobeek,

De Centrale Commissie Mensgebonden Onderzoek (CCMO) heeft zich als Bevoegde instantie voor de marginale beoordeling van geneesmiddelenonderzoek in Nederland, op grond van artikel 13i, van de Wet medisch-wetenschappelijk onderzoek met mensen (WMO), beraden over het onderzoeksprotocol PIVOT studie, NL69928.091.19.

Op 23-05-19 is het onderzoeksvoorstel ter beoordeling bij de Centrale Commissie Mensgebonden Onderzoek (CCMO) ingediend.

De Centrale Commissie Mensgebonden Onderzoek (CCMO) heeft als Bevoegde instantie geen bezwaar tegen uitvoering van het onderzoek in Nederland op basis van haar marginale toets.

De marginale toets van de Bevoegde instantie betreft het controleren van de Clinical Trial Module van de Eudravigilance database op onverwachte ernstige bijwerkingen voor ongeregistreerde geneesmiddelen en het controleren van de EudraCT database . Indien nodig, kan de oordelende METC de Centrale Commissie Mensgebonden Onderzoek (CCMO) vragen de Europese databank Eudravigilance te raadplegen voor geregistreerde geneesmiddelen. De Centrale Commissie Mensgebonden Onderzoek (CCMO) zal de oordelende METC informeren over het resultaat.

Wellicht ten overvloede wijzen wij u erop dat, voordat het onderzoek in Nederland van start kan gaan, het onderzoek tevens positief beoordeeld moet zijn door een daartoe bevoegde erkende Medisch-Ethische Toetsingscommissie. Deze verklaring van geen bezwaar verliest zijn geldigheid als met het uitvoeren van het onderzoek niet is begonnen binnen een jaar nadat deze verklaring is afgegeven.

Tot slot wijst de Centrale Commissie Mensgebonden Onderzoek (CCMO) erop dat, op grond van artikel 7:1 van de Algemene wet bestuursrecht (Awb), degene wiens belang rechtstreeks bij het besluit is betrokken daartegen binnen zes weken na de dag waarop dit besluit bekend is gemaakt, bezwaar kan maken bij de Centrale Commissie Mensgebonden Onderzoek (CCMO).

Met vriendelijke groet,

Centrale Commissie Mensgebonden Onderzoek (CCMO) 04-06-19

DIT IS EEN AUTOMATISCH GEGENEREERD BERICHT

THIS IS AN AUTOMATED EMAIL

Dear D., MSc Lobeek,

The Centrale Commissie Mensgebonden Onderzoek (CCMO), as Competent Authority for the review of clinical trials in the Netherlands, has performed a marginal assessment of the clinical trial application PIVOT studie, NL69928.091.19 under section 13i of the Medical Research in Human Subjects Act (WMO).

The Centrale Commissie Mensgebonden Onderzoek (CCMO) received the clinical trial application at 23-05-19 for an assessment.

Based on a marginal assessment, the Centrale Commissie Mensgebonden Onderzoek (CCMO), as Competent Authority, found no objection against the execution of the clinical trial within the Netherlands.

The marginal assessment of the Competent Authority involves a check of the Clinical trial Module of the Eudravigilance database for suspected unexpected serious adverse reactions (SUSARs) for unauthorised medicinal products and a check of EudraCT database. If required, the reviewing Medical Research Ethics Committee, may request the Centrale Commissie Mensgebonden Onderzoek (CCMO) to search the European database Eudravigilance for authorised medicinal products. The Centrale Commissie Mensgebonden Onderzoek (CCMO) will inform the reviewing Medical Research Ethics Committee on the results.

The Centrale Commissie Mensgebonden Onderzoek (CCMO) would like to point out that before the clinical trial commences approval from a competent accredited Ethics Committee is required.

This approval loses it?s validity if the study has not been started within a year after this declaration of no objection.

Based on section 7:1 of the General Administrative Law Act (Awb), the person whose interest is directly associated with the decision can lodge an appeal with the Centrale Commissie Mensgebonden Onderzoek (CCMO) within 6 weeks after the day the decision has been announced.

With kind regards,

Centrale Commissie Mensgebonden Onderzoek (CCMO) 04-06-19

DIT IS EEN AUTOMATISCH GEGENEREERD BERICHT

THIS IS AN AUTOMATED EMAIL.

Radboudumc

Radboud university medical center
Executive Board

P.O. Box 9101, 6500 HB Nijmegen
The Netherlands
Internal postal code 630
Geert Grooteplein Zuid 10
Radboudumc main entrance, route 630
T +31 24 361 89 33

www.radboudumc.nl

Dutch Chamber of Commerce
trade register 41055629/4

630
Radboud university medical center
Department Radiology and Nuclear Medicine
E.H.J.G. Aarntzen, PhD
Internal postal code 757
P.O Box 9101
6500 HB NIJMEGEN

Date	Our reference	Page
16 September 2019	RvB19.51751	1 van 2

Your reference
NL69928.091.19

Contact

Subject
Approval from the Radboud university medical center Executive Board

Title : Imaging of tumour microenvironment in patients with oropharyngeal head and neck squamous cell carcinoma using RGD PET/CT imaging
File number : NL69928.091.19

Dear Colleague,

You recently submitted the above mentioned request for approval to carry out clinical research at Radboud university medical center. In this regard, I would like to remind you that on October 1, 2013, the Executive Board implemented a standardized framework ("normenkader") to ensure the quality of WMO-required research (i.e. investigator-initiated research falling under the Medical Research Involving Human Subjects Act).

I am pleased to inform you that your submitted research request complies with these guidelines (refer to the summary on Page 2 of this letter). Thus, the Executive Board hereby approves your request to conduct research at Radboud university medical center.

For questions concerning approval from Radboud university medical center's Executive Board, please contact the service desk of the Radboudumc Technology Center Clinical Studies (RTC CS), quoting the above reference number.
For further questions concerning the execution of the study, please check the Integral Quality System (IQS) via Q-portal.

In closing, I wish you every success in carrying out your research.

Kind regards,

Professor Jan W.A. Smit, PhD
dean / vice chairman

Documents reviewed:

- Positive decision MREC CMO Regio Arnhem-Nijmegen (reg.nr. 2019-5439) d.d. 6 August 2019
- Positive decision competent authority (CCMO) d.d. 04 June 2019
- Radiation Ethics Form, signed by medical physisist d.d. 08 May 2019

Quality insurance standards:

Risk classification (as judged by MREC):	negligible
Datamanagement plan:	approved
Monitoring plan (according to NFU criteria)*:	approved
Expertise (BROK-certification)	approved

Ionizing radiation – research on human subjects in accordance with ICRP-62:

Meets legal requirements as stipulated in the *Stichting Katholieke Universiteit* organization permit:	approved

* *We would like to point out that the research contract (if applicable) and the monitorplan have to be signed by all parties before the start of the study.*

C.c. Ms. E.A.J. van Genugten, BSc, M.M. Wiegman (AMD)